Dynamic Strain Aging of Al-Mg Alloys after Severe Plastic Deformation

Von der Fakultät für Georessourcen und Materialtechnik
der Rheinisch-Westfälischen Techischen Hochschule Aachen

Zur Erlangung der akademischen Grades
eines Doktors der Naturwissenschaften

Genehmigte Dissertation
Vorgelegt von **M.Sc**

Chenlu Meng

Aus Fujian/Zhangzhou, China

Berichter: Univ.-Prof.Dr.rer.nat.Dr.h.c. Günter Gottstein
Univ.-Prof.Dr.-Ing. Gerhard Hirt

Tag der mündlichen Prüfung: 29.März 2018

Acknowledgements

The experience of my master and PhD study in Institute für Metallkunde und Metallphysik at RWTH Aachen, was valuable and meaningful through my entire life. There are so many people here I would like to acknowledge. Without their selfless and continuous help, I would not accomplish anything, therefore, thank you.

Above all, I would like to salute to Prof. Gottstein. Not only because his wisdom helped me conquer all the difficulties from work, but also his unbelievable kindness supported and encouraged me walking out my trough in life. I am very lucky and honored to be educated by and worked under the guidance of such a distinguished professor. Outside the institute, his influence is even more significant. His humble and patience manner will definitely modify me in my future career, as a high school teacher. I will be proud to tell my students, that I truly learned from the best!

I would also like to thank Prof. Dr. Sandra Korte-Kerzel, for her continuous concern about my project and her kind support.

Specially, I want to thank Dr. Hu Weiping, who was the first direct supervisor and provided me the great beginning of my PhD study. With his guidance, all the knowledge from the textbook became lively, which lighten up my enthusiasm to observe and analyze problems in new level. The discussion with Dr. Hu is always smooth and practically helpful. Dr.-Ing Sandlöbes Stefanie, who stood up helping me with the finishing of my doctoral study after Dr. Hu´s retirement, is another important person I appreciate. Her broad scientific sight inspired me to investigate my project from different angle, and her enthusiasm for work also encourages me to pursuit my own dream career.

During my period in IMM, David Beckers taught and helped me with every aspect of Metallography. Arndt Ziemons and Schütz Gerhard contributed excellently to the casting and cutting of material samples. Thomas Burlet instructed me a lot on mechanical testing. Sabine Lakrache took care of me on countless paper work. Matthias Loeck offered me a great relaxing place in the table tennis room always filled with laughter. My dear GYM brothers, Al-Samman Talal, Barreles Mora Luis, Indranil Basu, ensure me a healthy physical body to conquer all the challenges in life.

All the Chinese colleagues, including Dr. Bingbing Zhao, Dr. Lei Hu, Dr. Yaping Lv, Dr. Shiteng Zhao, M.Sc Feng Jiao, M.Sc Fengxin Mao, M.Sc Hongyu Xiao, M.Sc Xiaoyu Mei, Zizhao Huang are acknowledged. They taught me a lot from a rookie student and enriched my days in IMM.

My last sincere appreciation goes to my beloved family members. Without all the supports from you, I will not become who I am today.

Table of Contents

1. Introduction 5

1.1 Al-Mg Alloys 5

1.2 Portevin-Le Chatelier Effect 7

1.3 Severe Plastic Deformation 14

1.3.1 ECAP 15

1.3.2 CCDP 16

1.3.3 Comparison of Methods 18

1.3.4 As-SPD feature 18

2. Experimental 21

2.1 Components 21

2.2 Cast Ingot Preparation 22

2.3 CCDP 23

2.4 Microcharacterization 23

2.4.1 Transmission Electron Microscopy (TEM) 23

2.4.2 Electron Backscatter Diffraction (EBSD) 24

2.4.3 X-ray Diffraction (XRD) 24

2.5 Mechanical tests 25

2.5.1 Strain Rate Jump Tests (SRJT) 26

2.5.2 Tensile tests at elevated temperatures 28

3. Results 30

3.1 Microstructure....30
3.1.1 Experimental techniques and microstructural phenomena....30
3.1.2 Micro characterization after room temperature deformation....31
3.1.3 Micro characterization after annealing....41
3.2 Mechanical properties....51
3.2.1 Mechanical tests at room temperature....51
3.2.2 Mechanical tests at elevated temperatures....60

4. Discussion....66
4.1 Properties at ambient temperature....66
4.1.1 Analysis of the deformed microstructure....66
4.1.2 Mechanical properties....72
4.1.3 Dynamic strain aging....80
4.2 Properties at elevated temperatures....92
4.2.1 Effect of preheating to test temperature....92
4.2.2 Deformation mechanisms....92
4.3 Relevance for sheet forming applications....99
5. Summary....101
6. References....105

List of Symbols

A	Material related constant
b	Burgers vector
$C(t_a,C_0)$	Aging solute concentration
C_0	Original alloy composition
C_∞	Saturated aging concentration
C_v	Vacancy concentration
d	Grain size
D_0	Diffusion pre-exponential factor
$\Delta E(t_a)$	Binding energy between solutes and dislocation core
ΔE_∞^{core}	Saturated binding energy
ΔG	Gibbs free energy of plastic deformation
K	Boltzmann constant
K	Vacancy concentration prefactor
l_f	Forest dislocation spacing
m	Strain rate sensitivity
m_i	Instantaneous strain rate sensitivity
m_s	Steady state strain rate sensitivity
N	Dislocation density prefactor
Q_m	Effective activation energy for solute migration
r_{sol}	Effective radius of solute atmosphere
r'_{sol}	Solute atomic radius
T	Absolute temperature
t_a	Aging time of dislocations
t_d	Intrinsic cross-core solute diffusion time
t_t	Transition time
t_w	Waiting time of dislocations in front of obstacles
V^*	Activation volume
α	Vacancy concentration exponent
β	Dislocation density exponent
$\dot{\varepsilon}$	Strain rate
$\dot{\varepsilon}_0$	Strain rate pre-exponential factor
$\dot{\varepsilon}_c$	Critical strain for the onset of serrated flow

ρ	Dislocation density
ρ_m	Mobile dislocation density
ρ_f	Forest dislocation density
σ	Flow stress
$\sigma_{0.2}$	Yield stress
σ_{th}	Thermal stress component
σ_a	Athermal stress component
σ_{DSA}	Extra flow stress component contributed by dynamic strain aging
σ_{drop}	Magnitude of stress drop during serrated flow
$\Delta\sigma_{\mathrm{i}}$	Instantaneous stress response upon strain rate jump
$\Delta\sigma_s$	Steady state stress response
$\Delta\sigma_{thi}$	Change of thermal stress component upon strain rate jump
Ω	Elementary strain
CCDP	Confined channel die pressing
CG	Coarse grain
DSA	Dynamic strain aging
GB	Grain boundary
ND	Normal direction
PLC	Portevin-Le Chatelier
RD	Rolling direction
RX	Recrystallization
SFE	Stacking fault energy
SIBM	Stress induced boundary migration
SPD	Severe plastic deformation
SRJT	Strain rate jump test
SRS	Strain rate sensitivity
nSRS	Negative strain rate sensitivity
UFG	Ultrafine grain

1.Introduction

1.1 Al-Mg Alloys

During the past century, various aluminum alloys have been designed with excellent engineering properties, i.e. tensile strength, ductility, density, formability, weldability and corrosion resistance, to name a few. Nowadays Al alloys are widely used in engineering structures and components where high strength-to-weight ratio, good formability and corrosion resistance are required.

Solid solution hardening is one powerful strengthening mechanism in coarse grained Al alloys. Figure 1.1 shows the evolution of yield strength with increasing concentration of alloying elements [Sanders 1986]. The enhancement of the yield stress by virtually all solute additions is evident, however, it depends on the solute element and its dependence on concentration is not linear. Only modest solution strengthening can be achieved with Mn and Cu [Totten 2003], whereas Mg causes outstanding strengthening. On the other hand, Mg decreases the density of Al more effectively than other element by approximately 0.5% for every 1 wt% Mg in solid solution [Gottstein 2004]. Therefore, Al-Mg alloys are comparably lighter than other Al alloys, which make them much more attractive for use in automotive industry. What is more, Al-Mg alloys prepared from the high grade Al exhibit optimal corrosion resistance and reflectivity. In industry, Al-Mg alloys are denoted as 5000 series Al alloys. Up to date, AA 5000 alloys have been widely studied and applied, especially in the field of beverage packaging, automotive industry and marine applications.

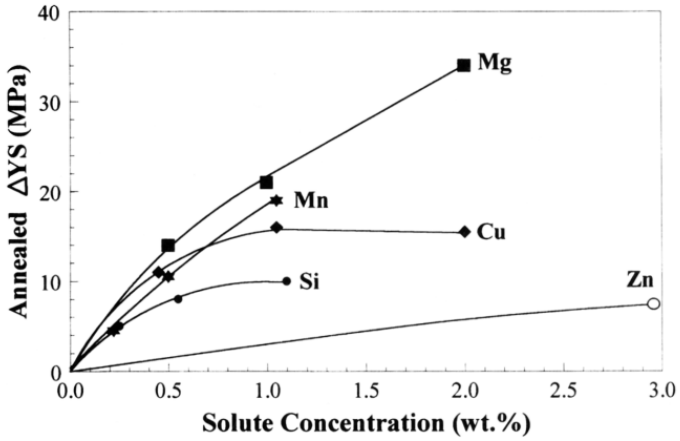

Figure 1.1: Weight percent solute of different alloy element to the increase of yield strength.

In commercial AA 5000 series alloys contain besides Mg also other elements, e.g. Fe, Si, Zn, etc. Those secondary elements are typically present only in small amounts but necessary for specific physical properties. In the AA 5000 series commercial alloys the Mg content ranges from 0.5 to 13 wt.%. The low Mg content alloys have better formability and are less flammable, whereas the highly concentrated alloys possess excellent strength. Table 1 lists some important mechanical properties as a function of Mg concentration [Total Materia].

Table 1: Mechanical properties of commercial Al-Mg alloys.

Alloy	Condition	Hardness (HV)	R_M (MPa)	$R_{p0.2}$ (MPa)	Elong. A (%)
0.5-1.5% Mg	Annealing	25-35	100-150	40-80	20-40
	Stress relieved	60-80	200-300	150-250	5-15
1% Mg, 1% Mn	Annealing	35-50	150-200	50-100	20-30
	Stress relieved	65-90	250-350	200-300	5-8
2-3% Mg, 0-2% Zn	Sand cast	50-60	150-200	50-100	3-7
	PM cast	50-70	170-220	70-150	3-8
	Annealing	40-55	150-250	80-150	25-35
	Stress relieved	65-90	250-350	200-300	6-15
5-7% Mg	Sand cast	50-60	150-200	70-150	4-10
	PM cast	60-80	200-300	100-200	5-12
	Annealing	60-80	250-350	120-250	20-30
	Stress relieved	80-100	400-500	250-350	10-15
8-12% Mg	Sand cast	70-90	150-300	100-200	3-8
	PM die cast	75-95	200-350	100-250	5-10
	Annealing	80-100	350-500	150-300	10-25
	Stress relieved	90-110	450-600	300-400	5-15
	Heat treated	120-140	400-500	250-350	20-25

In Al-Mg alloys a heat treatment does not lead to a major improvement in strength, but significantly increases the ductility. The melting temperature of Al-Mg alloys ranges around 650°C, which is relatively low and makes the material properties quite sensitive to high temperature exposure. The heat treatment of Al-Mg alloys for improvement of material properties has been explored deeply and systematically [Sjölander 2010, Mrowka-Nowotnik 2005]

In 5000 series Al-Mg alloys, strength is caused mainly through solid solution hardening, precipitation hardening and to a less extent by grain size effects, depending on Mg content. As Mg is a substitutional element in Al and the Mg atom is 12% larger than the matrix Al atom, it acts as a center of dilatation and interacts with the hydrostatic components of the strain field of dislocations. The interaction between the stress field of the solute atoms and the strain field of dislocations leads to an attractive force that draws Mg atoms to the dislocation core, which exert a retarding force for dislocation motion. The segregation of Mg atoms at the dislocation core reduces the tendency for dynamic recovery and dislocation rearrangement into lower energy configurations, leads to an increase of the dislocation density of the alloys and a more uniform dislocation distribution [Estrin 1995].

Besides all the advantages mentioned above, however, there is a drawback during manufacturing since deformation at room temperature and elevated temperatures may be discontinuous in some fabricating situations. In such case the strain localizes in narrow bands, referred to as the Lüders bands, and cause serrations of the flow stress (PLC effect).The PLC effect dramatically decreases the loading stability and may cause unexpected failure of the material. Besides, this phenomenon leads to surface roughness of semi-finished products, e.g. sheet material for the automotive industry, which requires an extra heat treatment to be recovered. Hence, there exists significant industrial need to understand and then eliminate the PLC effect.

1.2 Portevin-Le Chatelier Effect

The PLC effect is characterized by serrations on the flow curve and a localization of deformation, mostly observed in dilute solid solutions deformed in an intermediate temperature range. Since the 1950s respective studies have addressed the dependence of dynamic strain ageing (DSA) on various deformation conditions, e.g. temperature, strain/strain rate and stress rate, as well as alloy composition, solute element diffusivity and microstructure (grain size, precipitate state), which essentially affect the interaction of mobile dislocations with obstacles like solute atoms, forest dislocations, precipitates and grain boundaries. The PLC effect is commonly understood as a consequence of DSA. However, up to date a truly predictive PLC model is still missing, especially when the deformation kinetics are taken into consideration.

Despite of the complexity of the physical interpretations, the phenomenology of the PLC effect is quite obvious. The serrations and the associated deformation bands are classified into three types [Ananthakrishna 2007], see Figure 1.2. With increasing strain rate/ decreasing temperature, type C bands with large and regular stress drop are observed first. Then, type B "hopping bands" show up with lower serration regularity and smaller stress amplitudes. Finally, continuously propagating type A bands associated with small stress drops are seen. These three different types of PLC bands are believed to represent distinct correlated states of dislocation in the bands.

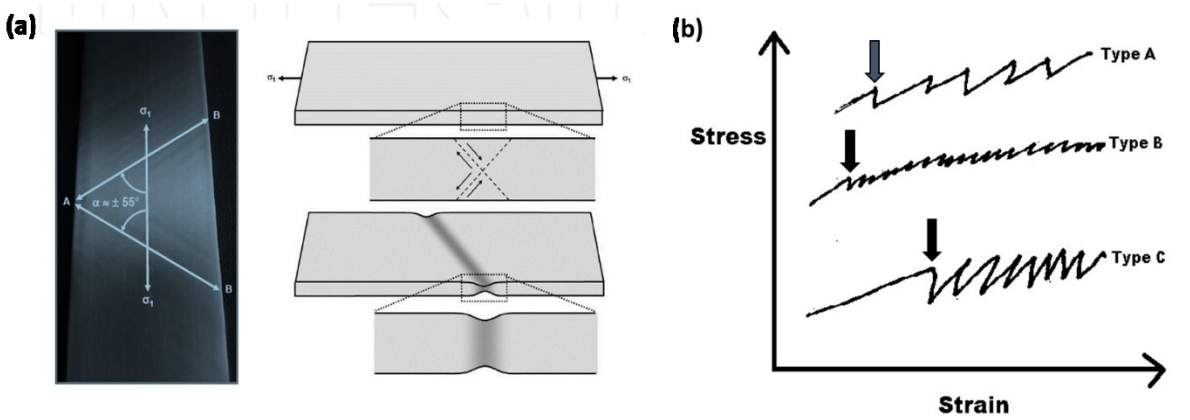

Figure 1.2: Observed PLC bands on the surface of Al-5Mg (a) and different types of repetitive stress drops in flow curves (b).

The classical explanation of the PLC effect via DSA was first proposed by Cottrell [Cottrell 1948, Cottrell 1953]. The interaction of quasi-viscously moving dislocations with a solute cloud was assumed to cause the serrated yielding and jerky flow, as observed in steels and Al alloys during plastic deformation. The segregation of mobile solute atoms to dislocations on the one hand, and the thermally activated unpinning of glide dislocations from their solute clouds on the other hand, represent the overall dynamics, alternating and repetitive competing processes. Since then the theoretical concepts to explain the PLC effect have advanced remarkably. Subsequent studies cast doubts on the interpretation which associated DSA with the interaction of mobile solutes with moving dislocations, instead a dislocation arrest model was proposed [Mulford 1979]. It is now generally accepted that the jerky flow during deformation owes to the fact that solutes move to junctions of forest and mobile dislocations, consequently increase the junction strength and block further mobile dislocations (pinning). Once the mobile dislocation can break away from the junction under an increased stress, it can move continuously and freely (unpinning) until it meets the next obstacle [van den Beukel 1982]. The competition between the slow rate of aging and sudden unpinning of the dislocations translates at the macroscopic level into a negative strain rate sensitivity (SRS) of the flow stress as a function of strain rate, mathematically deduced by Penning [Penning 1972].

It should be noted that DSA does not necessarily manifest itself immediately as plastic deformation begins, rather the PLC effect is characterized by a critical strain ε_c. The onset of the PLC effect (serrations on the flow curve) takes places when strain hardening dominates and the strain dependent SRS turns negative [Kocks 1981, Mulford 1979, Lee 1993]. The evolution of ε_c with strain rate and deformation temperature was also studied intensively. If ε_c increases with increasing strain rate (or decreasing temperature), this is defined as normal relation, whereas at other conditions the relationship will be reversed and is denoted as abnormal relation. It is rather obvious and supposed to be influenced by the deformation conditions. Since the Lüders bands degrade the surface quality, it is of industrial interest to eliminate or postpone the appearance of DSA, i.e. enlarge the critical strain ε_c.

Since dynamic strain aging is the fundamental physical mechanism utilized directly or indirectly for modelling the PLC effect, and as diffusion of solute atoms is the key atomitic

mechanism, the nature and the role played by diffusion caused a major debate. Van den Beukel et al. proposed vacancy-assisted models [Vandenbrink 1975, van den Beukel 1975, van den Beukel 1980] for interpreting the onset of serrated yielding and the effect of DSA on the SRS in Al-Mg, Au-Cu, Cu-Sn alloys. The basic mechanism envisioned was clustering of solutes at the arrested dislocation line by lattice diffusion from the region nearby the defect. According to the vacancy-assisted model of DSA, the PLC effect must be sensitive to the solute diffusivity and the mobile dislocation density [van den Beukel 1980, van den Beukel 1982]. On the other hand, Kocks et al. [Wycliffe 1980, Mulford 1979, Kocks 1985] suggested a strain hardening model, incorporating pipe diffusion based on the dislocation arrest theory as originally proposed by Sleeswyk [Sleeswyk 1958]. The mechanism underlying the model required that at the junction of a clean mobile dislocation with a clustered forest dislocation, solute atoms diffused from the forest dislocation along the core of the mobile dislocation. The lock strength increased with the arrest time as the solute increasingly pinned longer segments of the mobile dislocation. In this case, the solute mobility will mainly influence the strain hardening component but not the friction component of the flow stress and therefore, DSA and the PLC effect should be stress sensitive but not strain sensitive. The two models were compared in a joint article [Van den Beutel 1982].

Neutrally with respect to the debate, Kubin and Estrin proposed a heuristic model to assess the critical conditions associated with the PLC effect, based on the strain dependence of both the densities of mobile (ρ_m) and forest (ρ_f) dislocations instead of a vacancy assisted mechanism [Estrin 1986, Kubin 1990, Kubin 1992, Brechet 1995]. A key quantity, the elementary strain Ω produced when all mobile dislocations perform a successful thermally activated step through the forest obstacles, was estimated by studying a system of coupled differential equations for the evolution of the two densities. It was shown that by refining the strain dependence of the densities of mobile and forest dislocations, it was possible to obtain a rather realistic description of the critical strain ε_c, therefore the different limits of the PLC domain could be defined. The occurrence of jerky flow was predicted for Al-Mg and CuSn solid solutions by the model and showed qualitative agreement with experimental observations [Guillot 1972, Räuchle 1973]. Noteworthy, the model also explained the "inverse" behavior, which has been repeatedly observed in Al-based substitutional solid solutions for low strain rate tests conducted at room temperatures [Brechet 1995, Miura 1972, McCormick 1972]. The influence of precipitation before and during deformation modified the

concentration of solute atoms dissolved in the matrix, and it also substantially modified the elementary strain [Guillot 1972]. From another point of view, the development of both types of dislocation densities were calculated using the local stress increment of plastic instabilities [Horvath 2007]. The estimated dislocation densities as a function of strain were compared with the Kubin-Estrin model. The quantities of both densities obtained by different ways showed a similar tendency in their development during plastic deformation. The significance of Mg concentration was discussed as well, regarding its influence on the PLC plastic instabilities and on both dislocation densities.

Later on, the idea of strain-induced vacancies to enhance bulk diffusion (as it was observed that without extrinsic vacancies the diffusion coefficient in the bulk was too small) was challenged [Cuddy 1972, Schwaz 1985, Balik 1993, Nortmann 1997]. The results of their experiments indicated that the vacancies were not the decisive factor for DSA. While pipe diffusion presumably may proceed without being assisted by vacancies, the dislocation junction strengthening model has received numerous support by experiments performed on substitutional solid solutions of FCC metals. Most experimental data obtained from uniaxial tensile tests were successfully fitted by this model which indicated that pipe diffusion was the dominant DSA mechanism [Kalk 1995, Draheim 1994, Ling 1993, Springer 1991, McCormick 1978]. The activation energy for the PLC effect was measured by fitting experimental data to the model as well as by monitoring the temperature and rate dependence of the critical stress for PLC [Schwink 1997, Kumar 1995]. It was concluded that both the lower (normal) and the higher (inverse) temperature PLC regimes could be characterized by a pipe diffusion control model. A calorimetric study of the dynamics of solute clustering concluded that solute migration took place by pipe diffusion early on and by bulk diffusion at later times during the clustering process [Varschavsky 1998].

The common acceptance of pipe diffusion as the dominating mechanism for PLC was recently questioned by an atomistic simulation study of Mg diffusion along the core of dislocations in Al [Picu 2004]. It was verified that, if vacancy assistance was cut out of the picture, the solute diffusion along the core was almost as difficult as it was in the bulk (the activation energy for pipe diffusion was about 75% of the bulk value). Therefore, the pipe diffusion was also too slow to attribute the strengthening of junctions during the arrest time t_w of mobile

dislocations. Further, Picu proposed a new mechanism based on the strength variation of dislocation junctions due to the presence of solute clusters on forest dislocations [Picu 2004]. The process was possible since forest dislocations are stationary for much longer time intervals than t_w, and the strengthening effect depended on the cluster size, which was variable with the aging time t_a. Accordingly, the model was able to qualitatively reproduce several features observed experimentally [Soare 2005, Picu 2005].

Starting out from a deterministic solute kinetics, a statistical theory of discontinuous glide of non-interacting dislocations in the presence of DSA was developed by Hähner [Hähner 1996]. The results differed from former theories: DSA was found to be insufficient to explain the occurrence of a negative SRS, unless collective effects of dislocation interactions were also taken into account. Subsequently, a constitutive model of the PLC effect was proposed by Hähner and Rizzi, which described the spatial-temporal dynamics of the PLC effect by analyzing the evolution of an additional activation enthalpy during DSA owing to solute clustering at the dislocation junctions [Hähner 2003, Rizzi 2004]. In this description, the activation entropy is influenced by the waiting time of dislocation in front of obstacles when solute aging took place, i.e. solutes diffused to the core of dislocations and increased the activation entropy, although such an increase was counteracted by the product of activation volume and effective stress. Various types of PLC flow behavior (from A to C) were numerically reproduced, and the qualitative features of the PLC effect observed in experiments were correctly reproduced by this model. Moreover, based on a statistical theory of coupled dynamics between mobile dislocations and solutes, the relaxation effects due to DSA and critical conditions for the PLC effect were also quantitatively analyzed [Hähner 1997]. Available results in terms of the critical plastic strains of the regime of serrated flow as a function of the applied strain rate and deformation temperature, as well as in dependence of well-defined material parameters accessible from tensile tests, could be obtained. In particular, an “inverse behavior” was traced back to the same thermally activated process that caused “normal behavior”, as a comparison with Kubin and Estrin’s model [Kubin 1990] showed. It was finally concluded that not only a single diffusion process, but several aging mechanisms with different free activation enthalpies may be active concurrently.

The same conclusion, i.e. negative SRS could not be obtained with the condition of single rate dependent strengthening mechanism, was demonstrated by Soare and Curtin [Soare 2008] with another route, where the specific time dependence of the energy barrier due to aging was emphasized. With the ability to recover the classical kinetic theories in the absence of aging effects, but also able to incorporate various dislocation/solute interactions mechanisms, the model provided a robust rate dependent constitutive equation for solute strengthening and aging effects in alloys. In a companion paper, the influence of forest strengthening and forest aging was considered within the same fundamental framework, based on the assumption that a single cross-core diffusion controls the aging of both the solute and the forest strengthening mechanisms [Curtin 2006, Soare 2008]. Consequently, the dynamic forest strengthening mechanism, previously proposed and analyzed by Picu [Picu 2004, Soare 2005], entered the theory and provided a negative SRS so that the overall SRS was negative over a range of strain rate and temperatures. All the key parameters in this full rate-dependent constitutive model, apart from forest dislocation evolution parameters, were derivable from atomistic-scale material parameters. The prediction of the steady-state stress/strain/strain-rate/temperature/concentration dependent material response showed good qualitative and quantitative agreement with corresponding experimental results. However, in case of some high temperature results, certain predicted data was not consistent with the experimental values, which indicated that there might be other high-temperature mechanisms not represented in this model. For instance, solute drag acting on the unpinned mobile dislocation, the forest dislocation density decreasing due to annihilation and other recovery, even recrystallization mechanisms were all very likely to occur and complicated the overall behavior.

The fundamental idea of Curtin's theory was to introduce cross-core diffusion: single atomic jumps of solutes directly across the slip plane, from the compression to the tension side, in the core of the dislocation. Figure 1.3 depicts the binding energy of Mg substitutional solute in the vicinity of an edge dislocation, positive energy represents binding and the arrows indicate the flux direction of Mg. Across a core interaction region there was a differential binding energy, which provided a strong driving force for cross-core diffusion, thus led to an activation enthalpy much lower than in the bulk. Since the diffusion distance in this case was within several atomic lengths, it could happen very quickly and therefore could explain the long-disputed fact that bulk diffusion and pipe diffusion could not take place quickly enough

to lead to the pronounced drag effect [Curtin 2006]. This assumption of cross-core diffusion was supported very recently by the observation of an asymmetrical Mg distribution along some of the dislocations in an Al-Mg alloy using Atom Probe Tomography (APT) [Aboulfadl 2015]. Another significant observation was a tail-like Mg depletion behind a moving dislocation, which indicated an excellent agreement with the model prediction of Zhang for the case of high dislocation velocity [Zhang 2008]. The simulation revealed that, for dislocation velocities above a critical value, the Mg concentration was drastically depleted in the compressive regime above the dislocation slip plane and increased below the slip plane in the dilatation region. This provided for the first time an experimental atomic-scale proof for cross-core diffusion.

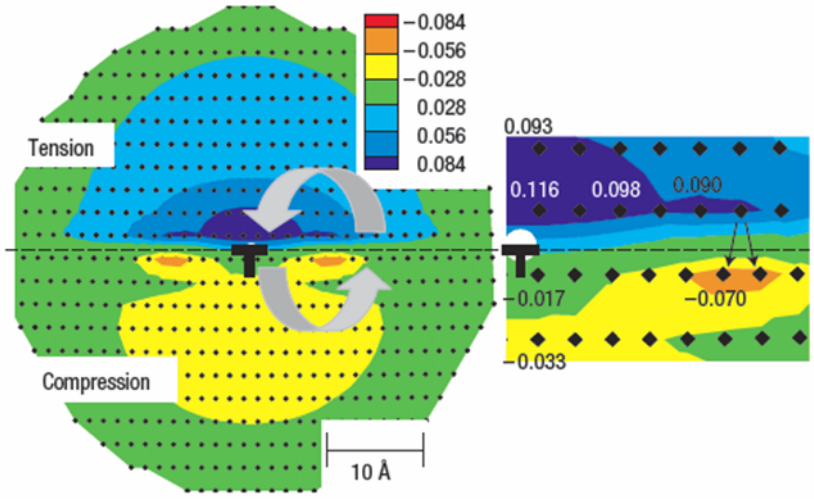

Figure 1.3: Binding energy of a Mg substitutional solute and an edge dislocation in Al versus Mg solute position [Curtin 2006].

1.3 Severe Plastic Deformation

In the past few decades, the mechanical properties of materials being improved through grain refinement by means of severe plastic deformation (SPD) attracted a lot of attention. A reduction in grain size to the submicrometer level has two significant advantages; first, there is an increase in the tensile strength through the Hall-Petch relationship at low temperatures,

with little or no corresponding reduction in the overall ductility. Second, if the ultrafine grains are stable at temperatures where diffusion is reasonably rapid, there is the possibility of achieving superplasticity at very high strain rates. Since then SPD has been widely used to fabricate bulk ultra-fine grained (UFG) metallic alloys with remarkably high strength and tolerable ductility for structural application at low and moderate temperatures. Several techniques are now available for producing the necessary high strains, including Equal Channel Angular Pressing (ECAP), High Pressure Torsion loading (HPT) [Zhilyaev 2008], high energy ball milling [Koch 1992], sliding wear [Rigney 1988] and Confined Channel Die pressing (CCDP) [Hu 2008]. As the best-established method with the highest efficiency, ECAP will be described in more details below, followed by a specific introduction to CCDP, which was utilized in this study.

1.3.1 ECAP

During ECAP, a billet of material is pressed through a die having two identical channels, which intersect at a certain angle. Various possible arrangements of these channels are illustrated in the schematic of Figure 1.4 [Valiev 2006]. Ideally, a billet experiences simple shear without any change in cross-sectional area upon passage through the intersection of the die channels, and the progress is therefore amenable to repetition. The following formula gives the equivalent strain of ECAP,

$$\varepsilon_{ECAP} = N \cdot \frac{2\cot(\phi/2 + \varphi/2 + \varphi cosec\left(\phi/2 + \varphi/2\right))}{\sqrt{3}}$$

where N is the number of ECAP passes and $\boldsymbol{\phi}$ the angle between the intersecting channels. (Fig.1.4). For $\boldsymbol{\phi}$ =90°, $\boldsymbol{\varphi}$ = 20°, the strain value approximately equals to 1 for each pass [Iwahashi 1996]. Four distinct procedures for repetitive pressings are identified in Figure 1.5. It was demonstrated that the evolution of microstructure occurred most rapidly and homogeneously when using route B_c [Komura 1999, Furukawa 1998, Molodova 2008].

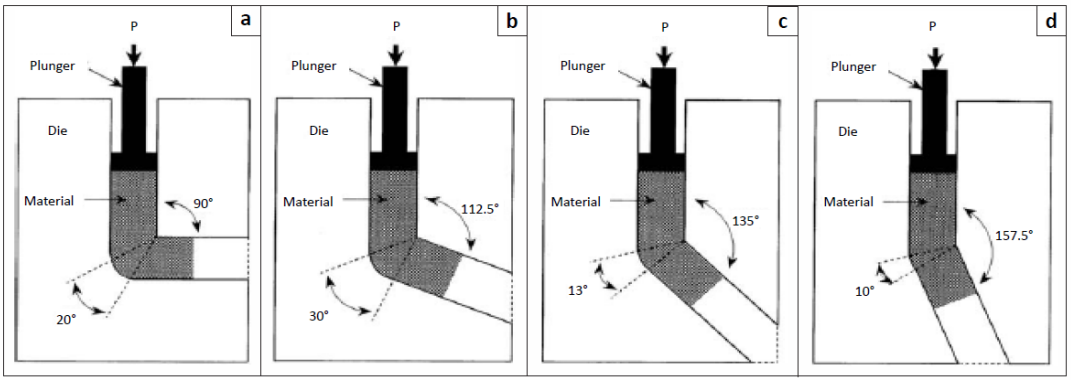

Figure 1.4: Schematic illustrations of the dies with different channel angel: (a) 90°, (b) 112.5°, (c) 135°, (d) 157.5°.

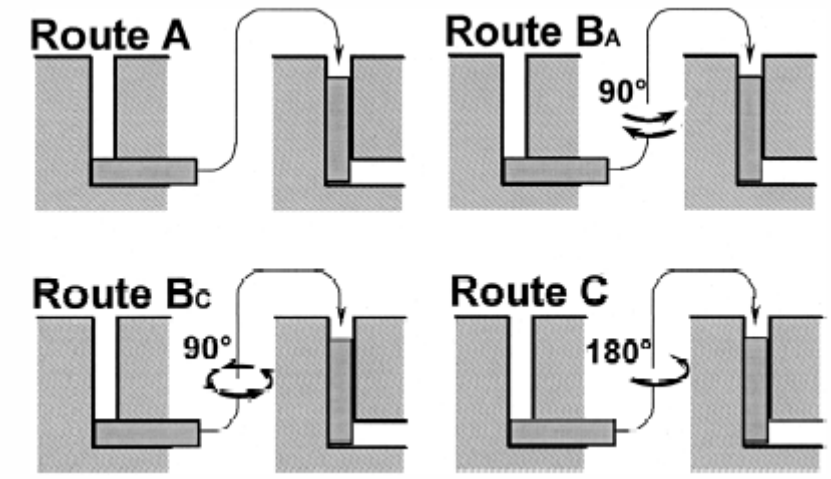

Figure 1.5: Schematic illustrations of each of four processing routes for repetitive ECAP.

1.3.2 CCDP

Confined channel die pressing is a special variant of channel die pressing. Conveying a large equivalent strain to the specimen by each pass in compression, it eventually leads to an ultrafine microstructure after several passes.

The geometry of specimens used for CCDP is usually a cuboid whose initial length is identical with the width of the die. Figure 1.6 shows a schematic illustration of the CCDP set-up. It is noted that the geometry of the specimen remains (more or less, due to friction) the

same before and after each pass, thus gives the possibility to subject the specimen to successive passes by rotating the specimen by 90°. Specifically, in the first pass, a compression load is applied along the A-axis and the materials flows along the A and C surface. Before the second pass, the specimen is rotated successively around the C-axis and then B-axis by 90°. The specimen is then subjected to a compression load along the B-axis, leading to material flow in the B and A surface. The same procedure is repeated in the third pass and after that, the material has regained its original geometry (with each facet being identical with the origin facet), as shown in Figure 1.7, denoted as route 2. It should be mentioned that there is an alternative route 1 for CCDP, which does not rotate the specimen during repetitive compressions. Hu et al. suggested that the effect of grain refinement for route 2 is more pronounced than route 1 [Hu 2008].

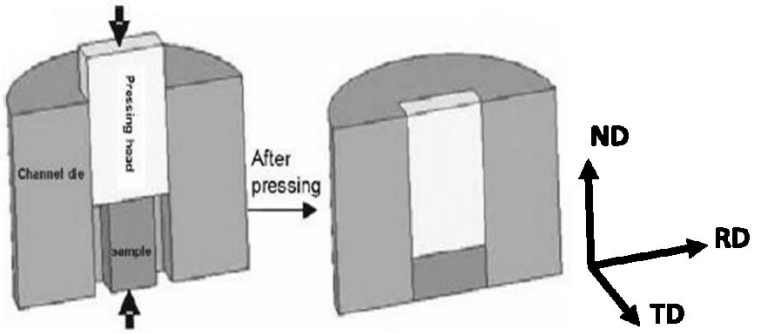

Figure 1.6: Schematic view of CCDP die with sample before and after pressing.

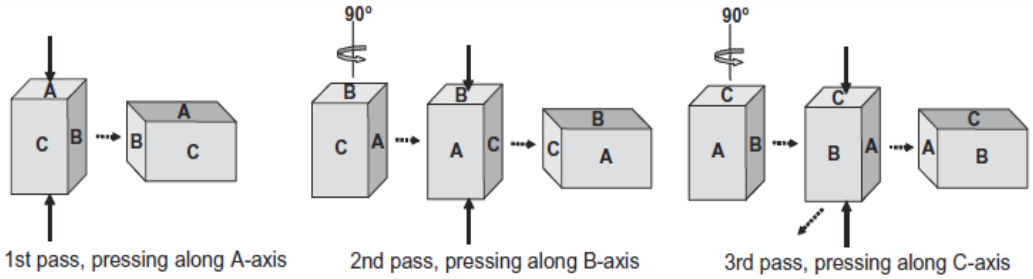

Figure 1.7: Schematic of CCDP strain path between consecutive pressings.

CCDP generates severe plastic deformation by accumulating equal strain step by step, and therefore is usually referred as discontinuous SPD technique. Although it is very effective way to fabricate bulk UFG materials, it has also disadvantages such as heterogeneity of strain distribution after deformation, resulting from friction between specimen surfaces and dies.

More precisely, each compression conveys a mean von Mises equivalent strain of 0.33 to the specimen [Chovet 2002]. A finite element study revealed that the central region of each billet undergoes the highest, but also a homogeneous deformation with a von Mises strain of > 0.7 [Zhang 2009, Zhang 2010].

1.3.3 Comparison of Methods

A comparison was made between ECAP and CCDP. The conclusions revealed advantages and disadvantages of both methods [Berghammer 2011]. The strongly inhomogeneous plastic strain distribution caused by CCDP confined a homogeneous UFG microstructure merely to a small area (central volume fraction of 5% of the sample). By contrast, a pure shear of the whole cross-section during ECAP led to a relatively homogeneous deformation throughout the sample. At a comparable equivalent strain, samples subject to ECAP were more effectively refined, and a higher fraction of high angle grain boundaries was obtained than by CCDP. On the other hand, with respect to the ease of l manufacturing practice, for ECAP a high force is needed and therefore the die cracks occasionally, whereas the CCDP process is simpler and easier to implement, especially for high pass deformation. With the arguments given above, CCDP was chosen as the SPD technic in current study for convenience. The low strain efficiency was compensated by using high numbers of CCDP passes. Since the effects on microstructure evolution are comparable, the results can be related to the numerous investigations by means of ECAP.

1.3.4 As-SPD feature

Extensive investigations have demonstrated the effective microstructure evolution and grain refinement during SPD. In Aluminum, for example [Terhune 2002, Iwahashi 1997, May 2005], the initial grain size of 1 mm was reduced to the micrometer level after a single ECA pressing. The microstructure was not homogeneous and consisted of parallel bands of subgrains with very low angles of misorientation. Some areas showed relatively equiaxed

grains, whereas others exhibited an elongated grain structure. Subsequent three pressings generated nearly equiaxed grains, 1.2 μm in size. Up to 12 passes the grain size slightly decreased to about 1 μm. It was suggested that the formation of new grains in Al during SPD was attributed to grain subdivision and texture evolution, as well as local boundary migration [Sun 2000]. On the other hand, from a careful investigation of the pure Al by transmission electron microscopy processed by SPD, Chang et al. drew the conclusion [Chang 2000] that with increasing strain, polygonised dislocation walls transformed firstly into partially transformed boundaries (subgrain boundaries), and finally into grain boundaries. Dissociation of lattice dislocations was believed to cause the transformation to occur. The disorientation distributions indicated a further upward shift in boundary disorientation and a predominance of high-angle grain boundaries in the microstructure.

Similarities were revealed between the ECAP of dilute Al-Mg solid solution alloys and pure Al [Wang 1993]. A single passage through the die at room temperature introduced an array of subgrains, and these elongated subgrains were arranged in well-defined bands essentially parallel to the direction of maximum shear. The subgrains were delineated by boundaries having low angles of misorientation, but these boundaries transformed into high angle boundaries with subsequent pressings through the die. Finally, through high passes, the microstructure achieved a homogeneous and equiaxed arrangement of grains separated by high angle boundaries. The addition of Mg to the Aluminum matrix had some clear influences on microstructure evolution: First, with increasing Mg content, more pressings were needed to establish a homogeneous microstructure in the material. Second, the ultimate grain size attained by SPD decreased with increasing addition of Mg, and this reduction was exceptionally marked. Third, the Mg addition had a strong influence on the recovery properties of the Al matrix. As a consequence of lower recovery, the dislocation density was increased and led to an increase of the proof stress over a wide range of strain [Iwahashi 1998, Gubicza 2004].

Since the grain refinement led to an increase in the overall strength and ductility at failure, the microstructural stability of the UFG material was of interest with respect to its potential for superplastic processing [Lee 2002]. The results from different studies confirmed the same evolution during high-temperature annealing: dislocation annihilation and recovery occurred

at first, producing low angle boundaries; the elongated grains evolved towards an equiaxed state; at relatively higher temperature, recrystallization took place inhomogeneously leading to a duplex structure [Morris 2002]. Wang et. al. exposed an Al-3%Mg alloy after 4 passes of ECAP to static annealing over a range of temperatures from 443K to 803K [Wang 1996]. The results revealed that the microstructure contained many 'non-equilibrium' grain boundaries, and recrystallization took place at higher temperatures giving rise to large grains with boundaries having high angle equilibrium confiugrations. A temperature of ~500K, close to half the absolute melting temperature, was regarded as an effective upper limit for utilization of the ultrafine grain structure in the material.

The nature of the non-equilibrium grain boundaries, as the feature of SPDed microstructure, was clearly associated with the underlying deformation mechanism underneath. Horita used high resolution electron microscopy to examine the structure of grain boundaries in an Al-Mg alloy after SPD [Horita 1880]. Besides the high energy non-equilibrium configuration, it was observed that the grain boundaries were mostly curved or wavy along their length, and some portions were corrugated with regular or irregular arrangements of facets and steps. By means of diffusion experiments ranging from 493 to 723K, it was revealed that the interdiffusion coefficients tended to be higher in as-ECAP fine-grained alloys having high fractions of high-angle boundaries [Fujita 2004], which implied the significant role that grain boundaries play during elevated temperature.

2. Experimental

2.1 Components

According to the phase diagram, at most 17.4 wt% Mg could be dissolved in Al at 450°C, see Figure 2.1. However, the room temperature solubility of Mg in Al is quite small, i.e. less than 1.8 wt%. The surplus Mg will either stay in solid solution in a super-saturated state or will precipitate out of the solid solution as second phase particle (Al_3Mg_2). In reality, with proper annealing and quenching conditions, up to 5.5 wt% of Mg can be kept in solution in a supersaturated state in the Al matrix at room temperature, which strongly increases the alloy strength by solid solution hardening.

Industrial experience indicates that alloys containing more than 5 wt% Mg are not appropriate to be utilized in cold worked condition due to their susceptibility to stress corrosion. Therefore, in the current study, Al-Mg alloys with Mg concentrations of 0.5%, 1%, 1.5%, 2%, 4% and 5% were investigated.

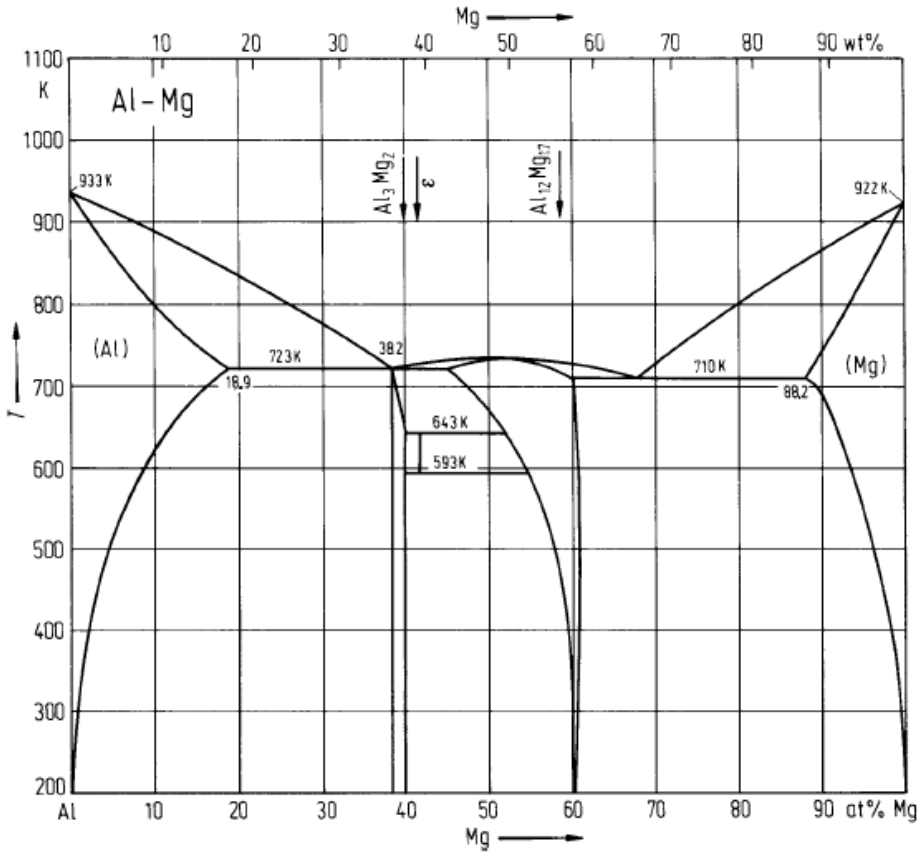

Figure 2.1: Al-Mg binary phase diagram.

2.2 Cast Ingot Preparation

Al-Mg alloys in the present work were produced from aluminum and magnesium of high purity (99.9999) in an induction furnace and gravity casting in 600 hPa Argon atmosphere, using a copper mould with boron nitride coating. The cast ingots were solution annealed at 470°C for 24 hours in air, then quenched in ice water. As evident from the TEM observations all Mg was dissolved in the alloy without detectable precipitation, which means, the Al-Mg alloys with Mg contents ranging from 0.5 to 5 wt.% were actually in a supersaturated solid solution state. Besides, pure Al with industrial purity ($\geq$ 99.99%) was utilized as reference material.

2.3 CCDP

From the as heat-treated Al-Mg ingots cuboidal samples with dimension $9 \times 9 \times 12\ mm^3$ were machined for confined channel die pressing (CCDP). CCDP was conducted in a Zwick 1484 mechanical testing machine at room temperature (Figure 3.2). The force and displacement were recorded with specific load sensors and extensometers, respectively. The applied strain rate was around $10^{-3}s^{-1}$, following route II for 1, 3, 6, 9, 12 and 18 passes, respectively, denoted later as P1, P3… P18. It is noteworthy here that, because of its relatively poor ductility, Al-5Mg could not endure 18 passes of CCDP. Prominent interior cracks were initiated due to stress concentrations.

Due to friction the strain distribution in the samples was inhomogeneous, decreasing from the central region (70% per pass) to the edges. The central volume ($3 \times 3 \times 3\ mm^3$) which experienced the highest deformation was used for mechanical testing and microstructure observation. A more detailed description of the CCDP process can be found in refs. [Chovet 2002, Zhang 2010].

2.4 Microcharacterization

2.4.1 Transmission Electron Microscopy (TEM)

Due to the high deformation degree an ultrafine grain structure developed in the as-CCDPed samples. Therefore, most microstructure characterization was conducted by TEM. TEM foils of 3mm diameter and about 0.5mm thickness were sectioned from the central cuboid of the as-CCDPed specimen perpendicular to the long axis. After proper grinding and thickness reduction, the foils were then jet-polished by means of a TenuPol 5 with an electrolytic solution of 938ml methanol +50ml H_2SO_4 +12ml HF at -14°C and 28 Volt. The dislocation structure and precipitation state were revealed by bright field images at high magnification.

The grain size was measured as the boundary spacing (including cells, subgrains and grains) from dark field micrographs of more than 500 grains for each specimen. The misorientation evolution was determined from selected area diffraction (SAD) patterns.

2.4.2 Electron Backscatter Diffraction (EBSD)

For microstructure characterization of samples deformed at elevated temperatures, orientation microscopy by EBSD was utilized. Because dynamic recovery and recrystallization (RX) took place at elevated temperatures, the internal stresses were substantially reduced. The samples for EBSD were carefully prepared by twin-jet polishing, using a similar procedure as for TEM sample preparation, but with shorter polishing time (before the sample was perforated). Focused Ion beam (FIB) imaging with EBSD detector was applied to conduct the measurements.

2.4.3 X-ray Diffraction (XRD)

The macrotexture evolution during elevated temperature deformation was measured by XRD (Figure 2.2). The dog-bone-shaped tensile sample were ground (reducing the thickness from 1mm to half), followed by mechanical and electrolytic polishing. The undeformed samples were also prepared and measured in the same manner.

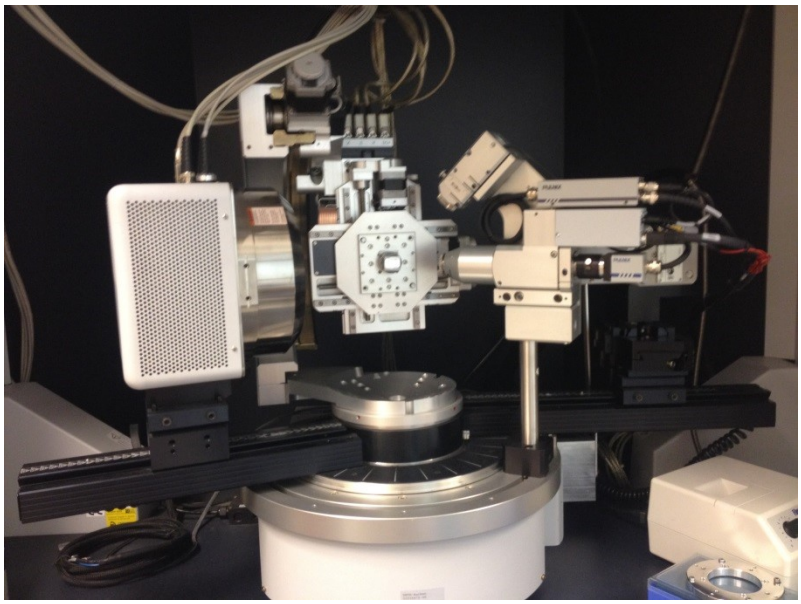

Figure 2.2: XRD experimental set-up with Texture Goniometer.

2.5 Mechanical tests

The impact of SPD on the mechanical properties of UFG Al-Mg alloys was investigated by tensile tests at room temperature and elevated temperatures (100°C, 200°C) at constant and changing strain rates. For every test, the temperature was monitored continuously and controlled to remain within a deviation of ± 1 K. Due to the limited ductility at room temperature, strain rate jump tests of as-CCDPed specimens were carried out by compression of cylindrical samples (ϕ1.5 * 2.25mm^3) cut parallel to the long axis of the as-CCDPed cuboids. Strain rate jump tests at elevated temperatures and all the constant rate tests were conducted by uniaxial tensile tests. The gauge volume was 3.54*1.5*1mm^3 with the tensile direction being parallel to the long axis of as-CCDPed cuboids. For all mechanical tests, the electromechanical DZM mechanical testing machine at IMM with different setups was utilized, shown in Figure 2.3. The stress noise of the device was less than 0.05MPa.

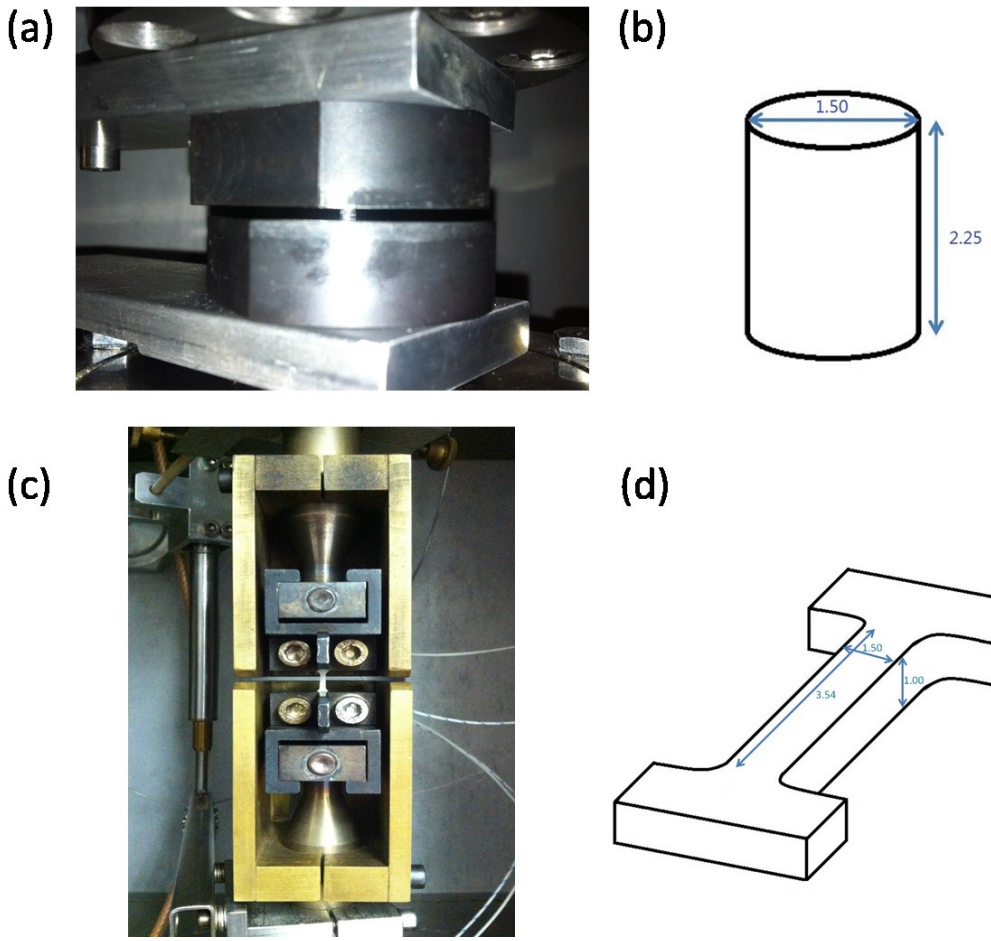

Figure 2.3: The experimental set-up (a) and sample geometry (b) of compression test; and the experimental set-up (c) and sample geometry (d) of tensile test of DZM.

2.5.1 Strain Rate Jump Tests (SRJT)

On the one hand to avoid issues related to the load history, on the other hand, to obtain extensive data from one single test sample, SRJT are widely used as an effective means of mechanical tests: a base strain rate is applied for a period of time, followed by an instantaneous jump to a different strain rate, which is maintained for another period of time. Given the limited ductility of Al-Mg alloys at room temperature, the strain rate change tests were conducted in compression. Two rate-jump modes were utilized: (a) the strain rate changed alternatingly between $\dot{\varepsilon} = 10^{-3}s^{-1}$(at a true strain of 3 and 13%, respectively) and $\dot{\varepsilon} = 10^{-4}s^{-1}$(at 10 and 19%, respectively), denoted as double-rate tests; (b) the rate changed from an initial value of $\dot{\varepsilon} = 10^{-4}s^{-1}$ to $\dot{\varepsilon} = 10^{-3}s^{-1}$at a true strain of 3% and then to

$\dot{\varepsilon} = 5 * 10^{-5} s^{-1}$ at 10% followed by $\dot{\varepsilon} = 5 * 10^{-4} s^{-1}$at 13% and finally to $\dot{\varepsilon} = 10^{-4} s^{-1}$ at 16% (multi-rate tests). The different strain rate stages are illustrated in Figure 2.4.

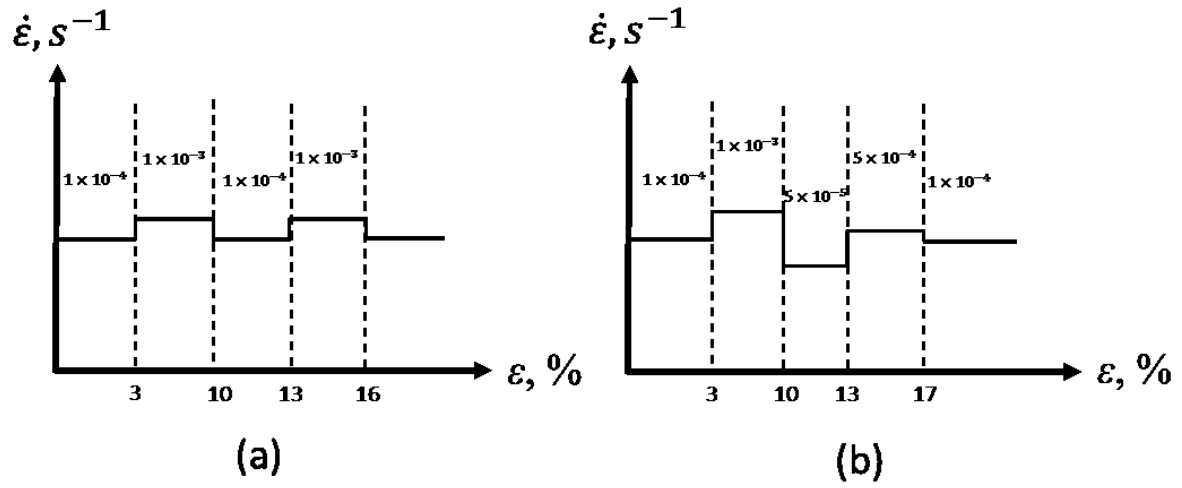

Figure 2.4: Schematic illustration of applied strain rate jump modes: (a) double-rate jump and (b) multi-rate jump tests.

The strain rate sensitivity (SRS), including instantaneous (m_i) and steady state (m_s) SRS, the flow stress response ($\Delta\sigma$), including instantaneous ($\Delta\sigma_i$) and steady state ($\Delta\sigma_s$) flow stress changes at the rate jump as well as the transient time (t_t) that passed during stress relaxation from the instantaneous response to the subsequent steady state were evaluated by double-rate tests. The definition of m_i, m_s, $\Delta\sigma_i$, $\Delta\sigma_s$ and t_t are illustrated schematically in Figure 2.5. The amplitude of the flow stress serrations (σ_{drop})and the PLC type were determined by multi-rate tests.

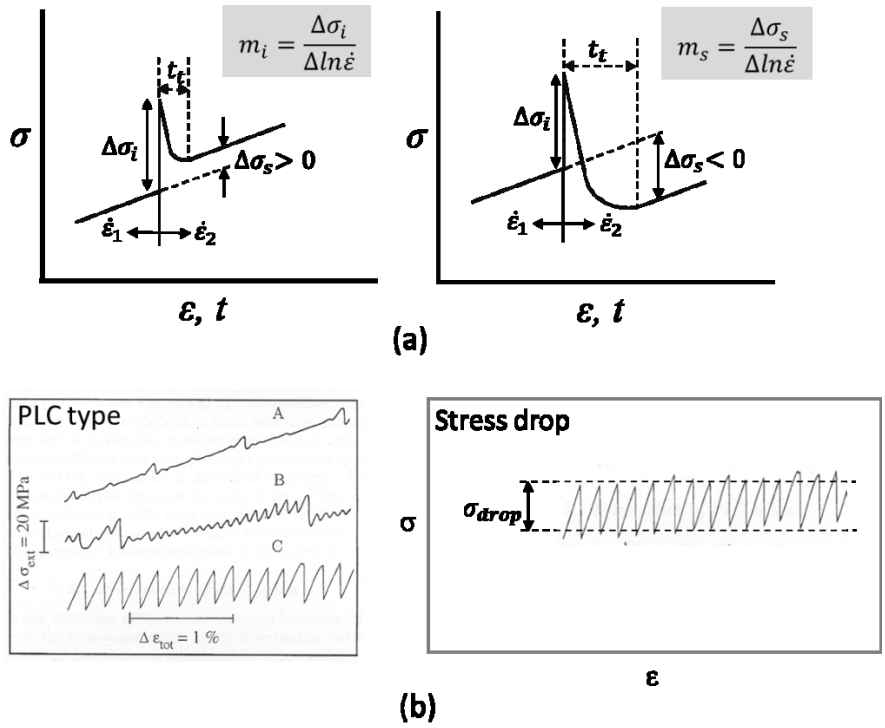

Figure 2.5: Schematic illustration and definition of instantaneous and steady state stress responses $\Delta\sigma_i$ and $\Delta\sigma_s$, strain rate sensitivity m_i and m_s and transient time t_t at a strain rate-up jump, where $\dot{\varepsilon}_1 < \dot{\varepsilon}_2$ for $\Delta\sigma > 0$ (left figure) and $\Delta\sigma < 0$ (right figure).). (b) Definition of PLC type and stress drop σ_{drop} (stress serration).

2.5.2 Tensile tests at elevated temperatures

Tensile tests at different temperatures were performed at constant strain rates of $10^{-3}s^{-1}, 10^{-4}s^{-1}$ *and* $10^{-5}s^{-1}$, respectively. For all elevated temperature tests, the samples were first mounted and then heated by heat conduction through the clamps to distinct target temperatures. Although the heat conduction from the clamps to the specimen was very effective, a certain time was necessary to make sure the whole sample reached equilibrium at the desired temperature. The heating process lasted a few minutes depending on the target temperature. The respective values are listed in Table 2.1.

Table 2.1: Heating time needed for different testing temperatures.

Experimental temperature (℃)	Waiting time (min)
50	9-10
100	11-12
200	16-17

3. Results

3.1 Microstructure

3.1.1 Experimental techniques and microstructural phenomena

Due to the high deformation degree and, thus, the ultrafine grain size of the as-CCDPed samples, it was not possible to achieve a satisfactory indexing rate by EBSD. Therefore, the microstructure evolution with progressing CCDP pass was mainly characterized by TEM. By bright field (BF) imaging the fine microstructure, e.g. dislocation structure and precipitation state, were revealed at high magnification. The grain size was determined from the boundary spacing (including cells, subgrains and grains) via dark field (DF) micrographs, with more than 500 grains for each specimen. The misorientation evolution was analyzed by selected area diffraction (SAD) patterns. However, EBSD measurements could be conducted in as-CCDPed pure Al samples, due to the recovered or even recrystallized microstructure. Further grain refinement was therefore impossible, and the dislocation density decreased at the same time. In the first section on micro characterization the evolution of microstructure in dependence of CCDP pass number and Mg content will be addressed.

The deformed structure introduced by CCDP at room temperature remained stable at ambient temperature. However, with increasing deformation temperature, the non-equilibrium, high-energy deformed structure was subjected to a tendency to change to a lower energy state by structural rearrangements during recovery, recrystallization, and grain growth [Gottstein 2004]. The microstructural heterogeneity after deformation is a characteristic feature of UFG material and expected to affect those softening processes and, thus, to influence the mechanical properties of the material. It has been reported that a high tensile ductility or even superplasticity can be achieved in materials with grain size ~ 1- 10µm [Chokshi 1993]. Moreover, with a grain size in the sub micrometer or nanometer regime, an increase in the

overall ductility was obtained by concurrently decreasing the strain rate or increasing the temperature. In this study, a major purpose of the characterization work of specimens subjected to elevated temperature deformation was, besides probing the thermal stability of the as-CCDPed Al-Mg alloys, to find a processing window for an economic forming operation to obtain the optimal mechanical properties.

For the sake of brevity, only the results on Al-1Mg, Al-2Mg and Al-5Mg will be presented in this chapter.

3.1.2 Micro characterization after room temperature deformation

3.1.2.1 Al-1Mg

The BF images combined with the corresponding SAD patterns are presented in Figure 3.1, revealing the microstructure of Al-1Mg alloy after specific CCDP passes. The first CCDP pass generated a cellular dislocation structure with a high density of dislocations in the cell boundaries but a relatively low density of dislocations within the cell interior (Figure 3.1 (a)). With rising number of CCDP passes, e.g. after 3 passes, the cells became elongated parallel to the shear direction. The cell size decreased, and the thickness of the cell walls also shrunk. The cell structure was no longer dominating after 4 passes and became replaced by a larger fraction of subgrains separated by low angle grain boundaries (LAGBs) (Figure 3.1 (b, c, d)). This structural development was accompanied by an increasing misorientation, as evident from the SAD patterns. For medium imposed strains, e.g. 6 to 9 passes, the azimuthal spread of some diffraction spots suggested that the grains contained subgrain boundaries with small misorientations or an intense strain field. As the LAGBs became predominant and the misorientation grew, the SAD patterns tended to appear circular. The SAD patterns were obtained by using a specific micrometer aperture, which included diffraction spots from numerous grains. Thus, the measured spot spreading did not constitute a quantitative measure of the misorientations between neighboring grains. Nevertheless, by maintaining a constant

aperture size, this spreading could be used as a qualitative measure of the evolution of the boundary misorientation with increasing number of CCDP passes.

For low Mg concentration alloys, pronounced dynamic recovery was expected to take place, since the solute content was too small to substantially impede cross slip. This resulted in an increase of misorientation during the process of polygonization, which was observed by BF imaging (Figure 3.2). The dislocation cell walls first transformed into LAGBs and subsequently to high angle grain boundaries. The observed thickness fringes in both samples indicated a high misorientation between the adjacent grains.

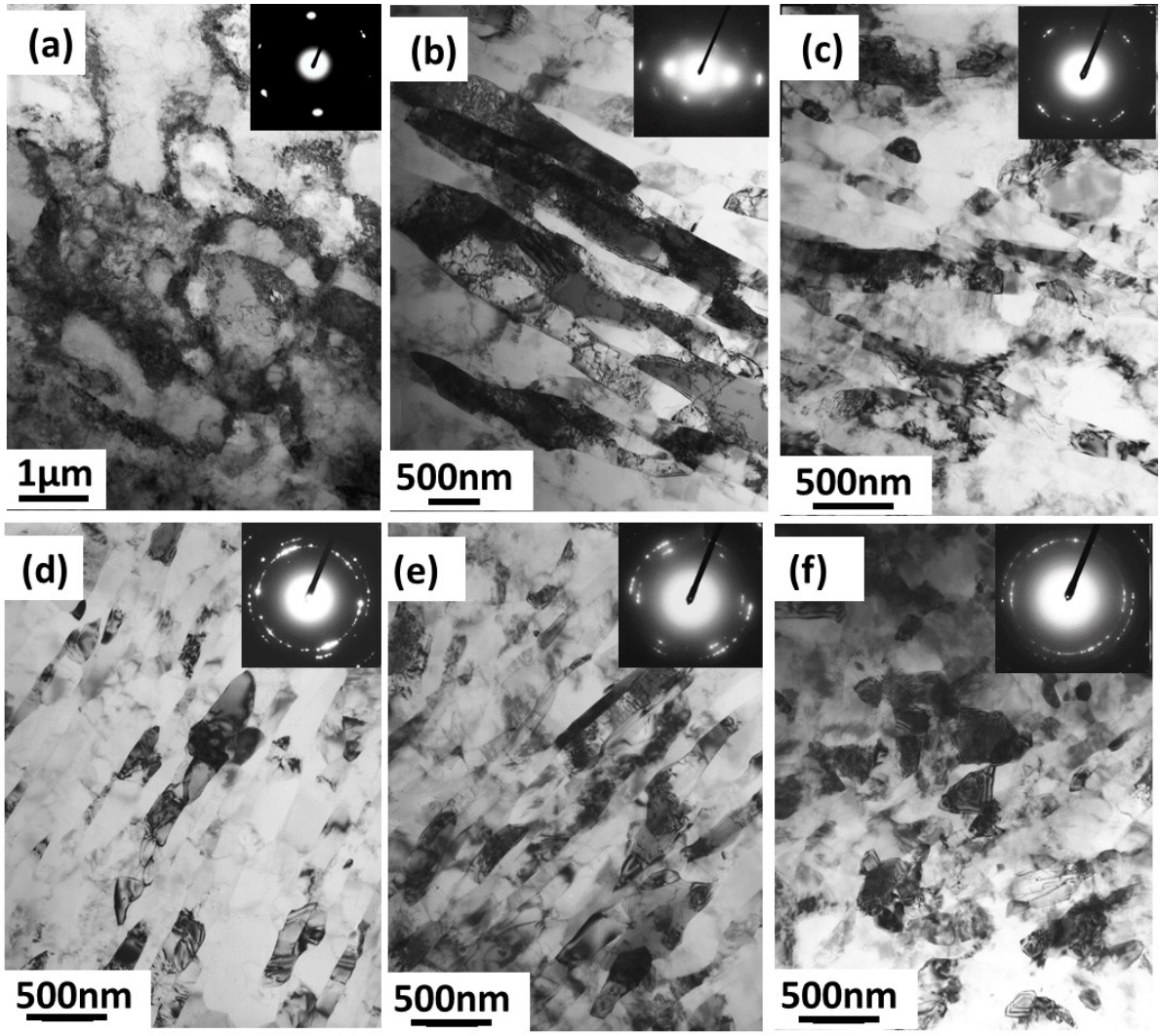

Figure 3.1: Bright field images and corresponding SAD patterns of Al-1Mg alloy: (a) P1; (b) P3; (c) P6; (d) P9; (e) P12; (f) P18.

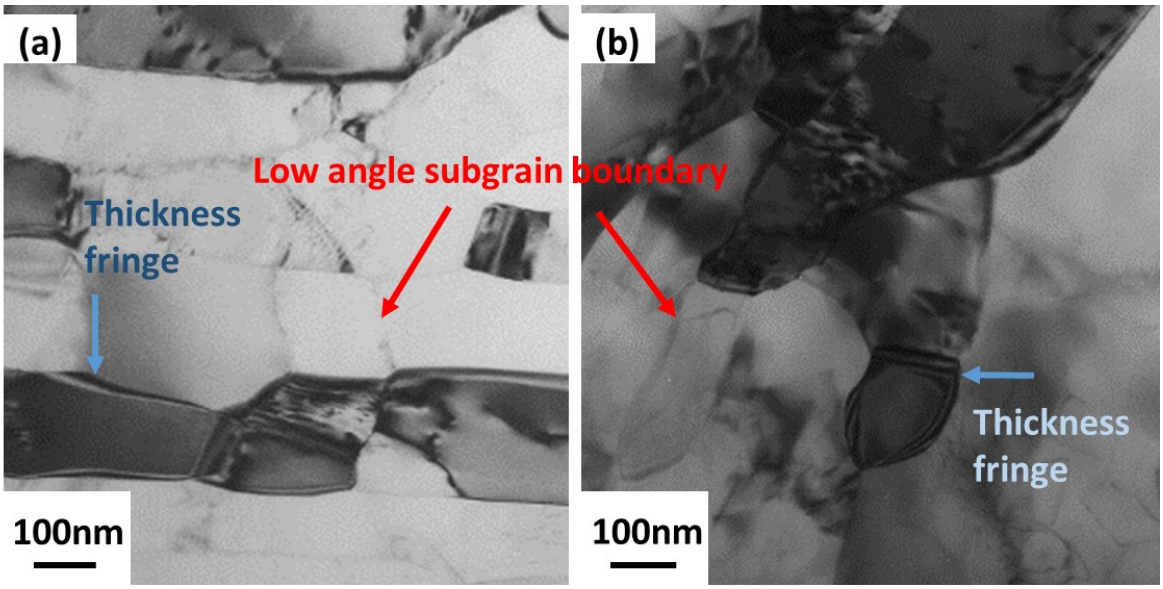

Figure 3.2: Recovered microstructure observed in Al-1Mg by bright field imaging, (a) Al-1Mg P9, (b) Al-1Mg P18.

Grain size measurements of Al-1Mg were conducted by the line intercept method from DF images without differentiating between low angle and high angle boundaries. The grain size distributions are depicted in Figure 3.3. The evolution of the mean grain size with rising CCDP pass number is also given. Obviously, the grain size was refined down to an ultrafine scale (300~400nm) and exhibited a monotonically decreasing trend with progressing CCDP. The slope of the curve, i.e. the refinement rate, decreased which indicated that grain refinement became less efficient at higher SPD strains.

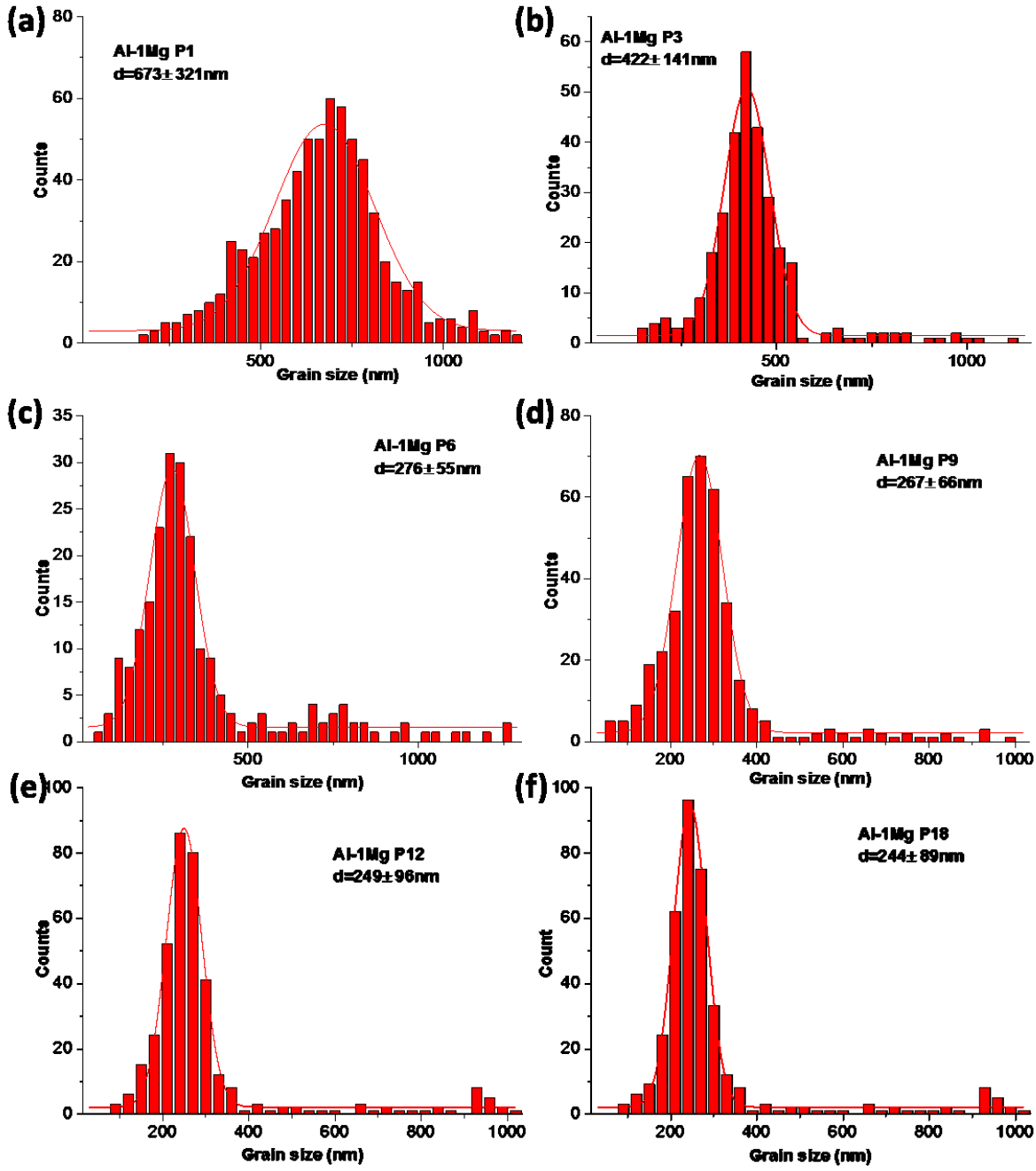

Figure 3.3: Grain size distributions and their evolution with CCDP pass number of Al-1Mg alloy: (a) P1; (b) P3; (c) P6; (d) P9; (e) P12; (f) P18.

3.1.2.2 Al-2Mg

The microstructure of Al-2Mg (Figure 3.4) was similar to that of Al-1Mg, only finer because the higher Mg content impeded more strongly dynamic recovery. The microstructure changed

gradually from a deformed dislocation cell structure (Figure 3.4. (a), P1) with a single crystal type diffraction pattern, to a subgrain structure marked by emerging diffraction rings (Figure 3.4. (c), P6), and finally to a polycrystalline material with high angle boundaries with complete diffraction rings (Figure 3.4. (f), P18).

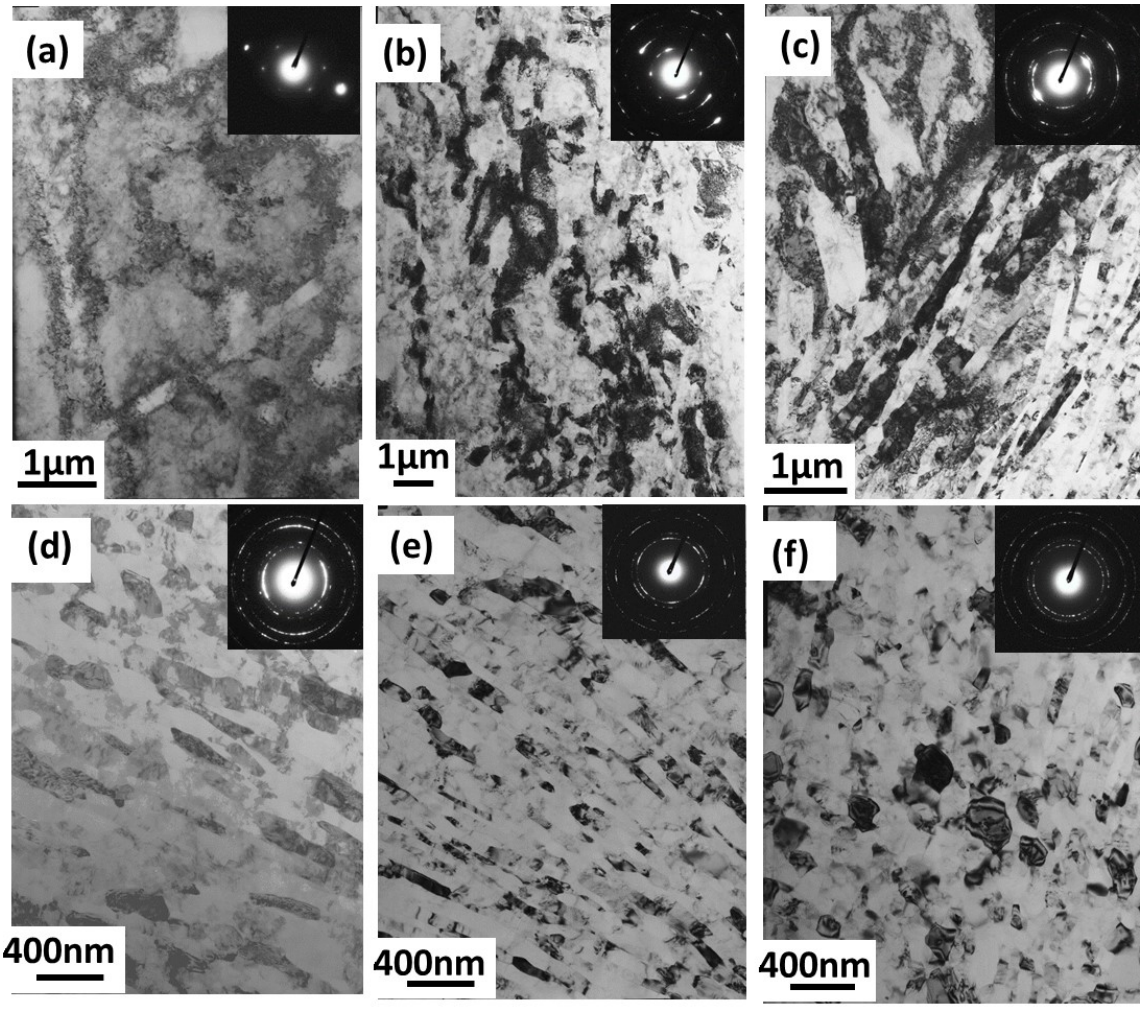

Figure 3.4: Bright field images and corresponding SAD patterns of Al-2Mg alloy: (a) P1; (b) P3; (c) P6; (d) P9; (e) P12; (f) P18.

The dislocation rearrangement and the recovery progress of Al-2Mg were also monitored by TEM observations. Recovery (polygonization) took place during CCDP of Al-2Mg (Figure 3.5), along with a decrease of the dislocation density and the formation of specific dislocation patterns, e.g. networks of low-angle grain boundaries. The grain size distribution and its evolution with progressing CCDP pass are shown in Figure 3.6. It is noticed that the finally obtained refined grain size was smaller than for Al-1Mg.

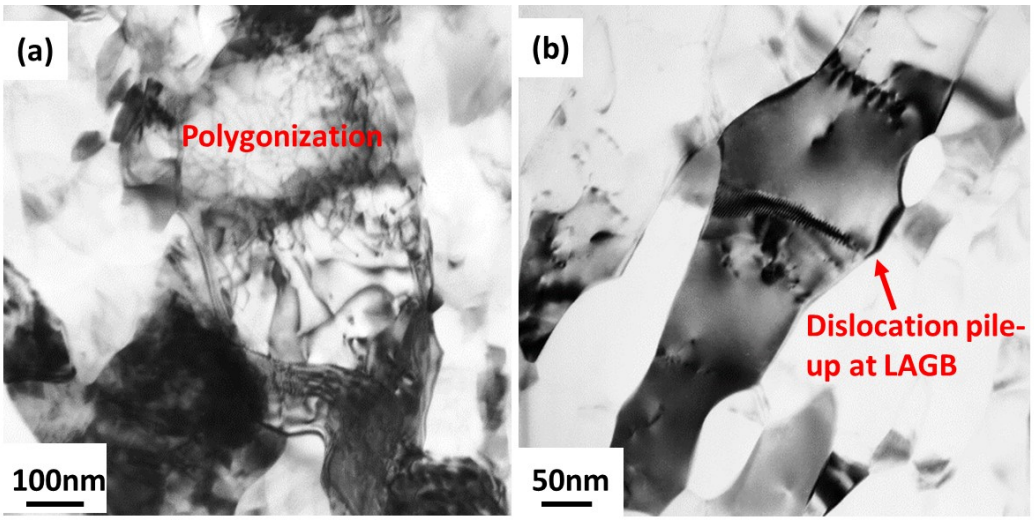

Figure 3.5: Recovered structure observed in Al-2Mg, bright field image, (a) Al-2Mg P18, (b)Al-2Mg P18.

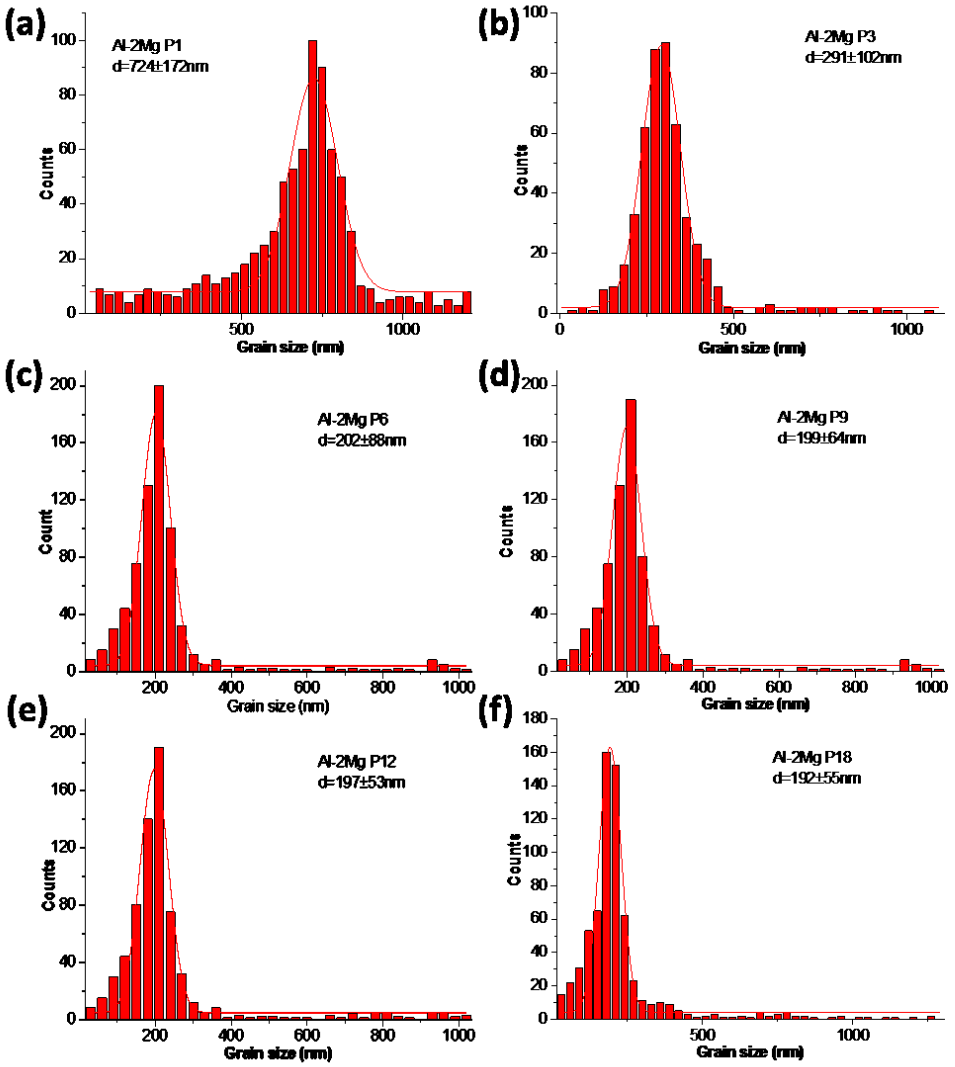

Figure 3.6: Grain size distributions and their evolution with CCDP pass number of Al-2Mg: (a) P1; (b) P3; (c) P6; (d) P9; (e) P12; (f) P18.

3.1.2.3 Al-5Mg

In general, the microstructure of Al-5Mg was very similar to Al-2Mg, only with finer grain size, see Figure 3.7. The grain size reached even down to 100nm after 6 passes, as evident from Figure 3.8. The SAD patterns of the high pass Al-5Mg samples indicated a high frequency of HAGBs. Unlike the HAGBs formed during static annealing i.e. by recrystallization, these HAGBs were formed during SPD and gradually evolved from cell and subgrain boundaries, and thus contained a high density of extrinsic grain boundary dislocations. Owing to their high energy and long range stress fields, they are also referred to as non-equilibrium grain boundaries [Horita 1996, Musalimov 1989]. Our TEM investigation confirmed those observations.

The grain refinement of Al-5Mg was most pronounced throughout the current study because of the highest Mg content. On the other hand, the Mg solutes also caused a difference between Al-1Mg and Al-5Mg in terms of the extent of recovery, i.e. Al-5Mg showed a much weaker recovery during SPD processing, which will be addressed later.

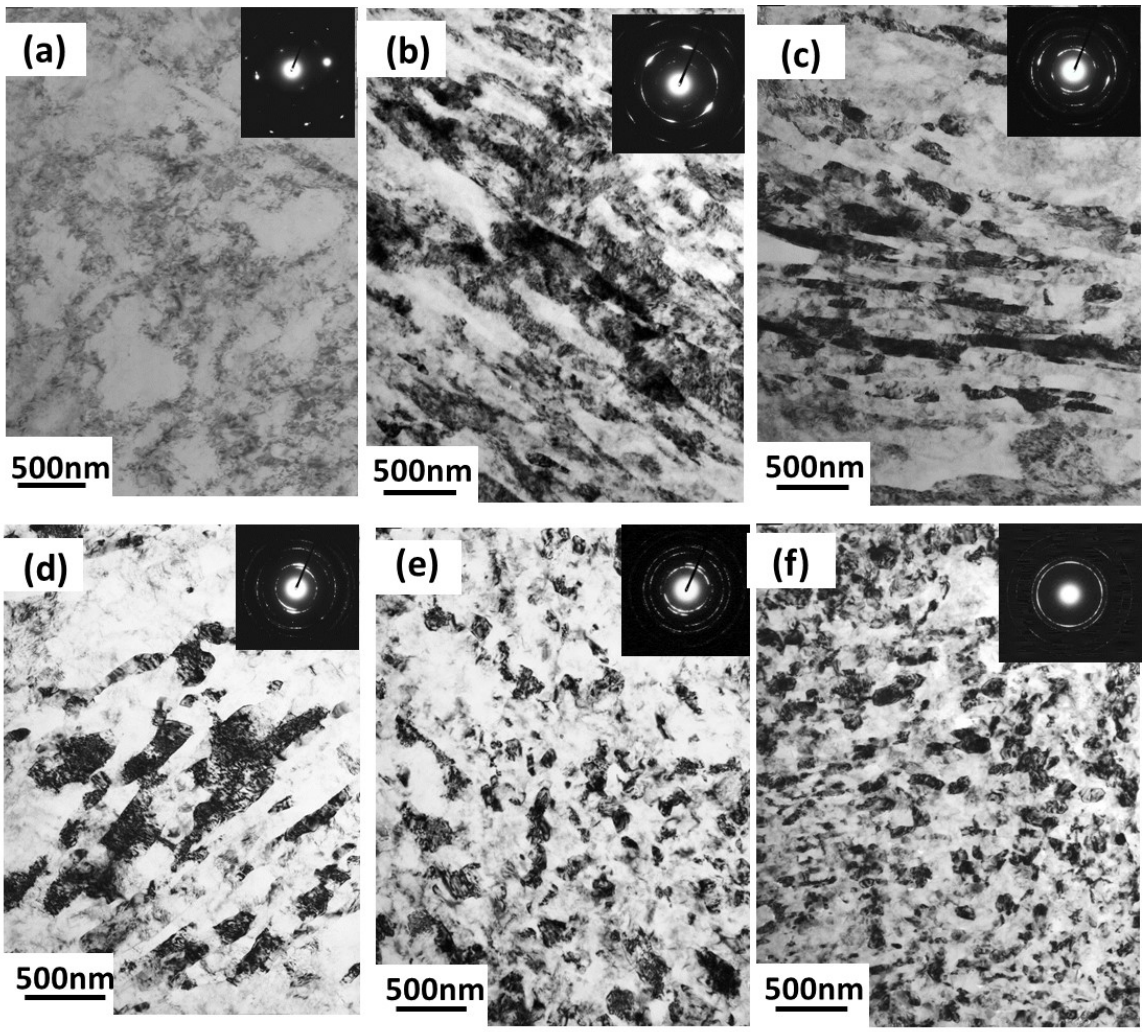

Figure 3.7: Bright field images and corresponding SAD patterns of Al-5Mg: (a) P1; (b) P3; (c) P6; (d) P9; (e) P12; (f) P18.

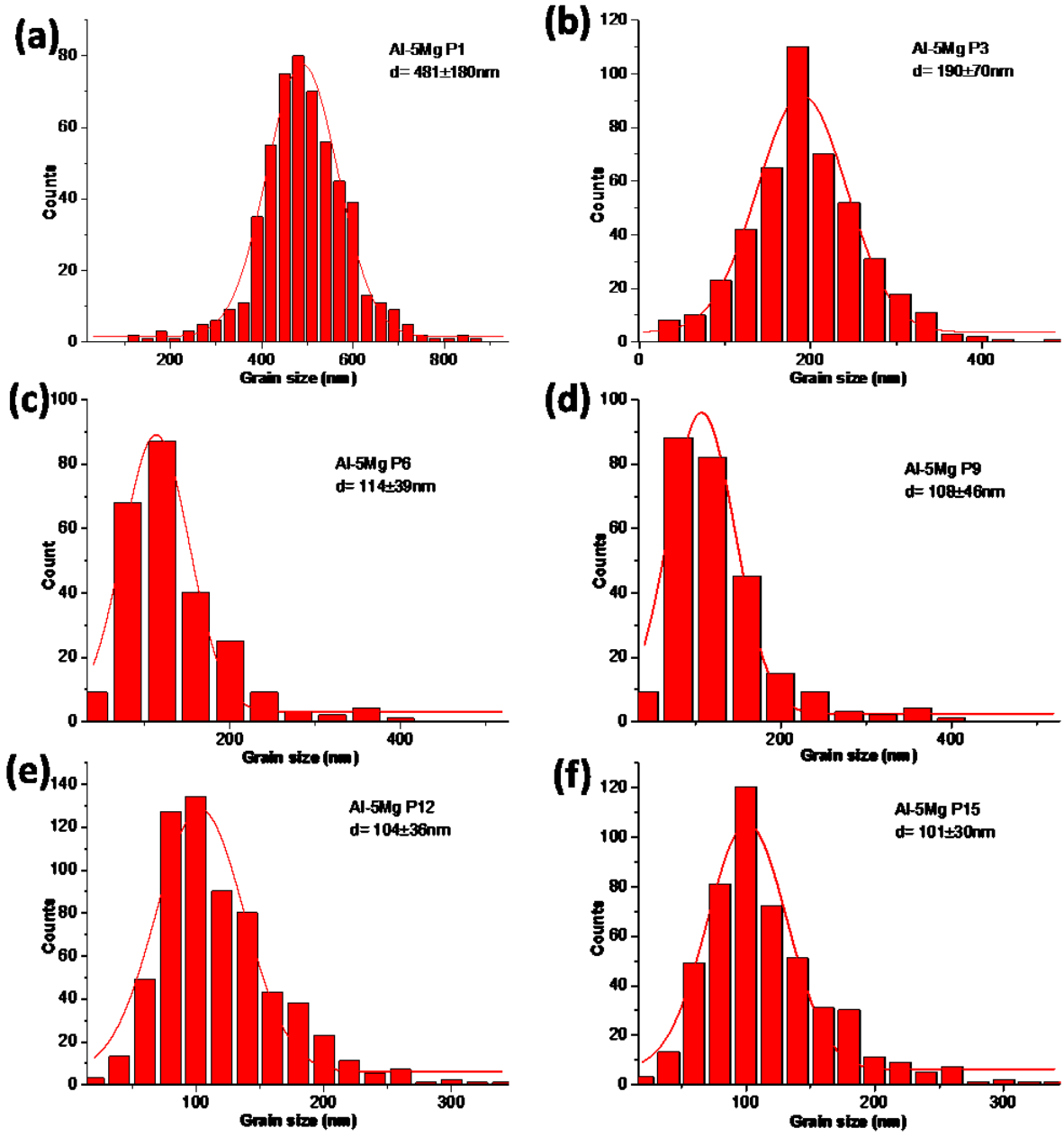

Figure 3.8: Grain size distributions and their evolution with increasing CCDP pass number of Al-5Mg: (a) P1; (b) P3; (c) P6; (d) P9; (e) P12; (f) P18.

3.1.2.4 RT ductility and fracture mechanism

The tensile ductility of Al-Mg alloys is heavily reduced by prior SPD. The elongation to fracture first decreases and then levels off with increasing SPD strain. The samples with high

Mg content even fractured before yielding after being subjected to a high number of passes. Some interior cracks had already been generated during CCDP processing, leading to catastrophic fracture during subsequent tensile deformation. To reveal the fracture mechanisms of UFG Al-Mg alloys, the fracture surfaces of Al-4Mg alloys were investigated by secondary electron imaging after several CCDP passes, see Figures 3.9 and 3.10, respectively.

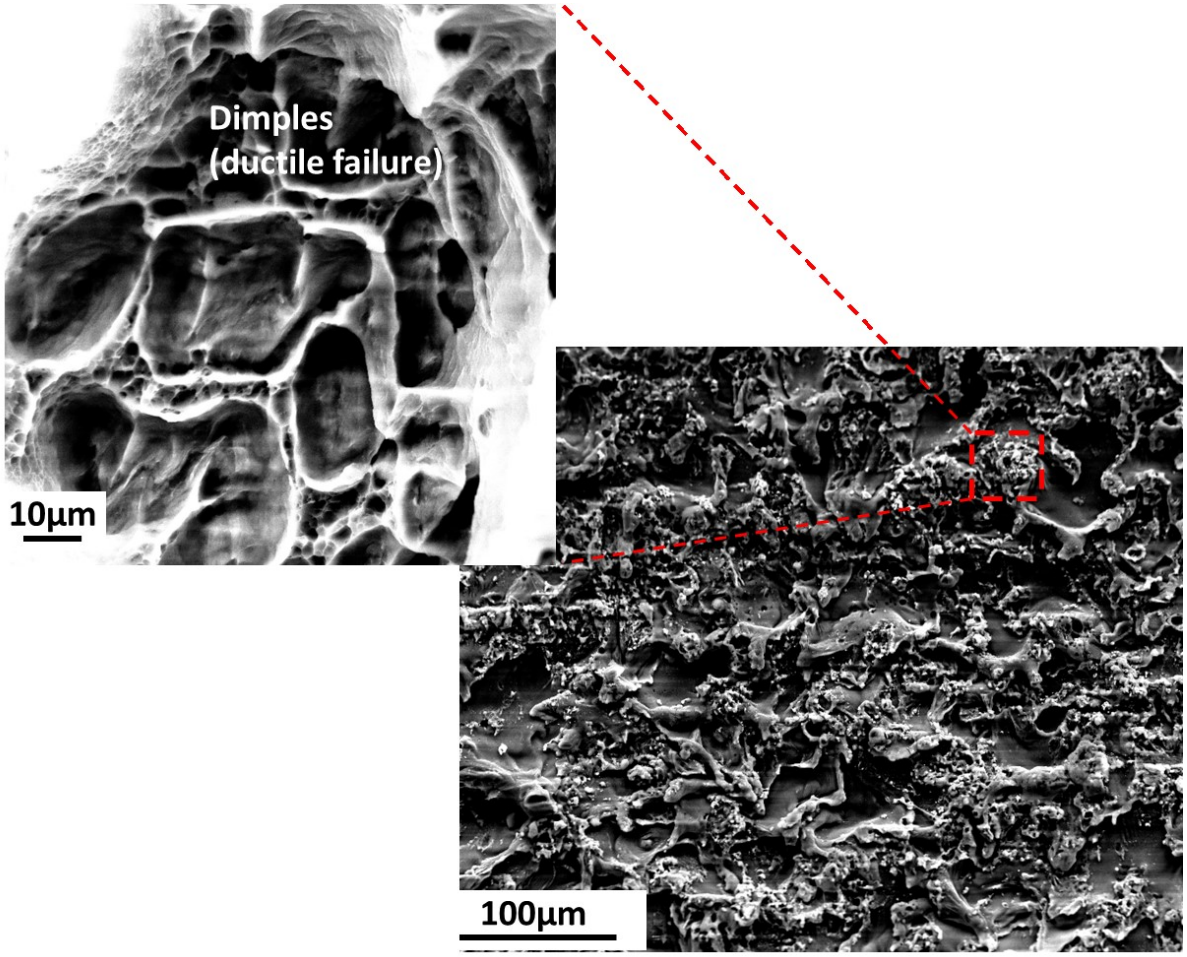

Figure 3.9: Fractography of Al-4Mg without pre-deformation, P0.

A typical ductile fracture surface with a high area fraction of dimples was observed for a coarse grained sample, P0 (Fig. 3.10).

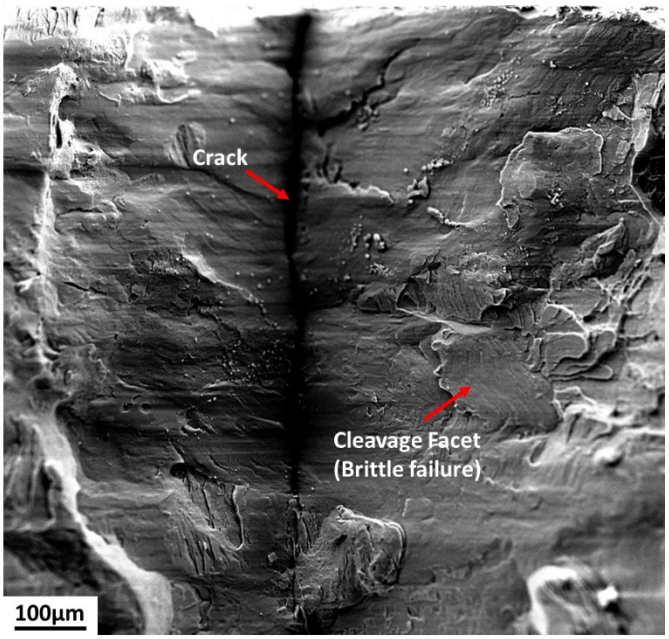

Figure 3.11: Tensile fracture topography of Al-4Mg after 9 passes of CCDP.

Highly predeformed UFG samples, e.g. P9 in Figure 3.11, revealed a fracture surface with mostly cleavage facets, indicative of transgranular brittle fracture.

3.1.3 Micro characterization after annealing

The microstructure of the studied Al-Mg alloys became significantly refined by CCDP, the grain size decreased down to 100 nanometers at room temperature. In this section the microstructure evolution of Al-1Mg and Al-5Mg through a series of annealing treatments at 100°C and 200°C are presented. For brevity, only micrographs of specimens with the highest deformation degree will be shown, because they possess the largest dislocation density and misorientation difference, which govern microstructure evolution during annealing. Samples with lower CCDP pass numbers exhibited the same trend, though.

3.1.3.1 Al-1Mg

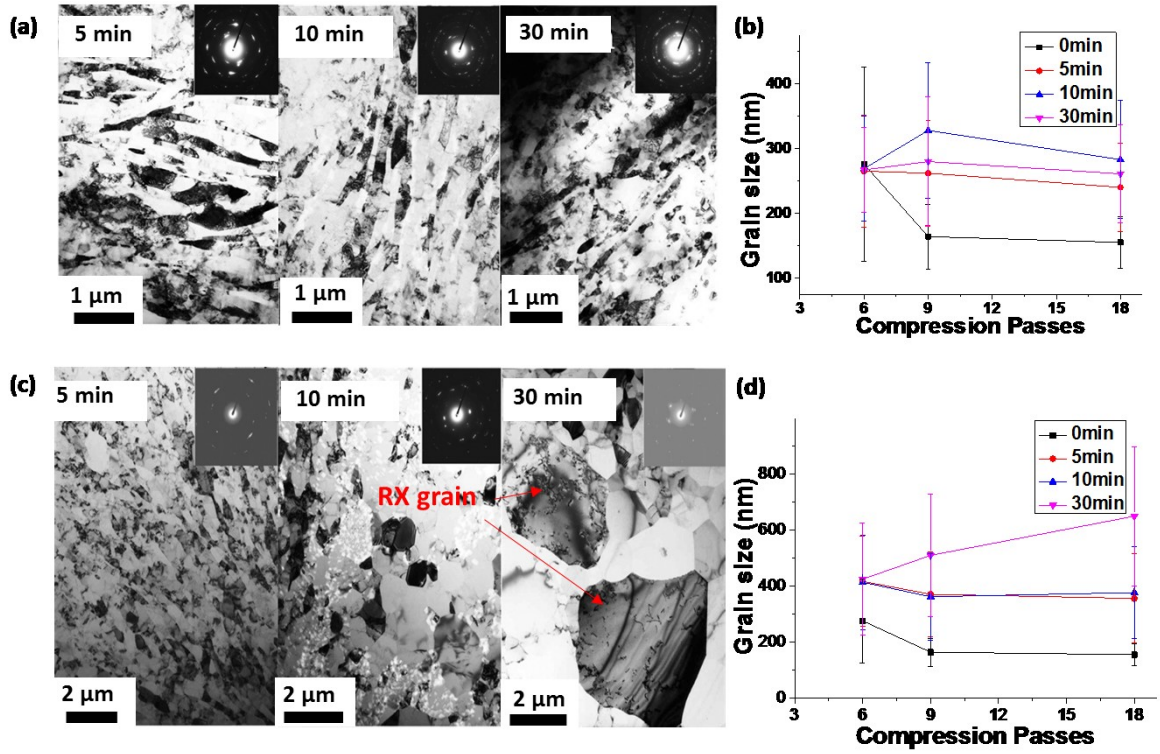

Figure 3.12: Microstructure evolution of Al-1Mg after 18 CCDP passes and static annealing at (a) 100°C, (b) corresponding grain size distribution after static annealing at 100°C, (c) 200°C, (d) corresponding grain size distribution after static annealing at 200°C.

Annealing of the most strongly strained samples, i.e. 18 CCDP passes for Al-1Mg, at 100°C and 200°C, respectively, revealed that at 100°C the microstructure retained its deformed character after annealing for 30 minutes. The subgrains and grains aligned along the shear direction, and the grain size distribution barely varied, see Figure 3.12 (a), (b). On the other hand, the microstructure changed dramatically within the same annealing time at 200°C. Recrystallization became recognizable after 10 minutes; with longer annealing time some grains of micrometer size were observed together with the prior fine-scale deformed grain matrix, forming a bimodal type microstructure, Figure 3.12(c). At 200°C within 10 minutes annealing the microstructure, the grain size, and its dependence on CCPD pass number did not change significantly, compared to their as-SPDed counterpart. Further increasing the annealing time promoted the progress of recovery and recrystallization. Accordingly, the average grain size increased with the rising CCDP pass number, due to the stored deformation energy. The newly recrystallized grains showed the tendency to grow larger than several micrometers, which caused an increased average grain size.

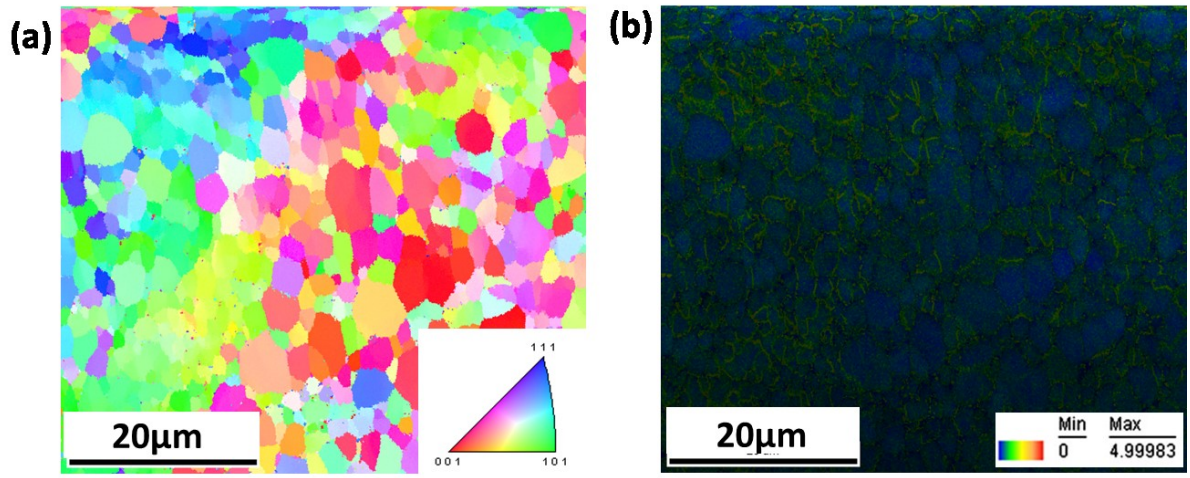

Figure 3.13: EBSD measurements of Al-1Mg P9 after annealing at 200°C, (a) inverse pole figure (IPF), and (b) kernel average misorientation (KAM) map.

After high temperature strain rate jump tests (SRJT) EBSD measurements revealed the dynamic microstructure evolution. The total heating time of the EBSD sample was around 30 minutes, comparable with the results of a 30 minutes statically annealed sample. In general, the sample deformed at elevated temperature exhibited a more homogeneous microstructure, Figure 3.13 (a). The KAM map (b) revealed more details along with the inverse pole figure (IPF): grains with low strain index were classified as recrystallized grains, mostly located in the central area with orientations close to (001), with <001> parallel to ND (Fig. 1.6); the strain index in the left and upper area is comparably higher, indicating the location of the former deformed structure, which is also consistent with their orientation i.e. (110), (111), with <011> and <111> parallel to TD and RD . The combination of recrystallized and deformed structure is well captured by EBSD measurements, unfortunately more details from the high strain area are not accessible by this technique. To obtain further quantitative information, XRD texture measurements of samples subjected to elevated temperature deformation were conducted. The Matlab system “Goniometer Tool” was utilized to calculate the orientation density and to determine the volume fractions of texture components. The corresponding pole figures and the misorientation distributions are presented below.

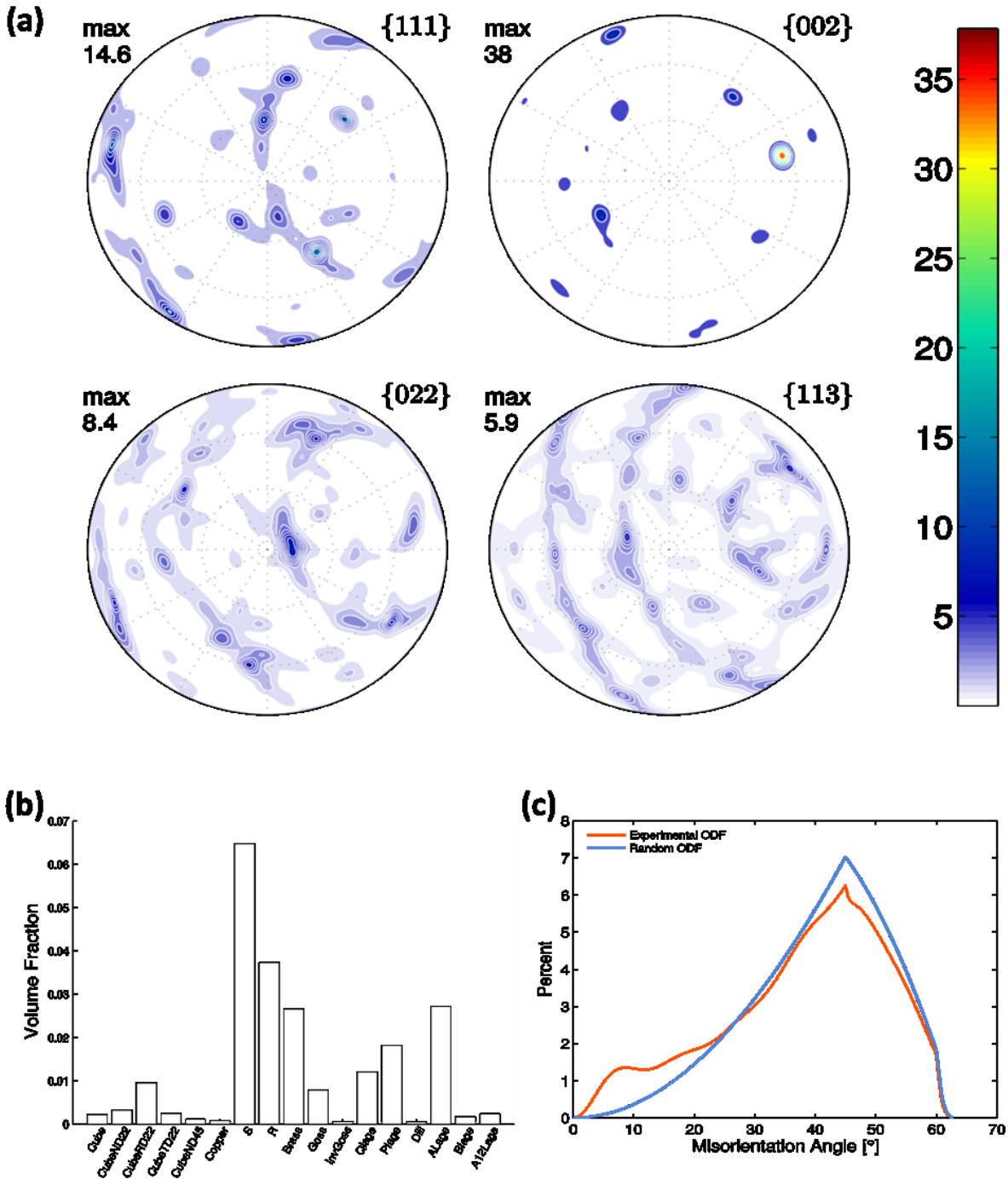

Figure 3.14: Texture analysis of Al-1Mg P9 sample after SRJT at 100°C, (a) pole figures, (b) volume fraction of various texture components, (c) misorientation distribution.

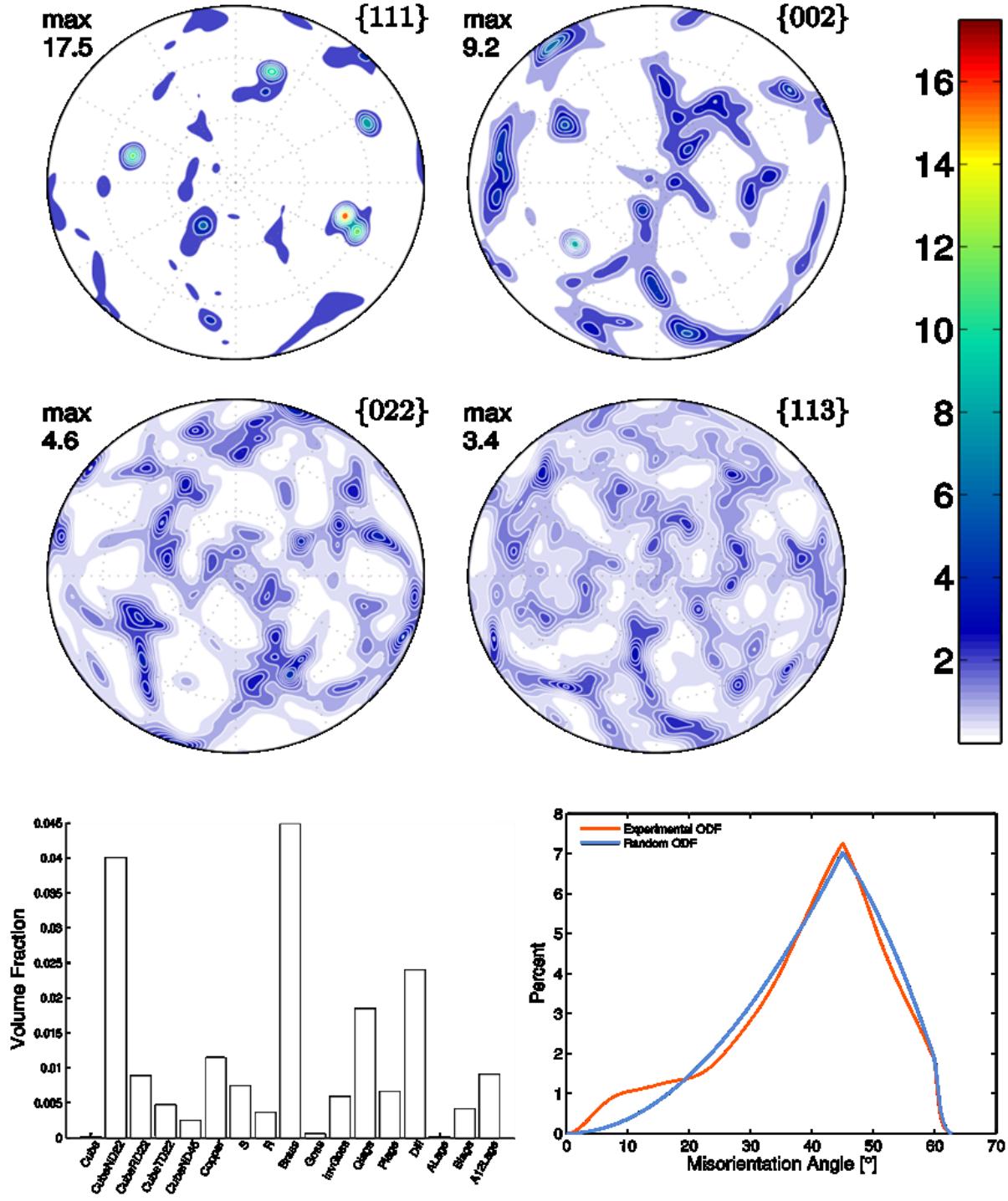

Figure 3.15: Texture analysis of Al-1Mg P9 sample after SRJT at 200°C, (a) pole figures, (b) volume fraction of various texture components, (c) misorientation distribution.

The combination of Figures 3.14 and 3.15 reveal the general macrotexture evolution of Al-1Mg P9 at elevated temperatures. For comparison, the exact volume fractions of each texture component and the fraction of low angle grain boundaries are summarized in Table 3.1. The

volume fraction of the conventional texture components, e.g. Cube, Goss, Copper, S and Brass, amounted to less than 7%, i.e. the texture in both samples was in general weak. The Cube and Goss texture are typical recrystallization respectively deformation texture components in Al alloys. The volume fraction of the Cube texture increased with increasing temperature, whereas the Goss component became weaker. The misorientation distribution map indicated that the volume fraction of LAGBs was higher than for a random misorientation distribution.

Table 3.1: The volume fraction of different texture components and fraction of low angle grain boundaries in Al-1Mg P9 deformed at different temperatures.

Volume fraction (%)	Cube	Goss	Copper	S	Brass	LAGB (relative frequency in %)
Al-1Mg P9 100°C	1.7	4.6	0.1	6.5	2.7	8.19
Al-1Mg P9 200°C	5.6	1.1	1.1	0.7	4.5	6.09

3.1.3.2 Al-5Mg

In the alloy with the highest solute content and high pre-deformation degree, i.e. Al-5Mg, P12, the kinetics of recovery and recrystallization were found to be slower than in Al-1Mg. It is evident from Figures 3.16 (a) and (c) that the microstructure evolution at both temperatures is essentially the same. The subgrain morphology and misorientation distribution maintained their initial as-deformed state, no noticeable recrystallization occurred under the investigated annealing conditions. Figures 3.16 (b) and (d) depict the grain size distributions (including cells, subgrains and grains) of Al-5Mg annealed at 100°C (c) and 200°C (d) after different annealing times as a function of CCDP pass number. The structural coarsening was not as obvious as in Al-1Mg, and recrystallization was strongly inhibited. In other words, the CCPDed microstructure in Al-5Mg is quite stable at 200°C within 30 minutes. As also

evident from Figure 3.16, no precipitation of intermetallic phases was detected during the various heat treatments.

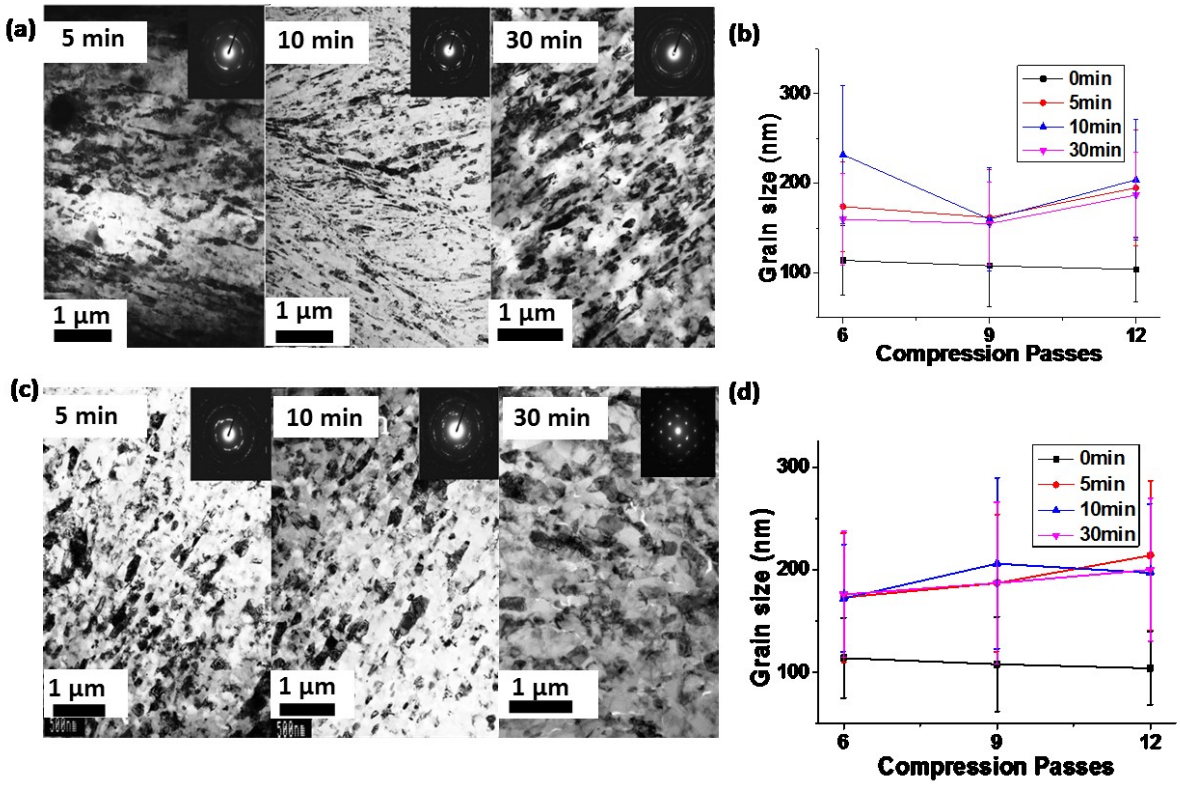

Figure 3.16: Microstructure evolution of Al-5Mg after 12 CCDP passes and annealing at (a) 100°C, (b) corresponding grain size distribution after static annealing at 100°C, (c) 200°C, (d) corresponding grain size distribution after static annealing at 200°C.

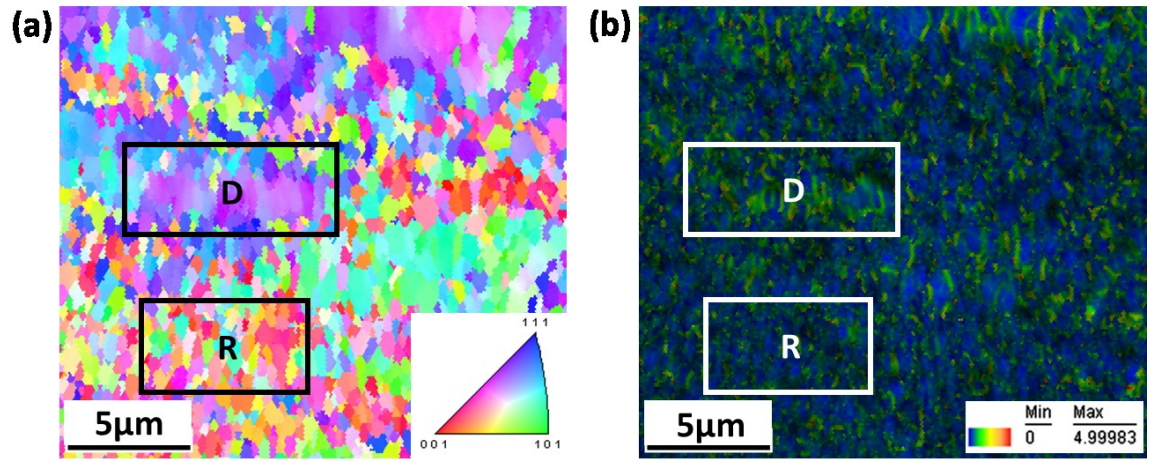

Figure 3.17: EBSD map of Al-5Mg P6 200°C, (a) IPF and (b) KAM.

Figure 3.17 reveals the orientation and internal strain distribution of Al-5Mg P6, after SRJT at 200°C. The average grain size was in the range of a few hundred nanometers, consistent with TEM observations. Compared to Al-1Mg, the reduced average recrystallized grain size of Al-5Mg suggests a pronounced drag effect of grain boundary motion caused by the high Mg content. These combined maps clearly distinguish the deformed and recrystallized areas: the area in frame R contains various grains displaying relatively wide color variations along <001>, corresponding to newly recrystallized locations with less internal strain, and the area in frame D contains grains of fairly similar color aligned along a preferential direction <111>, revealing the prior deformed structure. The internal strain index remains high in the deformed area and relatively low in the recrystallized regions. The average strain index is higher than in Al-1Mg.

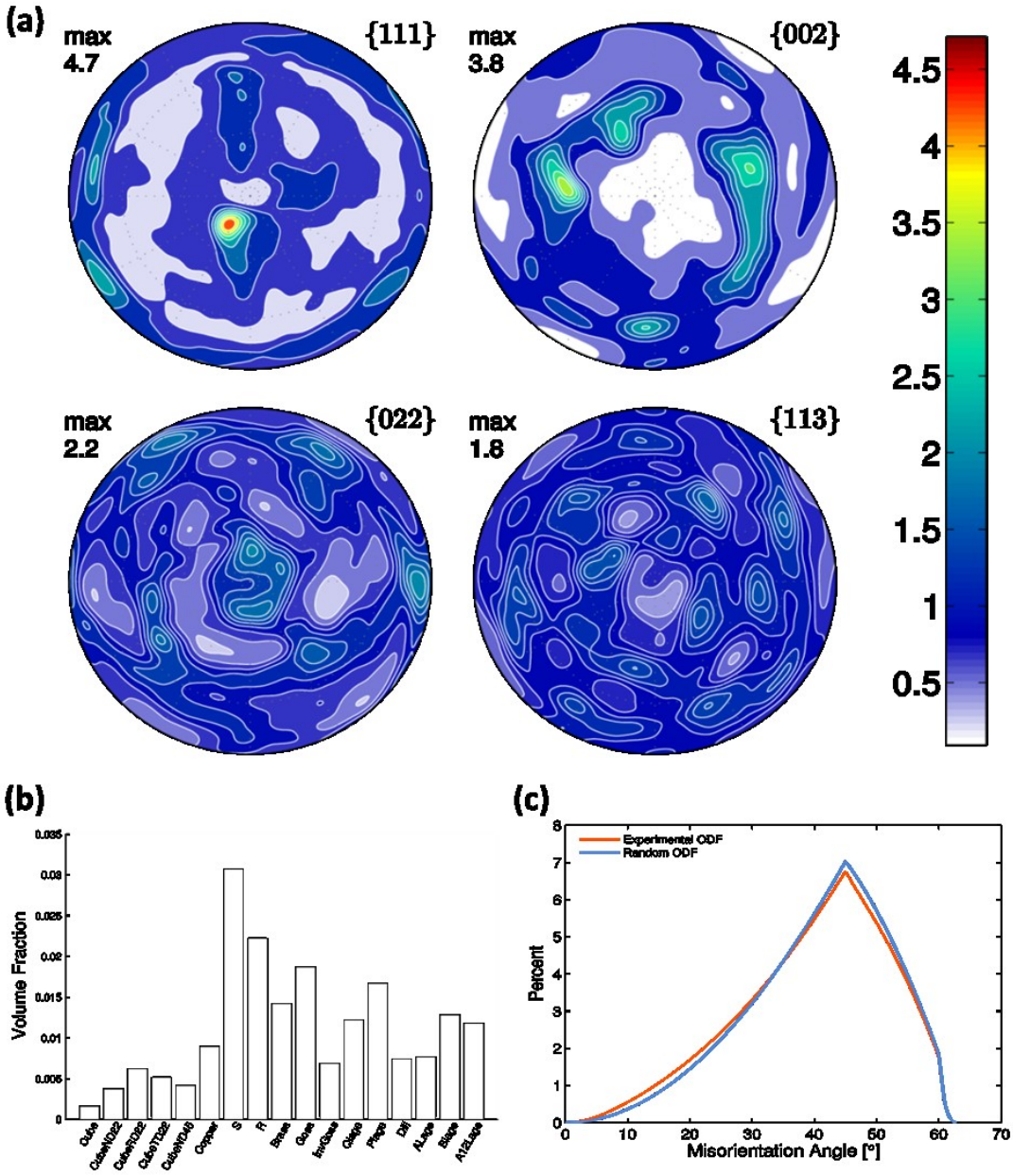

Figure 3.18: Texture analysis of an Al-5Mg P9 sample after SRJT at 100°C, (a) pole figures, (b) volume fraction of various texture components, and (c) misorientation distribution.

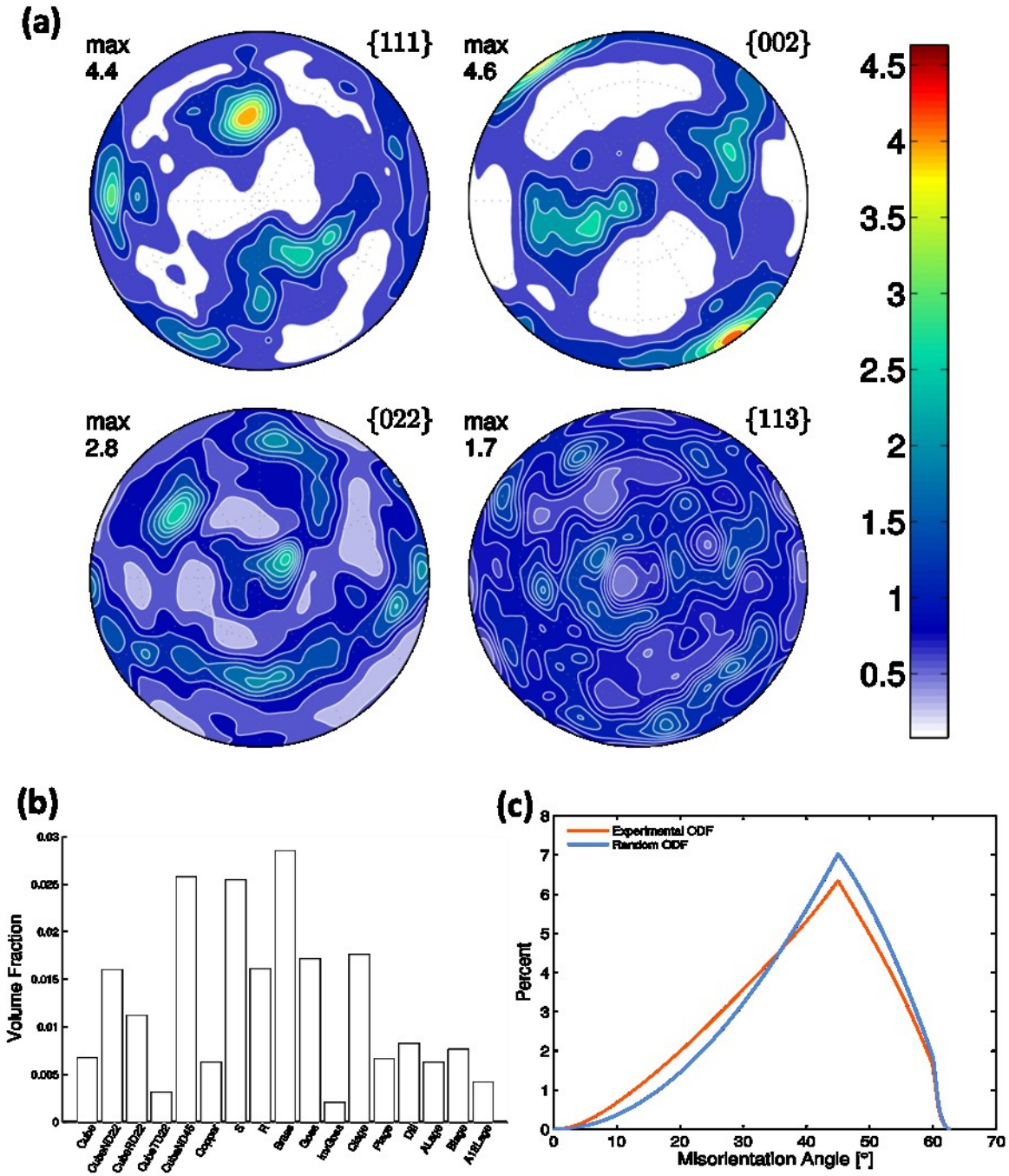

Figure 3.19: Texture analysis of an Al-5Mg P9 sample after SRJT at 200°C, (a) pole figures, (b) volume fraction of various texture components, and (c) misorientation distribution.

Table 3.2: Volume fraction of different texture components and fraction of low angle grain boundaries in sample Al-5Mg P9 deformed at different temperatures.

Volume fraction (%)	Cube	Goss	Copper	S	Brass	LAGB (relative frequency in %)
Al-5Mg P9 100°C	2.1	4.8	0.9	3.1	1.4	3.22
Al-5Mg P9 200°C	6.3	3.5	0.6	2.5	2.9	3.96

3.2 Mechanical properties

In the current study, Al-Mg alloys with Mg concentrations of 0.5%, 1%, 1.5%, 2%, 4% and 5% were investigated. For the sake of brevity, only results on Al-1Mg and Al-5Mg are presented here.

3.2.1 Mechanical tests at room temperature

3.2.1.1 SRJT of Al-1Mg

As described in Chapter 2, strain rate jump tests were conducted in two separate routes for different purposes. Double-SRJTs were performed to identify the material parameters, e.g. strain rate sensitivity and stress response at the jump point. The compression flow curves of of Al-1Mg double SRJT specimens are shown in Figure 3.20 for different number of CCDP passes.

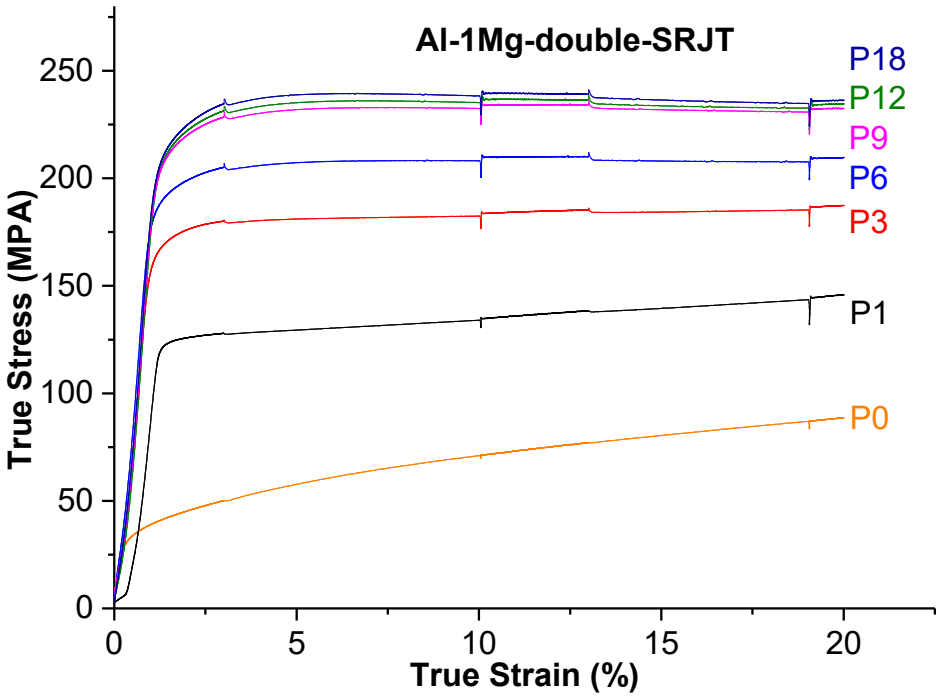

Figure 3.20: Compression flow curves of Al-1Mg alloy specimens subjected to double strain rate jump tests at room temperature.

Contrary to tensile testing, compression deformation is accompanied by geometric hardening rather than geometric softening, thus delayed the deformation instability. Therefore the flow stress kept rising with strain up to the end of the test. The stress response at each strain rate change point was meticulously investigated. The instantaneous stress change did not only reveal an increasing tendency with respect to a rising number of CCDP passes, but also exhibited an asymmetrical configuration with respect to the jump direction, i.e. $\Delta\sigma_{up} < \Delta\sigma_{down}$ (see Fig. 2.5 for definition). It further led to an asymmetry of the instantaneous strain rate sensitivity ($m_i = \Delta\sigma_i/\Delta ln\dot{\varepsilon}$), and the extent of this asymmetry tended to grow with progressing SPD, see Figure 3.21 (a). On the other hand, the steady state SRS values calculated as average from all jump points ($m_s = \Delta\sigma_s/\Delta ln\dot{\varepsilon}$) turned out to be negative. The value of m_s first decreased with number of passes and then bounced back after P6 (Figure 3.21 (b)).

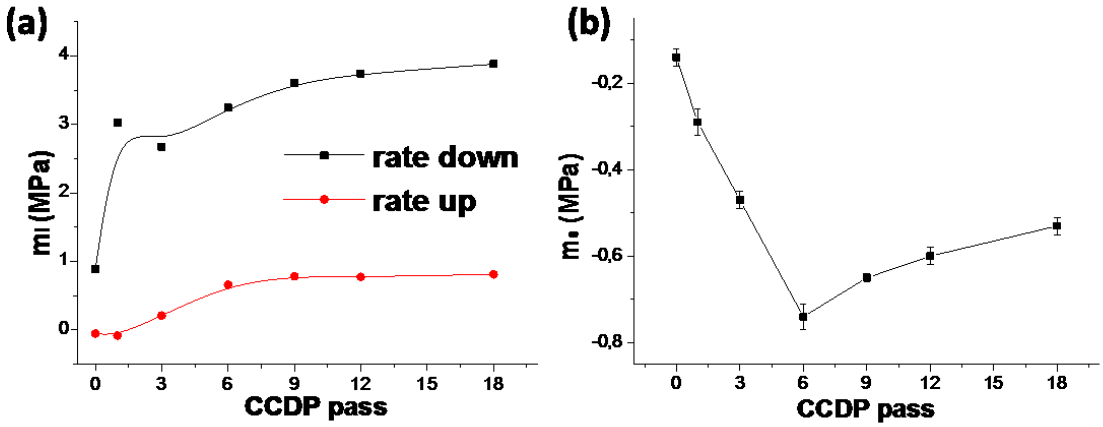

Figure 3.21: Evolution of averaged instantaneous SRS (a) and averaged steady state SRS (b) with respect to CCDP progress.

Multi strain rate jump tests were conducted to characterize the stress serrations and PLC types at corresponding deformation stages, as shown in Figure 3.22 and Table 3.3.

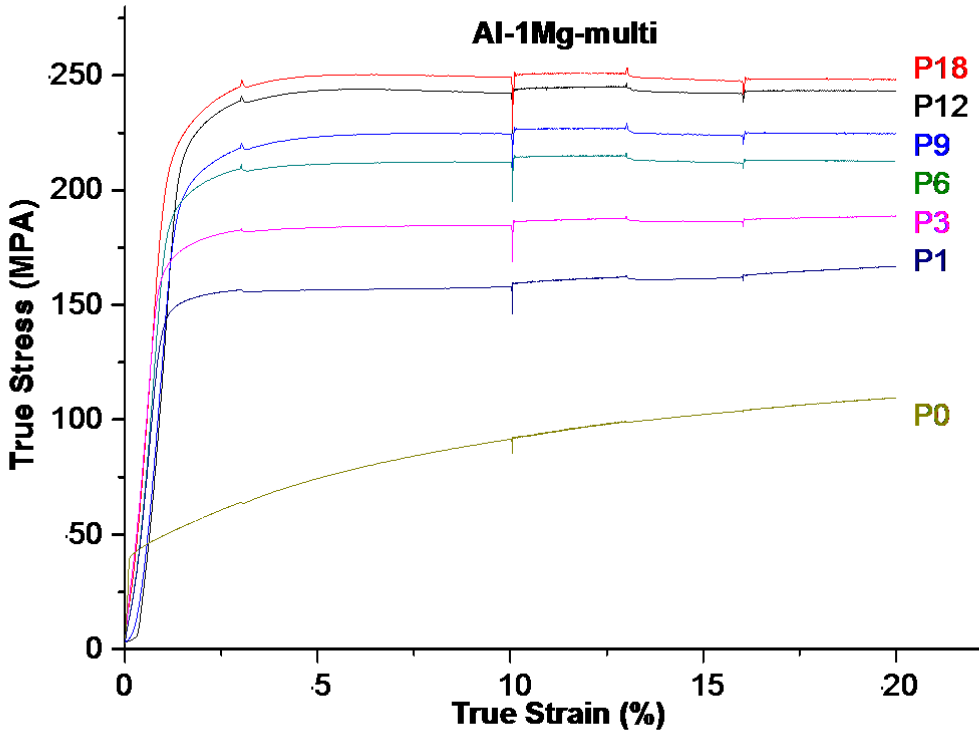

Figure 3.22: Flow curves of Al-1Mg alloy with multi strain rate jump tests at room temperature.

Table 3.3: PLC type and corresponding stress serrations of Al-1Mg.

$\dot{\varepsilon}/s$	Property	P0	P1	P3	P6	P9	P12	P18
5×10^{-5}	Serration (MPa)	0,4	0,4	0,25	0,3	0,25	0,25	0,2
	PLC type	B	B	B	B+C	B+C	B	B
1×10^{-4}	Serration (MPa)	0,2	0,1	0,15	0,2	0,25	0,2	0,15
	PLC type	B	B	B	B+C	B+C	B	B
5×10^{-4}	Serration (MPa)	0,1	0,35	0,25	0,3	0,25	0,15	0,1
	PLC type	A	B	A+B	A+B	A+B	A+B	A+B
1×10^{-3}	Serration (MPa)	0	0,03	0,05	0,1	0,2	0,15	0,1
	PLC type	No	No	A	A	A+B	A	A+B

3.2.1.2 Constant strain rate tensile tests of Al-1Mg

Tensile tests with constant strain rates were conducted at room temperature, in order to determine the characteristic mechanical properties of the materials, e.g. yield strength, ultimate tensile strength, etc. Moreover, the DSA related parameters such as critical strain, onset of the DSA effect, were determined for different strain rate conditions. For brevity only the tensile flow curves of Al-1Mg at a strain rate 10^{-4}/s with increasing number of CCDP passes are presented in Figure 3.23.

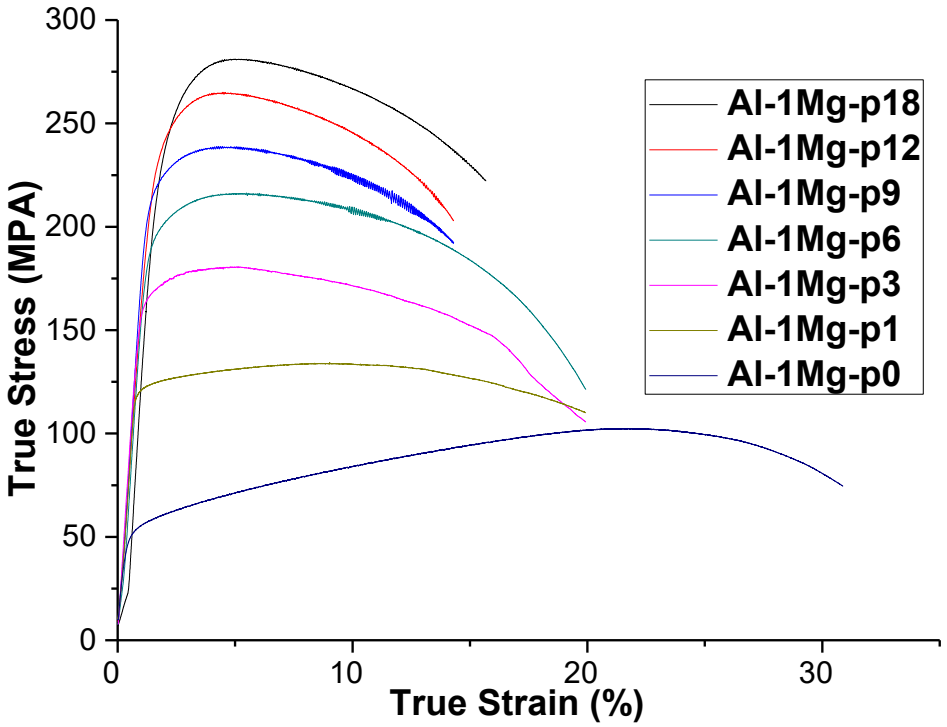

Figure 3.23: Tensile flow curves of Al-1Mg alloys at a strain rate of 10^{-4}/s.

With increasing number of CCDP passes, the yield stress and the ultimate tensile strength increased, whereas the uniform strain and the fracture strain showed an opposite trend. Evidently, SPD improved the strength of the alloy but concurrently degraded the ductility. The critical strain ε_c for the start of the PLC effect was affected by temperature, strain rate, CCDP passes etc. In order to assess the accuracy of ε_c the fluctuations introduced by the testing machine itself were examined by empty load tests. The onset of the PLC effect was associated with the first significant stress drop larger than 0.05MPa at a strain rate of 10^{-3} /s. In case of lower strain rates, i.e. 10^{-4} /s and 10^{-5} /s, the stress drop must only be larger than 0.01MPa. Values of important parameters are listed in Table 3.4.

Table 3.4: Mechanical properties of Al-1Mg alloys subjected to CCDP.

CCDP pass	$\sigma_y\ (MPa)$	UTS (MPa)	$\varepsilon_u(\%)$	Critical strain (%)

0	41,9	107,9	22,5	1,47
1	113,6	134,4	10,4	2,56
3	159,2	180,6	4,8	2,04
6	175,9	216,1	4,7	3,18
9	209,5	238,8	4,6	2,97
12	222,6	264,7	4,3	3,89
18	225,1	281,5	4,4	4,45

3.2.1.3 Constant strain rate tensile tests of Al-5Mg

The tensile flow curves at constant strain rate of Al-5Mg are shown in Figure 3.24. The ductility of Al-5Mg after SPD was quite limited, e.g. samples P9, P12, P15 fractured before yielding, and therefore, are not included in the figure.

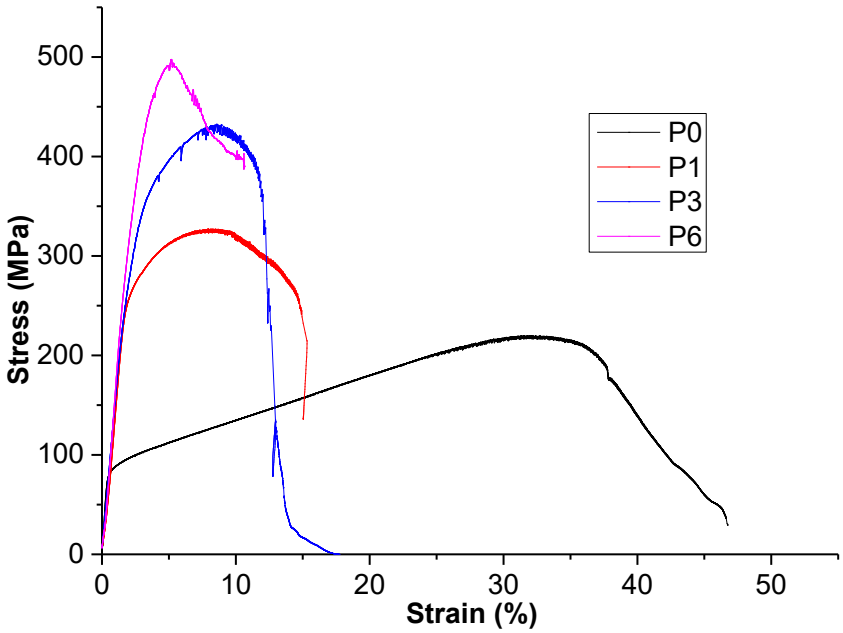

Figure 3.24: Tensile flow curves of Al-5Mg alloys, subjected to various CCDP passes, at a constant strain rate of 10^{-4}/s.

Table 3.5 summarizes all important mechanical properties obtained from Figure 3.24. The tensile strength of sample P6 was 468.4 MPa, which was six times larger than its undeformed counterpart and the highest tensile strength measured in the current work. These results revealed that with higher Mg content the increased strength and reduced ductility caused by SPD became more significant. The critical strain increased monotonically with increasing SPD up to six passes.

Table 3.5: Mechanical properties of Al-1Mg subjected to CCDP.

CCDP pass	$\sigma_y\ (MPa)$	UTS (MPa)	$\varepsilon_u(\%)$	Critical strain (%)
0	75,9	218,9	32,4	1,0
1	233,9	326,4	8,1	2,0
3	349,6	432,1	8,6	4,7
6	468,5	497,5	5,2	5,0

3.2.1.4 Flow curves with SRJT of Al-5Mg

The compression flow curves with double- and multi- strain rate jump tests of Al-5Mg are shown in Figures 3.25 (a) and (b), respectively. The slopes (work hardening rate) of Al-5Mg alloys were larger than of Al-1Mg.

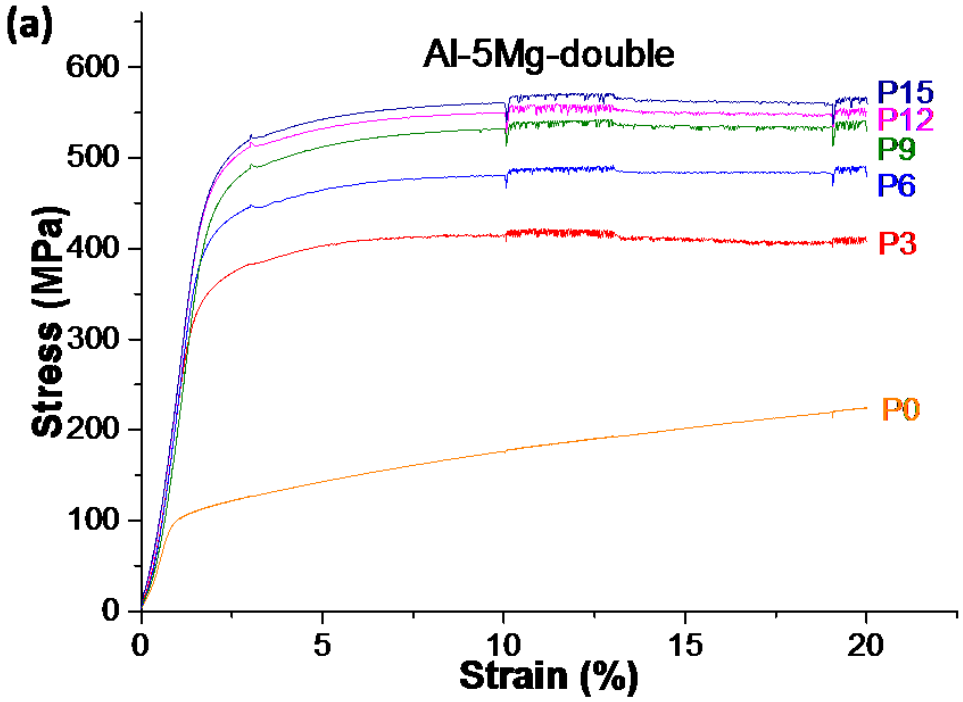

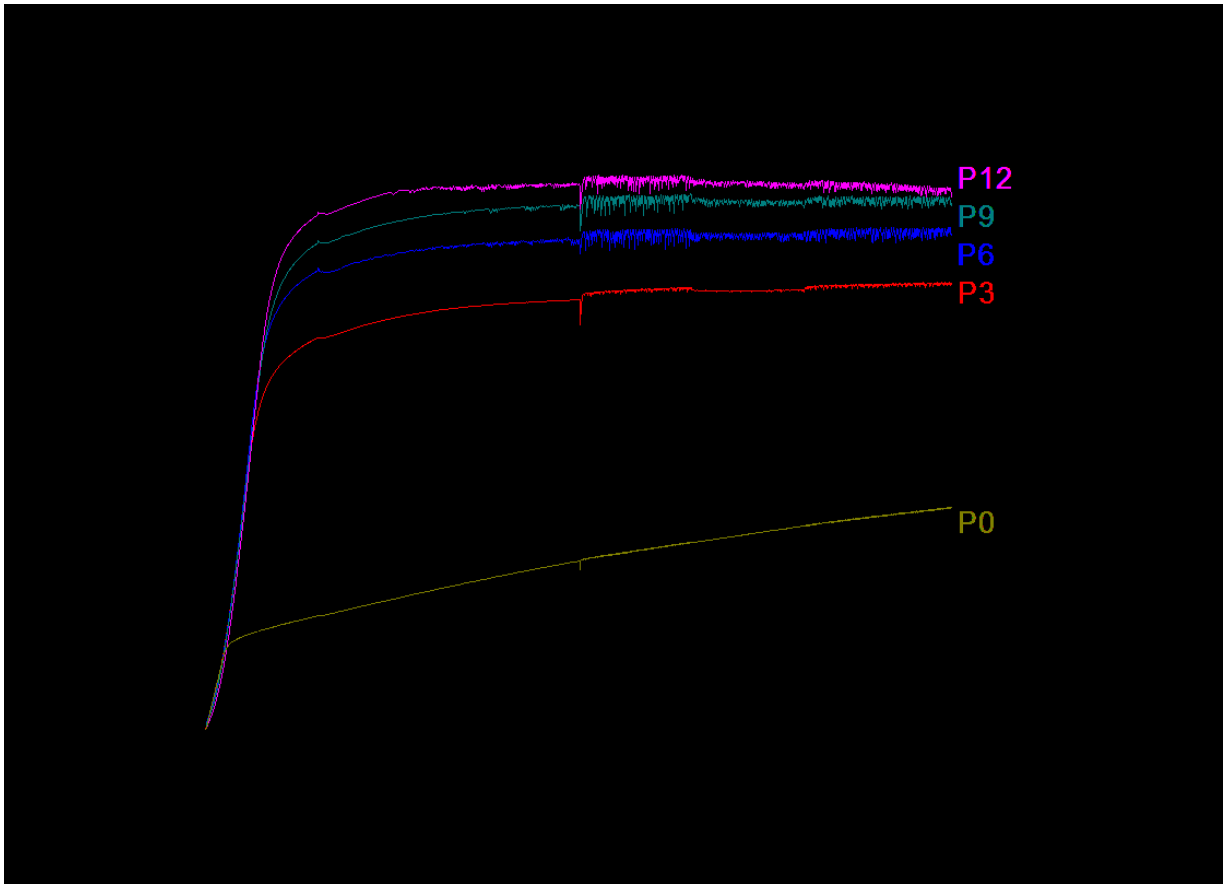

Figure 3.25: Compression Flow curves of Al-5Mg subjected to (a) double SRJTs and (b) multi SRJTs after various CCDP passes.

On each flow curve the serrations of the steady state flow stress were quite marked and their magnitude was higher than in Al-1Mg. Corresponding PLC types and stress serrations are summarized in Table 3.6.

Table 3.6: PLC type and corresponding stress serrations of Al-5Mg

$\dot{\varepsilon}/s$	Property	P0	P1	P3	P6	P9	P12
5×10^{-5}	Serration (MPa)	1	1,5	3	18	15	12,5
	PLC type	B	B+C	B+C	C	C	C
1×10^{-4}	Serration (MPa)	0,8	1,2	2,5	13	7	10
	PLC type	B	B	B+C	C	C	C
5×10^{-4}	Serration (MPa)	0,25	1	0,8	5	5	5
	PLC type	A+B	B+C	B	B	B+C	C
1×10^{-3}	Serration (MPa)	0	0,5	0,3	2,5	3	3
	PLC type	No	A	A	B	B	B

As indicated by Table 3.6, the stress serration amplitude showed a non-monotonic trend with increasing number of CCDP passes, i.e. they first rose and then decreased, contrary to the evolution of the steady state SRS. Generally, however, SPD amplified the magnitude of the DSA effect, resulting in an enlargement of the serration amplitude. On the other hand, the strain rate also influenced the DSA effect, i.e. a lower strain rate led to larger serrations. The PLC type tended to exhibit more regular serrations, e.g. type B and C, for alloys subjected to higher SPD strain.

3.2.2 Mechanical tests at elevated temperatures

3.2.2.1 Constant strain rate tests

Tensile tests at 100°C and 200°C were conducted at various constant strain rates, i.e. 10^{-3}/s,10^{-4}/s and 10^{-5}/s. Characteristic parameters such as yield stress, ultimate tensile strength and critical strain for PLC were derived from the flow curves. Due to the poor ductility of Al-5Mg, owing to tiny cracks inside the specimens after CCDP only results of Al-1Mg are shown in Figure 3.26.

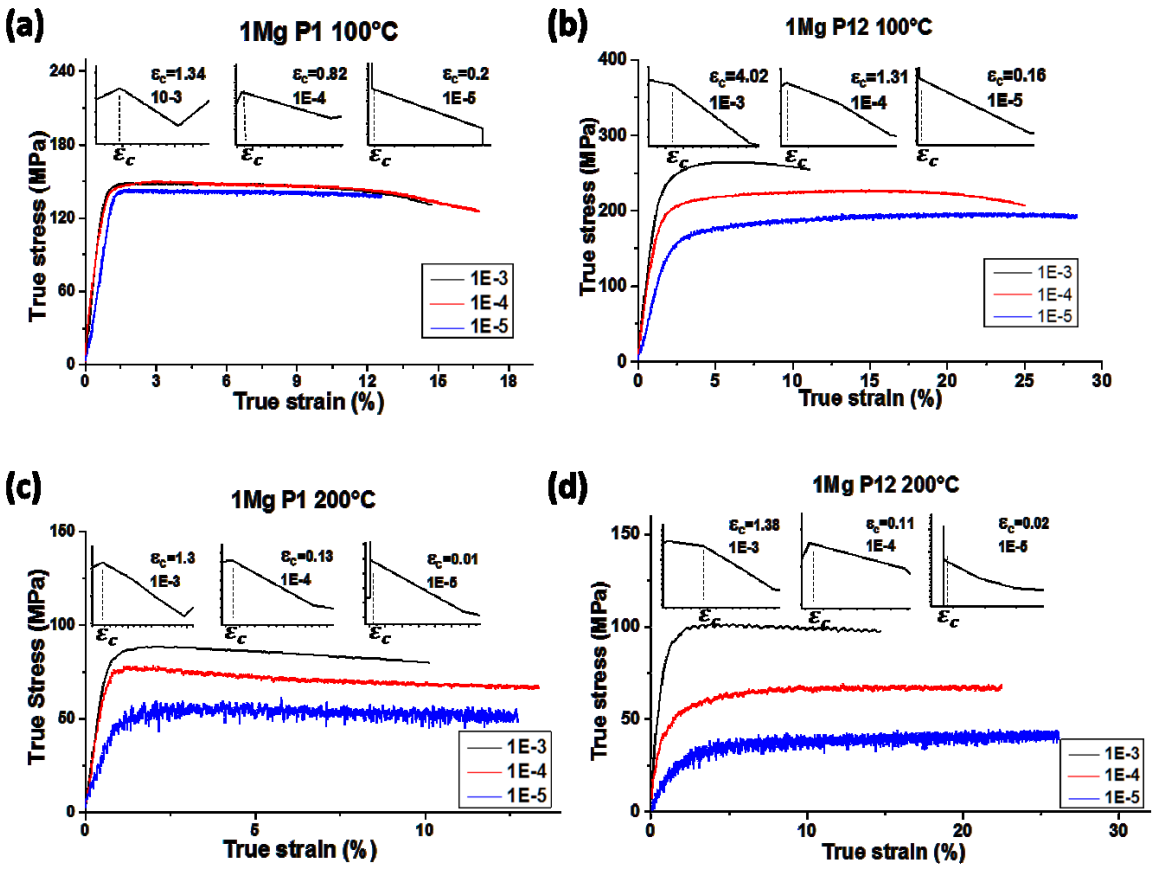

Figure 3.26: Stress-strain behavior of Al-1Mg during constant strain rate tensile tests for different temperatures (a) Al-1Mg P1 at 100°C, (b) Al-1Mg P12 at 100°C, (c) Al-1Mg P1 at 200°C, (d) Al-1Mg P12 at 200°C. The first serration (critical strain) for various strain rates is shown in the inserts for each curve.

The critical strain ε_c on each flow curve, i.e. the first stress drop indicating the onset of the PLC effect is also indicated in Fig. 3.26. With increasing temperature/decreasing strain rate, ε_c decreased, i.e. a higher deformation temperature facilitated the onset of the PLC effect. In case of very low strain rates, the stress drop would even arise at incipient plastic deformation Previous room temperature experimental results revealed that in most cases the critical strain ε_c increased with increasing CCDP pass number. This was also observed for deformation at 100°C. However, the influence of SPD was largely eliminated as the temperature increased up to 200°C. Furthermore, the critical strain was also related to the chemical composition, i.e. a higher Mg content led to a larger critical strain value.

The yield stress and steady state stress of Al-1Mg and Al-5Mg with progressing CCDP is presented in Figure 3.27. At 100°C, Al-1Mg subjected to higher CCDP strains exhibited higher yield stresses, whereas the high CCDP pass samples of Al-5Mg possessed a decreasing stress trend after P3. At 200°C the yield strength increased with increasing CCDP strain up to pass 3 where a peak value was reached. With further increase of the CCDP strain the yield strength subsequently decreased. This trend was qualitatively the same for both alloys but more pronounced for Al-5Mg. As expected, a decreasing yield stress was observed with increasing deformation temperature owing to thermal activation of the flow stress. However, the decrease of the yield stress with increasing pass number for the samples deformed at elevated temperatures was contrary to expectation, since an increasing prestrain would yield a higher dislocation density and therefore, a higher yield stress. Apparently, the decrease of the elevated temperature yield stress with increasing number of passes must be attributed to recovery and/or recrystallization processes taking place during heating of the samples to the testing temperature, as evident from the microstructures after static annealing (Figure 3.12). These softening processes, however, will be accompanied by a serious change of the microstructure established by predeformation via CCDP, which has to be taken into account for a correlation of microstructure – property relationships during and subsequent to deformation at elevated temperatures.

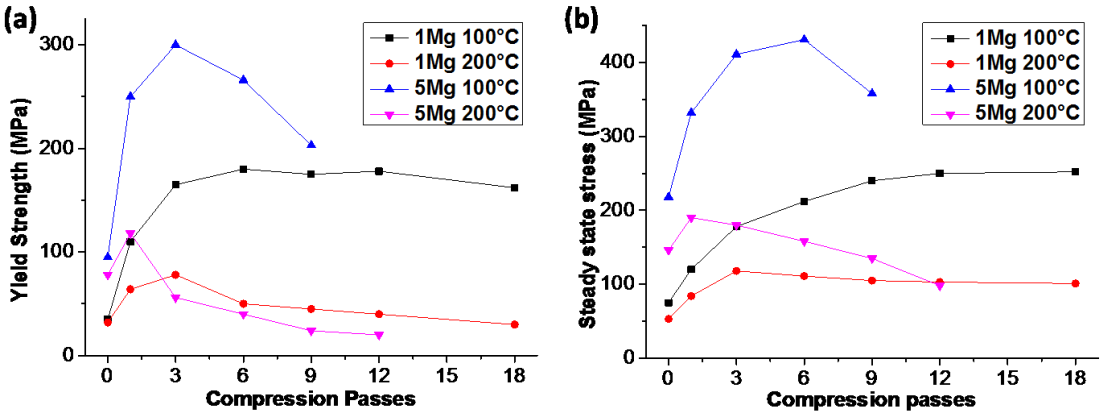

Figure 3. 27: Yield stress ($\sigma_{0.2}$) (a) and steady state flow stress (b) of all tested samples in dependence on CCDP pass.

3.2.2.2 SRJT and strain rate sensitivity

SRJTs conducted at elevated temperature were all performed during uniaxial tensile test. To simplify the analysis, only double mode SRJTs were applied, i.e. the strain rate alternated between 10^{-4}/s and 10^{-3}/s. Since each sample required a certain time period to reach the target temperature, the heating and soaking effect had to be taken into consideration for the annealing schedule.

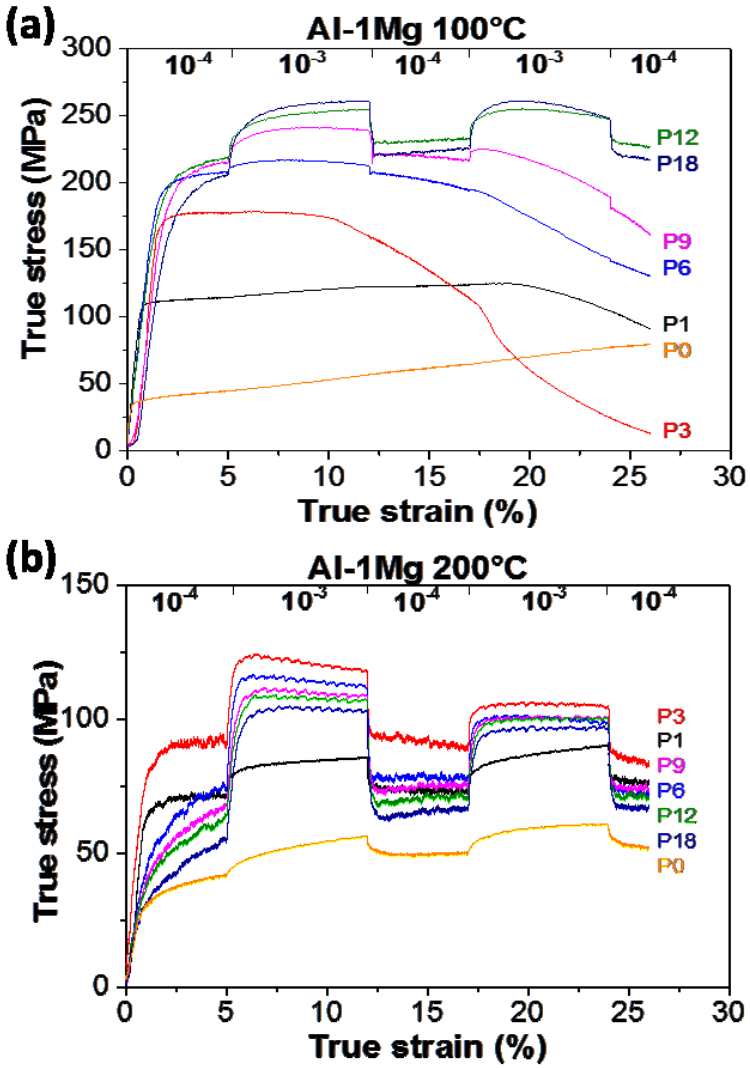

Figure 3.28: Stress-strain behavior of Al-Mg alloys during strain rate jump tests with increasing CCDP pass number. (a) Al-1Mg at 100°C. (b) Al-1Mg at 200°C.

Figure 3.28 gives the true stress - true strain curves with double strain rate jump tests at strain rates alternating between 10^{-4}/s and 10^{-3}/s for Al-1Mg at different temperatures. As expected, the strength of the as-CCDPed alloys decreased with increasing temperature. Compared with the room temperature behavior, at elevated temperatures the strength did not increase monotonically with the progressing CCDP. In case of Al-1Mg, at 100°C the yield strength first increased with rising number of CCDP passes but then levelled off. At even higher temperatures (200°C) the yield strength started to decrease after reaching a peak value at P3. As a benefit of reduced strength the ductility of all as-CCDPed alloys was improved. Noticeable softening with increasing strain was observed at the lower temperature, e.g. Al-1Mg P3, P6, P9 at 100°C. This softening behavior became less obvious as the temperature

increased. At 200°C such softening behavior had almost disappeared. At the strain rate change points, the asymmetrical instantaneous stress response with respect to the strain rate jump direction found at room temperature SRJT, was no longer observed at elevated temperature tests.

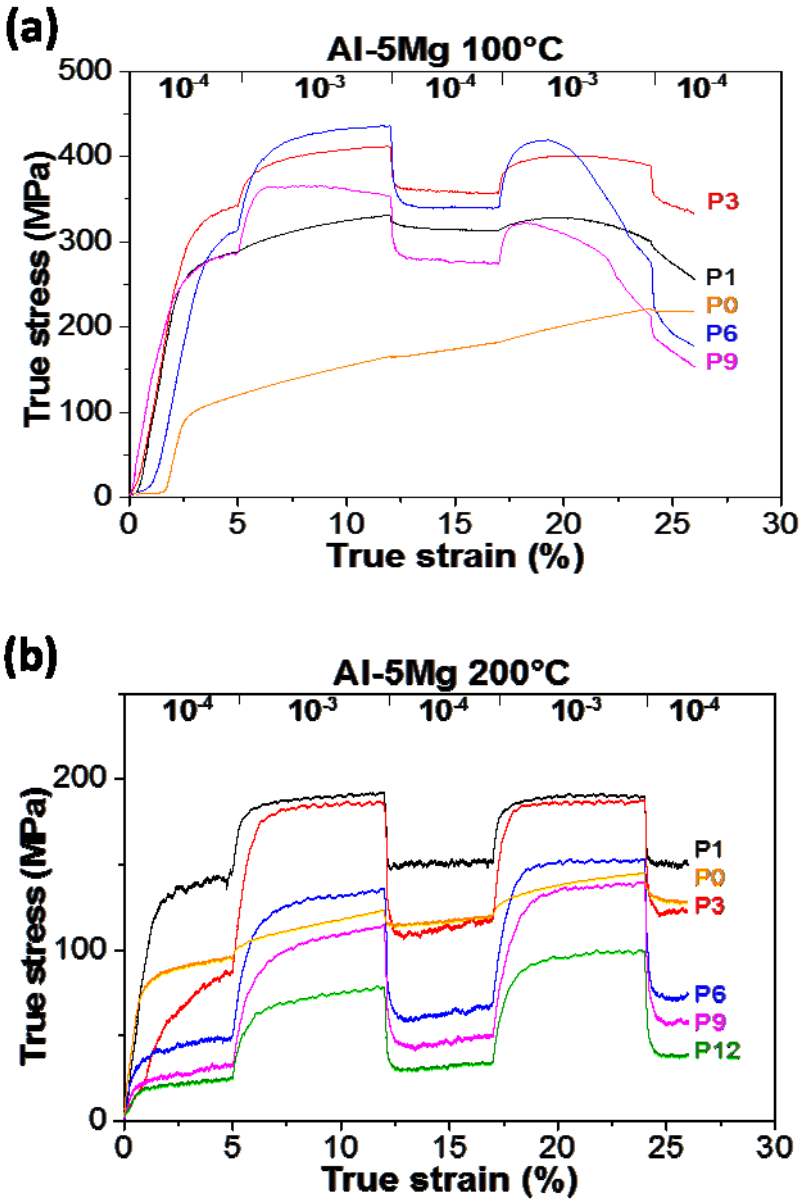

Figure 3.29: Stress-strain behavior of Al-Mg alloys with strain rate jump tests for increasing CCDP pass number. (a) Al-5Mg at 100°C. (b) Al-5Mg at 200°C.

The flow curves with SRJT for Al-5Mg at different temperatures are given in Figure 3.29. Compared with the low Mg content alloys, the softening of highly deformed sample was more pronounced, e.g. the strength reached a maximun for P6 at 100°C, and P1 at 200°C, and then decreased with increased CCDP pass number. The strain softening observed in Al-1Mg at 100°C was also found in Al-5Mg, P6 and P9, which disappeared, though, as the temperature was raised to 200°C. The instantaneous stress response at the strain rate change points were more pronounced than for Al-1Mg.

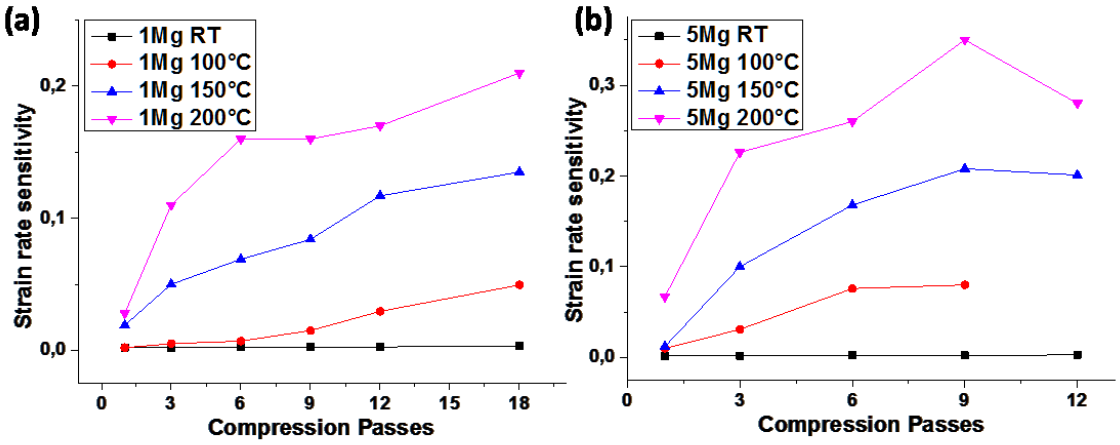

Figure 3.30: Strain rate sensitivity of as-CCDP Al-1Mg (a) and Al-5Mg (b) at different temperatures.

Figure 3.30 illustrates the dependency of the instantaneous SRS in Al-Mg alloys on the number of CCDP passes at different temperatures. The SRS values at room temperature were of the order of 10^{-3}; with increasing temperature and SPD strain they grew up to 10^{-1}. Increasing SPD and/or higher temperatures enlarged the instantaneous SRS.

4. Discussion

4.1 Properties at ambient temperature

4.1.1 Analysis of the deformed microstructure

4.1.1.1 Typical microstructure after CCDP

Instead of a homogeneous distribution of dislocations, cellular dislocation arrangements are typically found in pure metals, e.g. copper or alpha-iron and their alloys, when deformed plastically [Kuhlmann 1982, Ungar 1984]. In the current work a cell structure was also observed in Al-Mg alloys subjected to low (1-3) CCDP passes. The equivalent strain for one CCDP pass in the center of the sample was about 70%.

The microstructure became refined by intersection of intensive shear bands generated during each pass of CCDP, which generates the well-known inhomogeneous X-shape strain distribution of compressed samples. More precisely, larger equi-axed grains underwent elongation along the shear direction. In the course of repeated specimen rotation and compression, the subgrains encompassed by LAGBs within the central elongated grains were rotated and transformed into finer grains enclosed by high angle grain boundaries (HAGBs). Outside of the central region grain refinement was not so effective.

The micrograph in Figure 4.1 (a) reveals the microstructure of an Al-5Mg sample subjected to 9 passes of CCDP. The region enclosed by the white solid line gives evidence of the shear deformation with the shear direction about 45° inclined to the normal direction (ND) and extension direction (RD), see Figure 1.6. The microstructure in the triangular region is

distinctly elongated and finer compared to the area outside, indicating grain refinement by shear deformation. It is also noted that equi-axed grains were formed after subsequent shear deformation along 3 dimensions, which was caused by the rotation of the samples after each CCDP pass. Figure 4.1 (b) illustrates the microstructure in vicinity of a boundary between shear band and cell structure, marked by a solid white line. The larger cell structure became elongated along the shear direction, the subgrains within the elongated grains were rotated and transformed the cell walls into LAGBs. The grain refinement lead finally to a mechanically stable configuration with high dislocation density. No obvious deformation twinning was observed due to the relatively high stacking fault energy (SFE) of Al-Mg alloys. Moreover, no precipitation was detected in the UFG alloys even in Al-5Mg, which suggests that strain induced precipitation did not occur during the CCDP process. Therefore, the Al-Mg alloys in the present work remained all in a solid solution state.

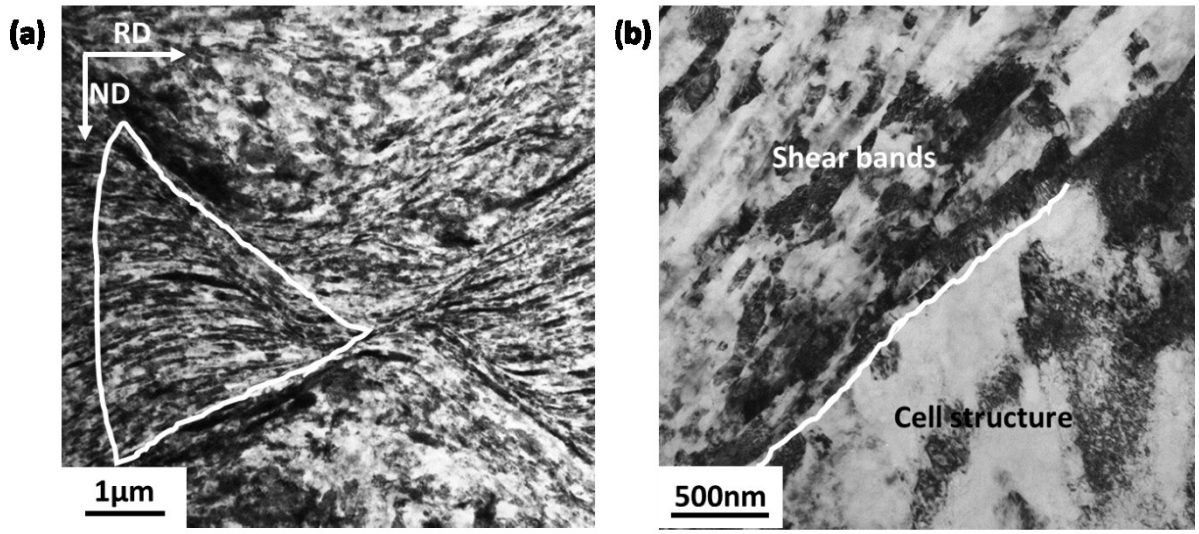

Figure 4.1: Evidence of shear deformation in Al-5Mg P9 (a), boundary between shear band and cell structure in Al-4Mg P9 (b).

With increasing imposed strain, the cell structure evolved into a microstructure consisting mainly of subgrains/grains, as evident from Figure 3.7 (f). Some grain boundaries were visible and appeared to be mostly curved, wavy or corrugated. There were also some poorly defined grain boundaries. The contrast within the grains was not uniform but often changed in a complex way, indicating high internal stresses.

4.1.1.2 Grain refinement by CCDP

Figure 4.2 depicts the influence of CCDP on grain refinement in Al-Mg alloys with different Mg content. The grain size decreased precipitously up to 6 passes, thereafter the rate of refinement levelled off.

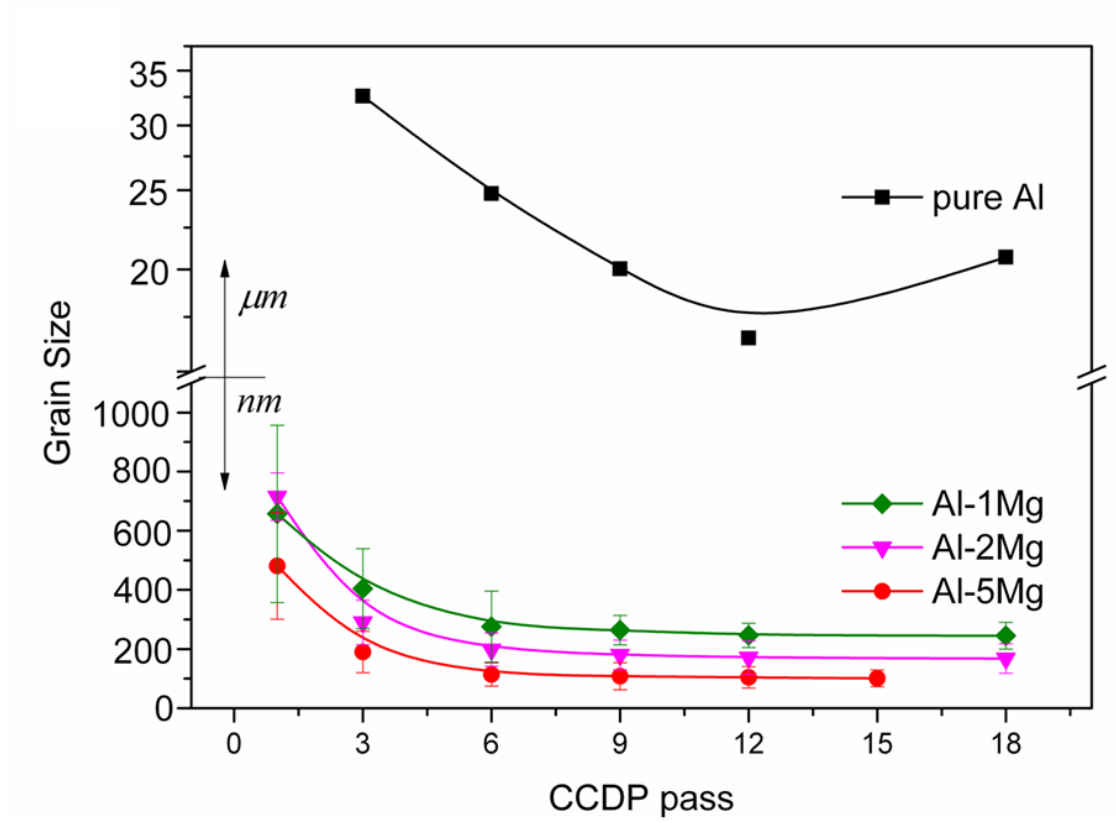

Figure 4.2: Grain size evolution of Al-1Mg, Al-2Mg, Al-5Mg and pure Al subjected to CCDP.

In materials with high stacking fault energy (SFE) such as Al and its alloys, dislocations tend to arrange themselves in a minimum energy configuration, i.e. dislocation cells with small misorientation. The mechanism behind grain refinement by severe plastic deformation is the fragmentation of originally coarse grains owing to dislocation cell formation. These cells subsequently evolve into subgrains with increased misorientation upon further imposed strain. Finally, the misorientation increases due to an increasing amount of dislocations absorbed in the sub boundaries, and eventually HAGBs are formed. TEM observations have revealed that the microstructure of UFG Al-Mg alloys fabricated by CCDP is a mixture of dislocation cells, subgrains and grains. With increasing plastic strain and thus, dislocation density, the cell/grain

size decreased. However, SPD cannot continue refining the microstructure once the grain size has reached a critical minimum value. The flow stress τ is related to the cell/subgrain size d by [Gottstein 2004]

$$d = \frac{KGb}{\tau} \qquad (4.1)$$

where G is the shear modulus, b the Burgers vector, and K is a constant of about 10 for metallic materials, τ is the applied shear stress. The imposed shear stress cannot be infinitely large but has a maximum value, τ_{max}. τ_{max} is typically estimated as G/35 for Al. According to Eq.4.1, $d_{min} = 350b \cong 100\,nm$. This value is consistent with the measured minimum grain size (~100nm) for Al-5Mg in our investigation.

Besides the strain also the Mg concentration has obviously impact on the grain refinement. In comparison to Al-1Mg, where the grain size decreases from several hundred micrometers in the non-deformed state to about 250 nm after 12 passes CCDP, the grain size of Al-5Mg is reduced to about 100 nm after a similar amount of deformation.

4.1.1.3 Influence of Mg content

Figure 4.3 (a) illustrates the typical cellular dislocation structure of Al-0.5Mg with high dislocation density in the cell walls and low dislocation density in the cell interior. Most of the wall dislocations are immobile with various junctions, which drag dislocation motion and enforce dislocation bow-out. To maintain the imposed strain rate new dislocations have to be produced, predominantly by Frank-Read sources. Concurrent recovery (Figure 4.3 (b)) happens via annihilation of anti-parallel dislocations and non-conservative motion by climb of edge dislocations. Although climb is a thermally activated process which typically occurs to a relevant extent only at high homologous temperatures, i.e. above half the melting temperature, it may also occur during lower temperature deformation when abundant vacancies are produced by SPD. The observation of subgrain boundaries and triple junctions can be regarded as proof of recovery (Fig. 4.3).

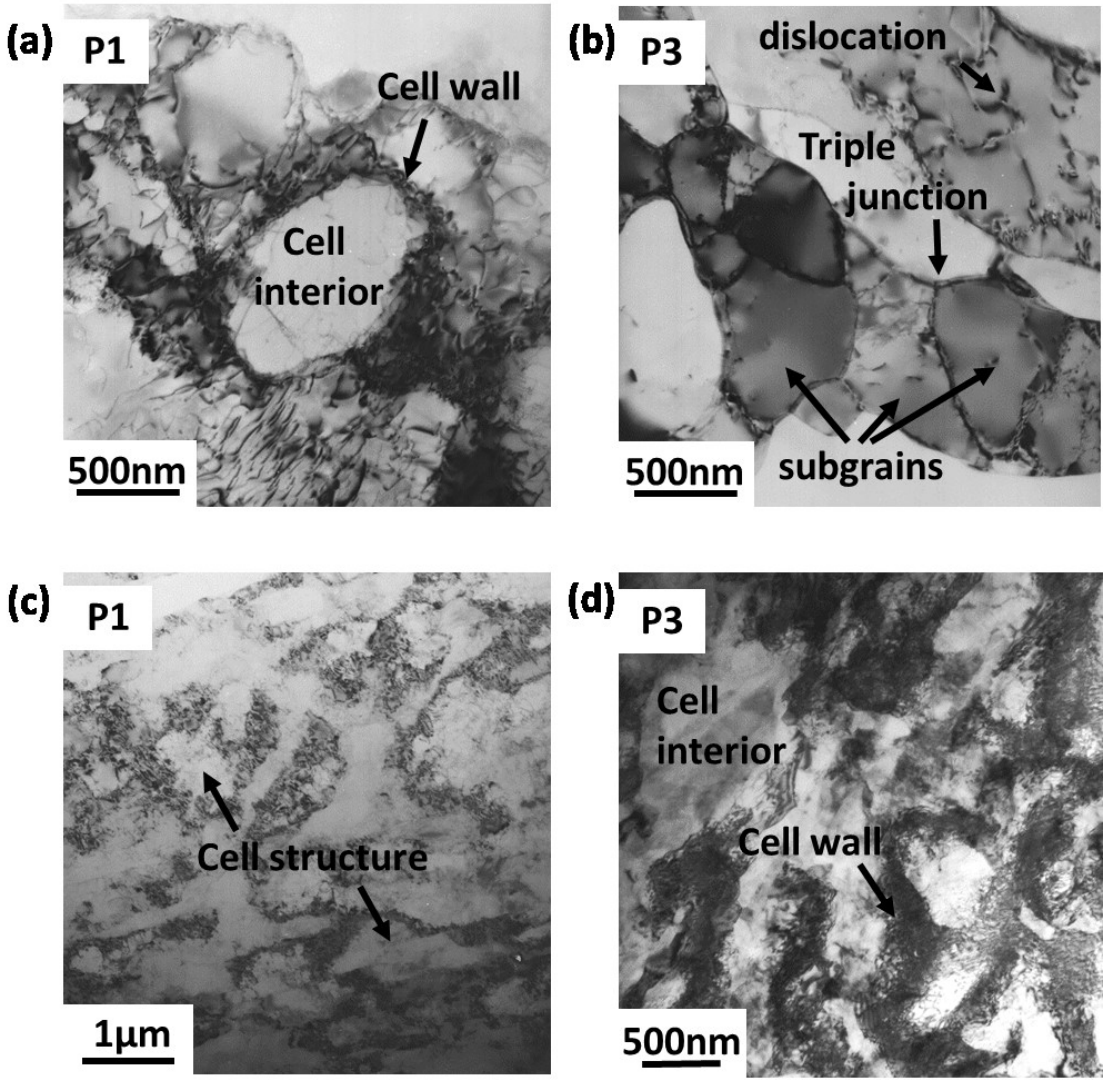

Figure 4.3: Typical cell structure of Al-0.5Mg after 1 pass (a), formation of subgrains led by recovery, P3 (b); Dislocation cell structure in Al-2Mg P1 (c) and Al-2Mg P3 (d).

With increasing Mg concentration the microstructure tends to develop more slowly. Recovery is much less pronounced since segregation of Mg atoms to the dislocations promotes their dissociation, which makes cross slip more difficult and therefore enforces planar slip, which lowers the possibility of dislocation annihilation. On the other hand, the segregated solute atoms exert a drag on dislocation motion and therefore, make deformation more difficult which makes itself felt by a higher flow stress compared to alloys with lower Mg content. Consequently, compared with Al-0.5Mg, where the cell structure has disappeared after P3, the cell structure in Al-1.5Mg (Figure 4.3 (d)) is retained up to a larger strain, i.e. more than 3 passes. Figure 4.3 substantiates that the dislocation density increases with growing Mg

content, as the thickness of the cell walls (dark regions) becomes larger with increasing Mg content.

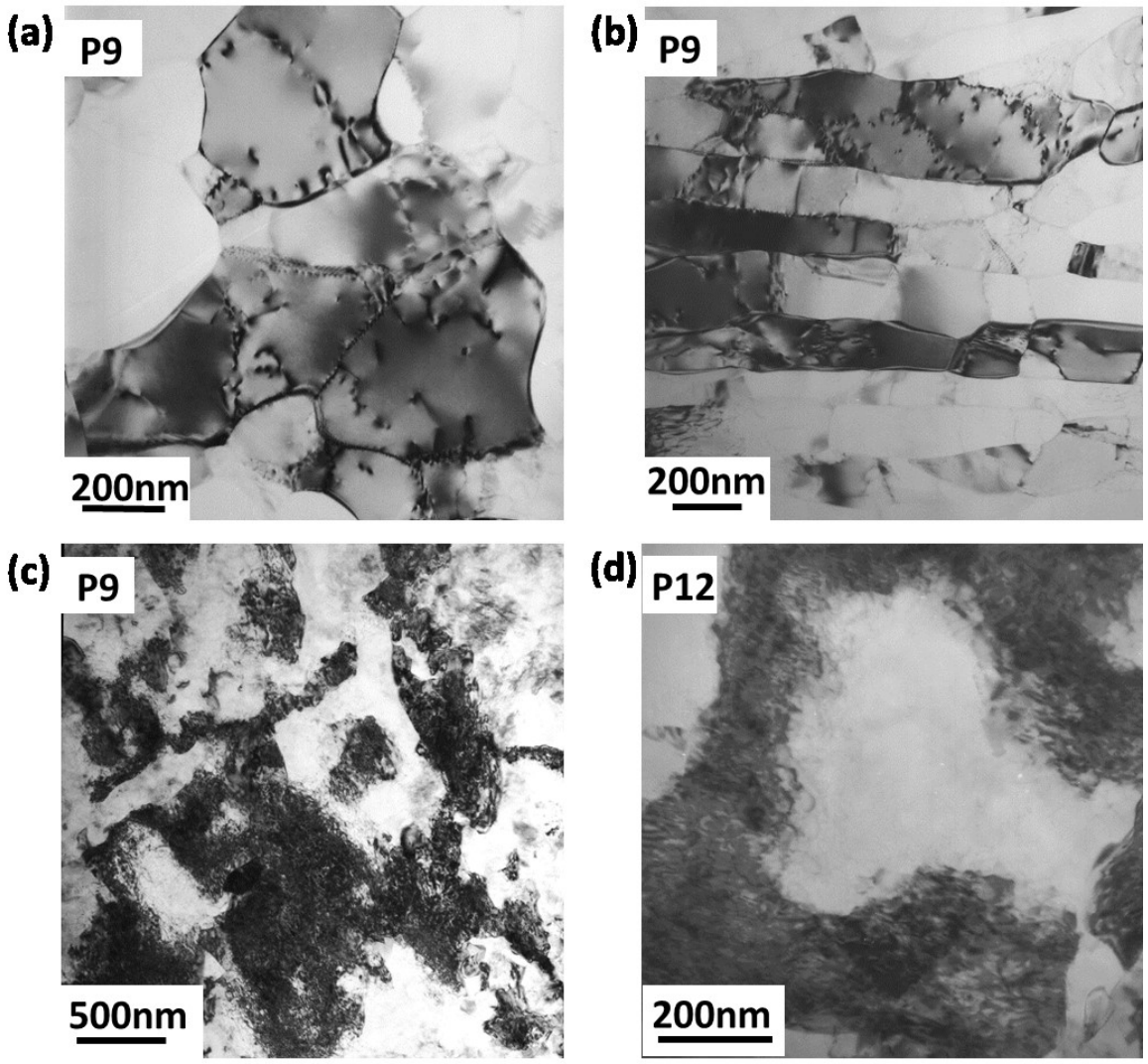

Figure 4.4: Microstructure of UFG Al-Mg alloys. (a), (b) Al-1Mg after 9 passes. (c) Al-5Mg after 9 passes, and (d) 12 passes.

With further increasing Mg content, the development of a stable microstructure is delayed to larger strains. Figure 4.4 (a) and (b) reveal that the microstructure of Al-1Mg P9 is mainly composed of subgrains and grains, indicating strong dynamic recovery. However, the microstructure of Al-5Mg after high number of passes (Figure 4.4 (c) and (d)) still contains dislocation cells with substantial wall thickness, indicative of retarded dynamic recovery. This

observation confirms the results of Gubizca et al. [Gubizca 2004] and Morris et al. [Morris 2002], on as-ECAPed Al-Mg alloys.

The recovery/recrystallization processes are controlled by thermally activated processes, which make the retardation effect of Mg atoms more apparent at elevated temperatures. As recrystallization (RX) and recovery (RV) both share the same driving force, i.e. the stored elastic energy of the dislocations, they compete with each other. RX may be suppressed by recovery, since recovery progresses initially fast as it does not need an incubation time. RX normally occurs when the deformation temperature is high enough, i.e. typically above a homologous temperature of 0.4. A comparison of KAM maps of two alloys demonstrates clearly that the internal strain retained in an Al-1Mg is lower than in Al-5Mg, indicating that recovery is more pronounced in the low Mg content alloy. Recrystallization can occur in both alloys since the necessary driving force is more than sufficient, however, only in Al-1Mg large recrystallized grains were observed in the TEM. The IPF of Al-5Mg P6 indicates the existence of some small recrystallized grains, which refrain from further coarsening, apparently due to the drag effect of Mg atoms on dislocation and grain boundary motion. In essence, the alloy with higher Mg content possesses better microstructural stability during annealing.

4.1.2 Mechanical properties

4.1.2.1 Yield stress

The yield stress of polycrystalline homogeneous alloys is comprised of three components, solid solution hardening, grain size strengthening and dislocation hardening (strain hardening). From the dependency of the yield stress ($\sigma_{0.2}$) at room temperature on the CCDP pass number (Fig. 4.5 (a)) it is obvious that $\sigma_{0.2}$ increased monotonically with rising pass number and Mg content. According to the theory of Labusch [Labusch 1970], the yield stress rises with solute concentration c_0

$$\Delta\sigma_{ss} = MAc_0^{2/3} \qquad (4.2)$$

where $\Delta\sigma_{ss}$ is the increase of yield stress due to solid solution strengthening, M is the Taylor factor, and A is a material constant with A≈20.5 for Mg in Al [Dixit 2008], M=3.06 for tensile deformation of randomly textured polycrystals [Gottstein 2004]. For the highest Mg content in this study, the maximum solid solution strengthening contribution was about 70 MPa.

The major strength contribution of the CCDP deformed material can be attributed to dislocation hardening or grain size strengthening, since the microstructure after CCDP is characterized by a cellular dislocation arrangement. The yield strength increase $\Delta\sigma_{gs}$ (replace in equation) due to grain size strengthening is expressed by the Hall-Petch relation

$$\Delta\sigma_{gs} = \sigma_0 + \frac{K}{\sqrt{d}} \qquad (4.3)$$

where $\sigma_0$is the yield stress of the corresponding single crystal, d is the grain size (replace in equation, because of Fig. 4.5b). Figure 4.5 (b) confirms this dependency for the investigated material and substantiates that grain size strengthening is the main contribution to the flow stress of the UFG material in this study.

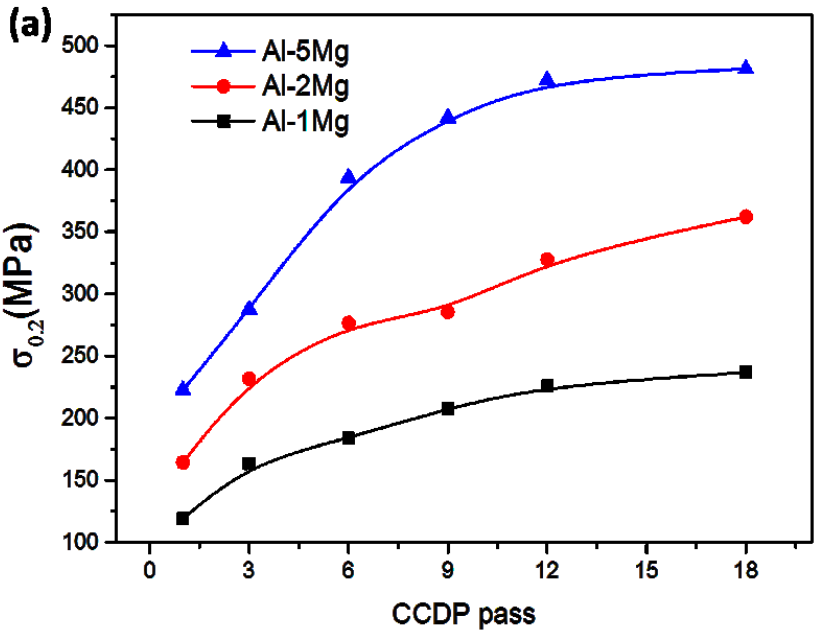

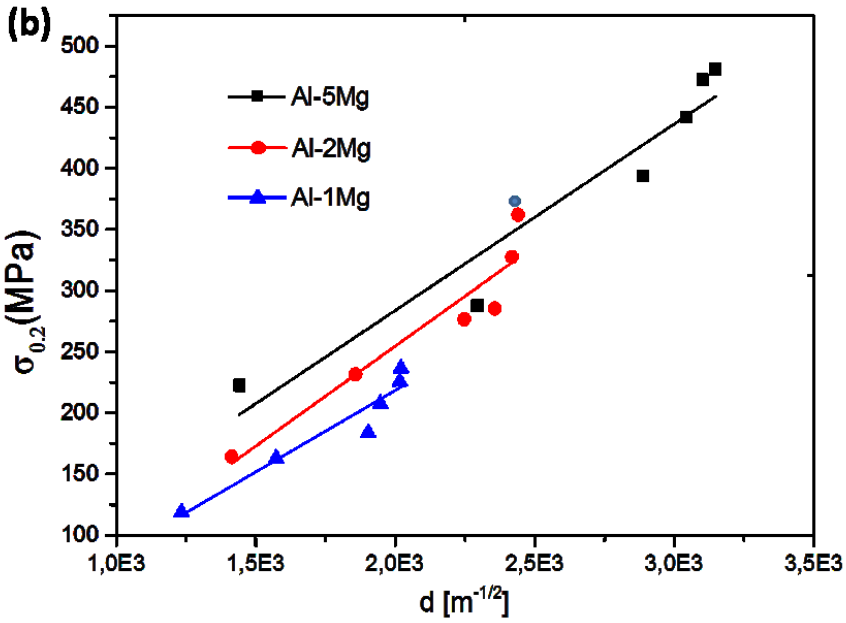

Figure 4.5: Dependency of yield stress on CCDP pass number and Mg concentration (a) and on grain size (b).

4.1.2.2 Strain rate sensitivity

For metallic materials exhibiting a PLC effect, the strain rate sensitivity has always been treated as important parameter, since it reveals essential information on the underlying deformation mechanisms. In this section, the behavior of the SRS will be presented for Al-5Mg, because of its most pronounced DSA effect. The other alloys with less Mg contents manifested weaker but similar features.

An description of the asymptotic steady state SRS was introduced by Hähner [Hähner 1997], who subdivided the total SRS (m_s) into two terms,

$$m_s = m_i + m_{DSA} \qquad (4.4)$$

in which m_{DSA} is the sensitivity component attributed to the DSA effect, whereas m_i denotes the instantaneous strain rate sensitivity (see Fig. 2.5). It's obvious from Eq. (4.4) that the value of m_s is determined by the superposition of m_i and m_{DSA}, particularly on the sign of both terms. Since m_i is always positive in current study, m_s will turn negative only if a

negative term m_{DSA} outweighs m_i, indicating the occurrence of serrated flow. Furthermore, the more negative m_s, usually the larger the amplitude of the flow stress serration.

By substituting the experimentally measured m_i and m_s into Eq. (4.4), the dependency of m_{DSA} on progressing SPD can be derived (Figure 4.6).

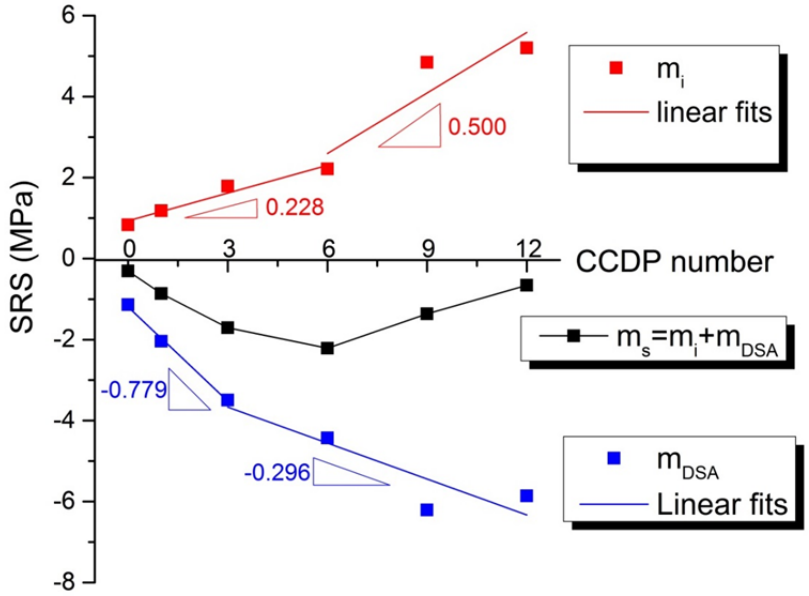

Figure 4.6: Dependence of SRS in terms of m_s, m_i *and* m_{DSA} CCDP pass number for Al-5Mg.

It is apparent that the trends of m_i and m_{DSA} are different. On the one hand, a monotonic increase of m_i is observed with increasing SPD degree, which is consistent with previous studies [Wei 2004, Wei 2007, Wei 2011]. It is attributed to the significant grain refinement down to the submicron/nanometer scale which dramatically enhances the rate dependence of plastic deformation in fcc metals. On the other hand, m_{DSA} becomes increasingly negative with increasing number of CCDP passes, indicating a growing aging effect with progressing CCDP.

However, although m_{DSA} is affected by SPD as well, it follows a distinct evolution law as does m_i. The instantaneous SRS, m_i, increases only slowly during the first 6 passes and accelerates afterwards. By contrast, m_{DSA} decreases rapidly within the first 3 passes but

afterwards the rate slows down. The difference can be attributed to the microstructure evolution during CCDP which imparts a different impact on m_i and m_{DSA}, respectively. At the early stage of SPD, i.e. below 6 passes, the microstructure comprises mainly a cellular dislocation structure will thick cell walls. With increasing SPD strain, the cellular structure gradually transforms into a subgrain/grain structure owing to dynamic recovery. The volume fraction of grain boundaries is increased during grain refinement. Although both cell walls and subgrain/grain boundaries obstruct dislocation motion, the underlying interaction mechanisms are different. Cell walls with high density of forest dislocations density hinder the motion of the mobile dislocations effectively, however, eventually they can be penetrated [Roters 2000]. Owing to the arrest of the mobile dislocations at the cell walls, DSA is intensified; i.e. m_{DSA} becomes more negative during the first few passes, when the fraction of cell walls increases. On the other hand, the cell structure does not influence m_i to the same degree as m_{DSA}. The penetration of cell walls requires essentially the cutting of forest dislocations which is relatively rate-insensitive in fcc metals. By contrast, grain boundary cannot be penetrated. At a later stage of SPD, i.e. after 6 CCDP passes, the fraction of subgrain/grain boundaries is so high that GB deformation mechanisms, e.g. grain boundary sliding, become increasingly activated. The related strongly reduced activation volume (see subsequent section) gives rise to an effective increase of m_i. Whereas the pile-ups of mobile dislocation in front of GBs remains of low impact on the SRS, thus slowing down the growth rate of m_{DSA}. In summary, the opposite development of m_{DSA} and m_i causes a minimum of m_s, at 6th pass(Figure 4.7).

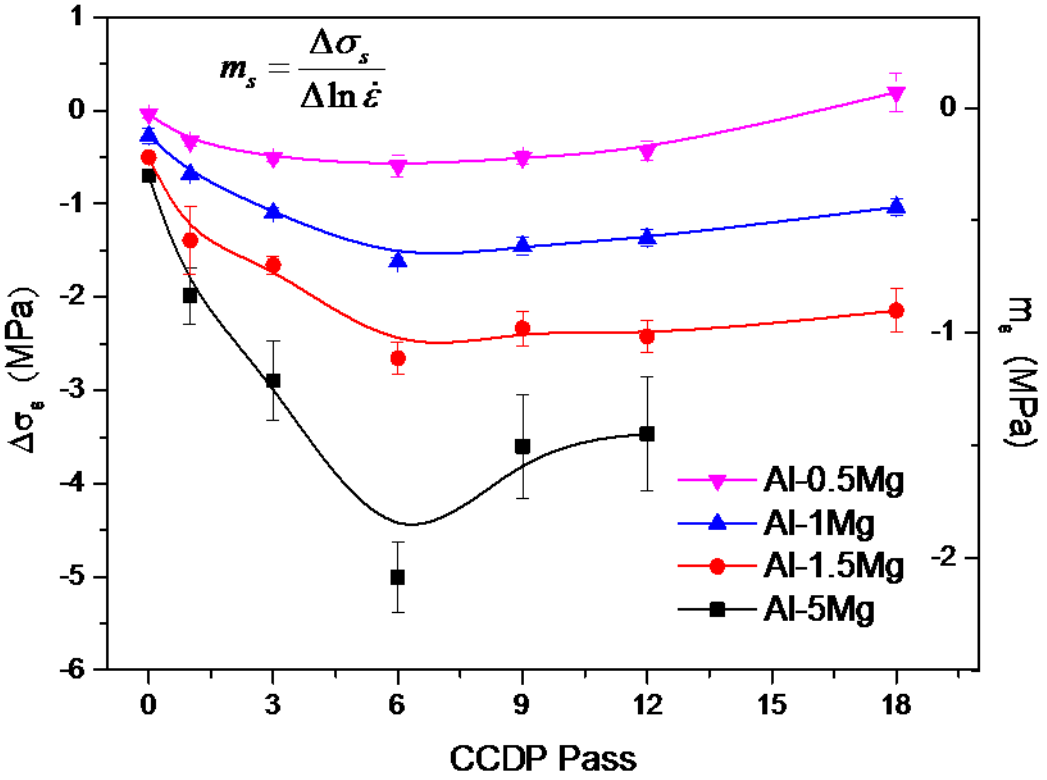

Figure 4.7: Evolution of steady state SRS with increasing number of CCDP passes for different Al-Mg alloys.

4.1.2.3 Activation volume and deformation mechanisms

The activation volume is considered as an indicator of the deformation mechanism in crystal plasticity. The motion of a mobile dislocation is a thermally activated and stress assisted process, therefore its velocity v obeys an Arrhenius relationship,

$$v = a\exp(-\frac{\Delta G(\tau)}{kT}) \qquad (4.5)$$

Correspondingly, according to Orowan, the shear strain rate $\dot{\gamma}$

$$\dot{\gamma} = \rho b v \qquad (4.6)$$

or

$$\dot{\gamma} = \dot{\gamma}_0 \exp(-\frac{\Delta G(\tau)}{kT}) \qquad (4.7)$$

where $\Delta G, k, T$ are the free activation energy, Boltzmann factor and absolute temperature, respectively; ρ is the mobile dislocation density and b the Burgers vector; $\dot{\gamma}_0$ is the pre-exponential factor.

During the motion of a dislocation, it has to overcome both the resistance from parallel and forest dislocations, i.e. the shear stress τ_0 necessary for motion in its glide system reads

$$\tau_0 = \tau_{pass} + \tau_{cut} \qquad (4.8)$$

The passing stress τ_{pass} results from the long range stress field of parallel dislocations of density ρ_p

$$\tau_{pass} = \alpha G b \sqrt{\rho_p} \qquad (4.9)$$

Here α is the geometrical factor of the order of 0.5. τ_{pass} depends on temperature only via the temperature dependence of the shear modulus G, i.e. only very mildly. Therefore, it is also referred as athermal flow stress τ_{ath}.

An applied resolved shear stress τ_{ext} has to attain τ_0 to set off plastic deformation. While the total free energy change for overcoming the cutting resistance is ΔG_0, the thermal activation barrier is lowered by the applied stress

$$\dot{\gamma} = \dot{\gamma}_0 \exp\left(-\frac{\Delta G_0 - (\tau_{ext} - \tau_{ath}) v^*}{kT}\right) \qquad (4.10)$$

where v^* is the activation volume

$$v^* = b \cdot d \cdot l^* \approx b^2 \cdot l^* \qquad (4.11)$$

l^* is the activation length, i.e. average spacing of forest dislocations $\frac{1}{\sqrt{\rho_f}}$. d is the obstacle width and for the cutting process equivalent to the Burgers vector. The product $b \cdot l^*$ is also referred to as the activation area.

One can extract v^* from Eq. (4.10),

$$v^* = -\frac{\partial \Delta G}{\partial \tau} = kT \cdot \frac{\partial ln\dot{\gamma}}{\partial \tau} = kT \cdot \frac{\Delta ln\dot{\gamma}}{\Delta \tau} = kT \cdot \frac{M \Delta ln\dot{\varepsilon}}{\Delta \sigma} \qquad (4.12)$$

M is the Taylor factor and $\tau \equiv \tau_{ext}$. $\Delta\sigma$ is the observed stress differential at an instantaneous change of the strain rate $\dot{\varepsilon}$. If we define the instantaneous SRS as

$$m_i = \frac{\Delta\sigma}{\Delta ln\dot{\varepsilon}} \qquad (4.13)$$

then the activation volume can be simplified to

$$v^* = MkT/m_i \qquad (4.14)$$

The activation length and accordingly the forest dislocation density are also available by

$$l^* = \frac{v^*}{b^2} = \frac{MKT}{m_i b^2} = \frac{1}{\sqrt{\rho_f}} \qquad (4.15)$$

SRJTs were performed to obtain the SRS of the investigated alloys. Specifically, $\Delta\sigma$ and $\Delta ln\dot{\varepsilon}$ were measured at the strain rate jump points, and $v^*$and l^*were calculated according to Eqs. (4.14) and (4.15). The development of activation volume and activation length of Al-5Mg with CCDP pass number is shown in Figure 4.8.

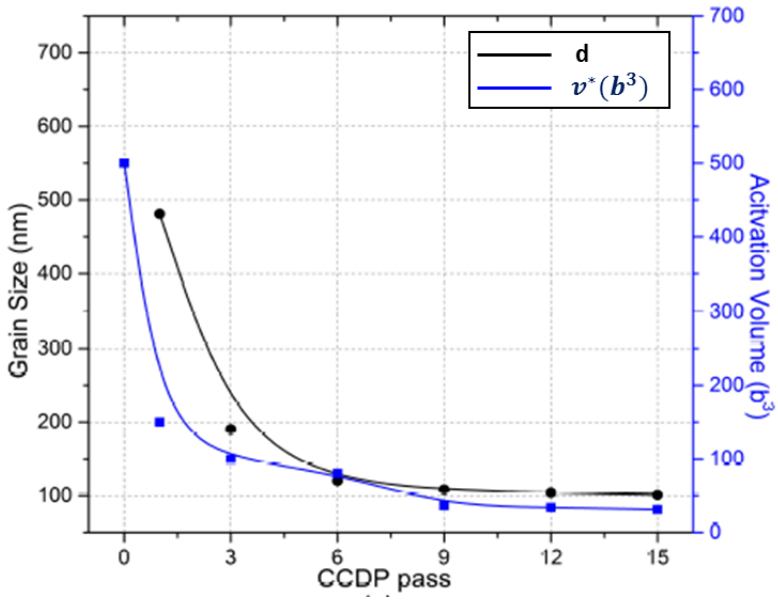

Figure 4.8: Dependence of grain size and activation volume on CCDP pass number for Al-5Mg.

It is obvious from Figure 4.8 that the activation volume follows the same trend as the grain size with progressing CCDP, i.e. the finer the grain size, the smaller the activation volume. The slope of both curves decreases strongly after P3. A quasi-steady state is reached at P15 with a minimum grain size of ≈ 100 nm, with a corresponding activation volume of $30b^3$ or

an activation length of 9 nm. The dependence of activation volume and activation length on SPD degree can be related to the microstructure evolution. With each pass of CCDP a large density of forest dislocations is generated, resulting in a decrease of the dislocation spacing and thus, of the activation volume. Besides, the cutting process also leads to jogs on the dislocations, which also act as pinning points and thus, further reduce the activation length (volume). Eventually a quasi-steady state is reached as indicated by the attainment of a minimum grain size. It is therefore concluded that dislocation glide is still the dominant deformation mechanism up to a high number of CCDP passes. TEM observations confirmed a significant density of dislocations in the microstructure of UFG Al-Mg alloys.

Compared to room temperature deformation the SRS became an order of magitude larger for deformation at elevated temperatures. This indicated that the deformation mechanism gradually changed with increasing temperature, probably owing to climb contributing increasingly to dynamic recovery [Yavari 1981]. This will be addressed in Sec. 4.2.

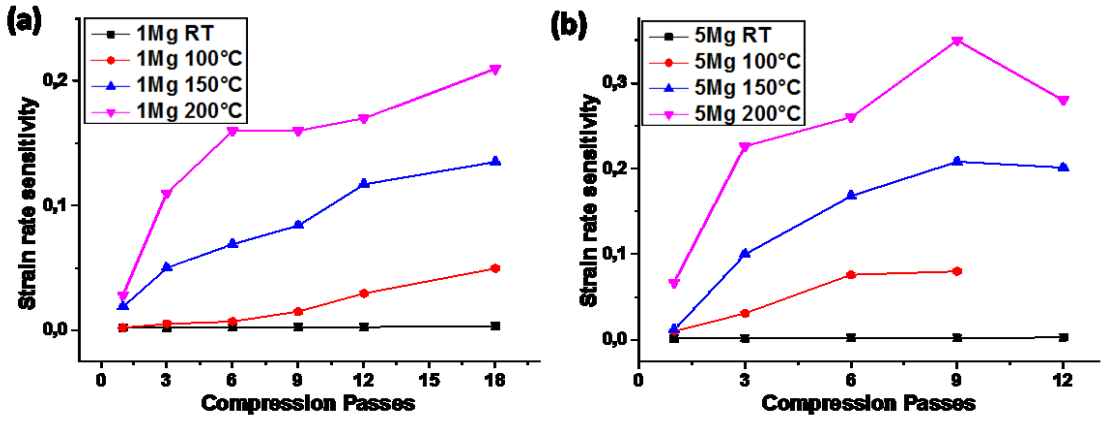

Figure 4.9: Development of strain rate sensitivity with progressing CCDP of Al-1Mg (a) and Al-5Mg (b) at different temperatures.

4.1.3 Dynamic strain aging

4.1.3.1 Asymmetry of stress response during SRJTs

During the SRJTs, the stress response exhibited a distinct difference in terms of the strain rate jump direction, i.e. the instantaneous stress response $\Delta\sigma_i$, the instantaneous SRS m_i and the transient time t_t were always one order of magnitude larger for rate-down transients than for rate rate-up changes, see Figure 4.10. This difference grew with increasing number of CCDP passes and Mg content.

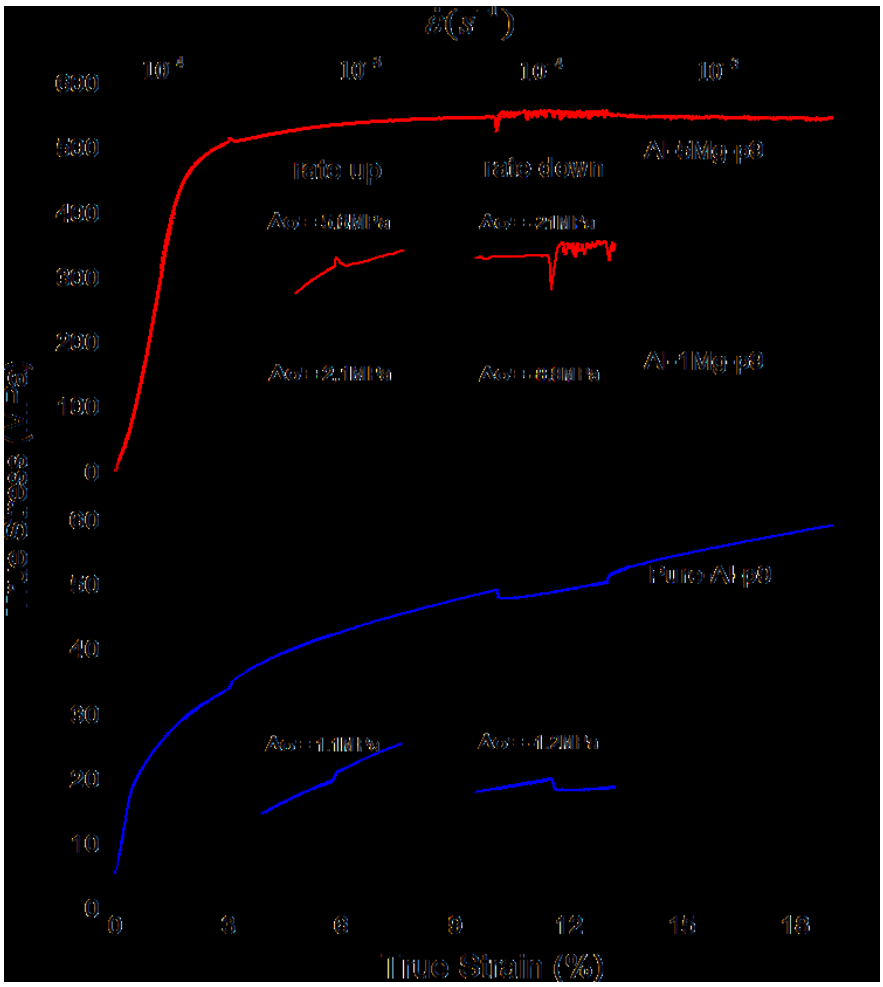

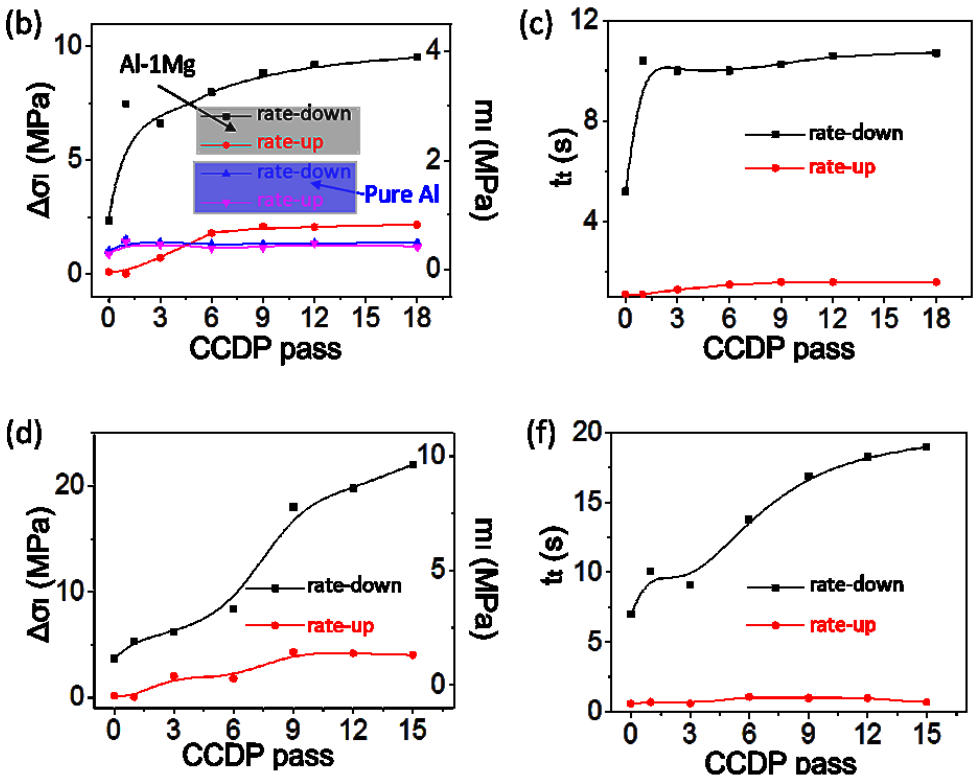

Figure 4.10: Flow curve and local blow-up at the strain rate jump points for Al-5Mg, Al-1Mg and pure Al, respectively (a). Evolution with rising number of passes: $\Delta\sigma_i$ and m_i of Al-1Mg and pure Al (b), t_t of Al-1Mg (c), $\Delta\sigma_i$ and m_i of Al-5Mg (d), t_t of Al-5Mg (f).

Consider the case of an upward jump with changing the strain rate from $\dot{\varepsilon}_1$ to $\dot{\varepsilon}_2$, where $\dot{\varepsilon}_1 < \dot{\varepsilon}_2$. The initial stress state at $\dot{\varepsilon}_1$ can be expressed as

$$\sigma(\dot{\varepsilon}_1) = \sigma_{th}(\dot{\varepsilon}_1, T) + \sigma_a + \sigma_{DSA}(\dot{\varepsilon}_1, T, C(\dot{\varepsilon}_1, T)) \qquad (4.16)$$

where $\sigma_{th}(\dot{\varepsilon}_1, T)$is the thermal stress component as function of strain rate and temperature, σ_a is the athermal stress component that is only mildly affected by temperature and independent of strain rate, and $\sigma_{DSA}(\dot{\varepsilon}_1, T, C(\dot{\varepsilon}_1, T)$ is the pinning stress exerted by solute atoms on mobile dislocation while the latter are waiting in front of an obstacle, i.e. PLC effect. On the one hand $\sigma_{DSA}(\dot{\varepsilon}_1, T, C(\dot{\varepsilon}_1, T)$ has the character of a thermal component owing to short range interactions of hindered dislocations with solute atoms. On the other hand it also possesses the character of an athermal component due to the solute concentration $C(\dot{\varepsilon}_1, T)$ at arrested mobile dislocations. Note that $C(\dot{\varepsilon}_1, T)$ has the opposite dependency on strain rate and temperature compared to $\sigma_{th}(\dot{\varepsilon}_1, T)$, i.e. a lower $\dot{\varepsilon}$ or higher T would lead to a larger σ_{DSA}

because of the stronger solute segregation. All tests were conducted at RT, thus, merely $\dot{\varepsilon}$ and C were variables. Hence, Eq. (4.16) can be simplified to

$$\sigma(\dot{\varepsilon}_1) = \sigma_{th}(\dot{\varepsilon}_1) + \sigma_a + \sigma_{DSA}(\dot{\varepsilon}_1, C(\dot{\varepsilon}_1)) \qquad (4.17)$$

At the moment of a strain rate change, the flow stress increases instantaneously to

$$\sigma(\dot{\varepsilon}_2) = \sigma_{th}(\dot{\varepsilon}_2) + \sigma_a + \sigma_{DSA}(\dot{\varepsilon}_2, C(\dot{\varepsilon}_1)) \qquad (4.18)$$

where only the $C(\dot{\varepsilon}_1)$ remains at the concentration of the initial state, since the aging solute concentration would not change immediately due to the diffusion (time) dependent nature of segregation. The instantaneous stress response

$$\Delta\sigma(up) = \sigma(\dot{\varepsilon}_2) - \sigma(\dot{\varepsilon}_1) = \sigma_{th}(\dot{\varepsilon}_2) - \sigma_{th}(\dot{\varepsilon}_1) + \sigma_{DSA}\big(\dot{\varepsilon}_2, C(\dot{\varepsilon}_1)\big) - \sigma_{DSA}\big(\dot{\varepsilon}_1, C(\dot{\varepsilon}_1)\big)$$

$$= \Delta\sigma_{th}(\dot{\varepsilon}_{2-1}) + \Delta\sigma_{DSA}\big(\dot{\varepsilon}_2 - \dot{\varepsilon}_1, C(\dot{\varepsilon}_1)\big) = \Delta\sigma_{th} + \sigma'_{DSA}(C(\dot{\varepsilon}_1)) \qquad (4.19)$$

in which $\Delta\sigma_{th}$ reflects the strain rate sensitivity of σ_{th} at constant dislocation structure. $\sigma'_{DSA}\big(C(\dot{\varepsilon}_1)\big) = \sigma_{DSA}\big(\dot{\varepsilon}_2, C(\dot{\varepsilon}_1)\big) - \sigma_{DSA}\big(\dot{\varepsilon}_1, C(\dot{\varepsilon}_1)\big)$ is defined as the effective (net) pinning stress caused by solute pinning of the arrested dislocations at the moment of a strain rate change from $\dot{\varepsilon}_1$ to $\dot{\varepsilon}_2$. The absolute value of $\sigma_{DSA}\big(\dot{\varepsilon}_1, C(\dot{\varepsilon}_1)\big)$ is larger than that of $\sigma_{DSA}\big(\dot{\varepsilon}_2, C(\dot{\varepsilon}_1)\big)$ since the higher strain rate results in a shorter waiting time and thus, less segregation of solutes contributing to the stress. Therefore the magnitude and direction of $\Delta\sigma(up)$is determined by $\Delta\sigma_{th}\ and\ \sigma'_{DSA}(C(\dot{\varepsilon}_1)$. As evident from Figure 4.10, all measured $\Delta\sigma(up)$ show positive values, i.e. $|\Delta\sigma_{th}(\dot{\varepsilon}_{2-1})| > |\sigma'_{DSA}(C(\dot{\varepsilon}_1))|$.

The downwards stress change can be written as

$$\Delta\sigma(down) = \sigma(\dot{\varepsilon}_1) - \sigma(\dot{\varepsilon}_2) = \sigma_{th}(\dot{\varepsilon}_1) - \sigma_{th}(\dot{\varepsilon}_2) + \sigma_{DSA}\big(\dot{\varepsilon}_1, C(\dot{\varepsilon}_2)\big) - \sigma_{DSA}\big(\dot{\varepsilon}_2, C(\dot{\varepsilon}_2)\big)$$

$$= \Delta\sigma_{th}(\dot{\varepsilon}_{1-2}) + \Delta\sigma_{DSA}\big(\dot{\varepsilon}_1 - \dot{\varepsilon}_2, C(\dot{\varepsilon}_2)\big) = \Delta\sigma_{th}(\dot{\varepsilon}_{1-2}) + \sigma'_{DSA}(C(\dot{\varepsilon}_2)) \qquad (4.20)$$

Adding Eq. (4.19) and (4.20) in absolute terms we obtain

$$|\Delta\sigma(up) + \Delta\sigma(down)| = \big|\Delta\sigma_{th}(\dot{\varepsilon}_{2-1}) + \Delta\sigma_{DSA}\big(\dot{\varepsilon}_2 - \dot{\varepsilon}_1, C(\dot{\varepsilon}_1)\big) + \Delta\sigma_{th}(\dot{\varepsilon}_{1-2}) +$$
$$\Delta\sigma_{DSA}\big(\dot{\varepsilon}_1 - \dot{\varepsilon}_2, C(\dot{\varepsilon}_2)\big)\big| = \big|\sigma'_{DSA}\big(C(\dot{\varepsilon}_1)\big) + \sigma'_{DSA}(C(\dot{\varepsilon}_2)\big| \qquad (4.21)$$

Note that the components of the thermal stress terms $\Delta\sigma_{th}(\dot{\varepsilon}_{2-1})$and $\Delta\sigma_{th}(\dot{\varepsilon}_{1-2})$ have to be taken equal in magnitude but opposite in sign, as proved valid by double SRJTs on pure Al

(Figure 4.10 (a) and (b)). In DSA-free pure Al, the thermal stress response for different transitions is essentially the same. Ultimately, Eq. (4.21) reveals the physical cause of the asymmetry in $\Delta\sigma_i$, which is that the stress response difference in terms of strain rate jump direction only relies on the DSA stress components at the adjoining steady states before and after the sudden rate jump.

In the current study all absolute values of $\Delta\sigma_i(down)$ were larger than that of $\Delta\sigma_i(up)$, which is consistent with the fact that a lower strain rate yielded a stronger interaction between solutes and dislocations, thus, larger σ'_{DSA}. According to Eq. (4.21), the evolution of $\left|\sigma'_{DSA}\left(C(\dot{\varepsilon}_1)\right) + \sigma'_{DSA}(C(\dot{\varepsilon}_2)\right|$ with increasing CCDP pass can be determined by utilizing the experimentally measured $\Delta\sigma_i(up)$ and $\Delta\sigma_i(down)$ from Figure 4.10(d). The result obtained on the UFG Al-5Mg alloy is depicted in Figure 4.11. It confirms experimentally that grain refinement by SPD does have an influence on DSA in UFG Al-Mg alloys by amplifying the additional back driving force for dislocation glide $\Delta\sigma_{DSA}$.

It is commonly accepted that DSA takes place during the arrest of mobile dislocations at immobile ones. Compared to the undeformed material where the forest dislocations are homogeneously distributed throughout the grain, the UFG Al-Mg alloys fabricated by CCDP possessed a heterogeneous distribution of dislocations, i.e. accumulated at cell walls or grain boundaries. Since the grain size was small and the dislocation density was remarkably high, the slip length of mobile dislocations was substantially shortened, thus, their waiting time in front of obstacles increased, giving solute atoms more time to diffuse towards the waiting dislocations. This increased the possibility for the DSA effect to reach its maximum. Regardless of the complexity of the underlying microscopic mechanism, the macroscopic flow curves revealed simply the enhancement of $\Delta\sigma_{DSA}$.

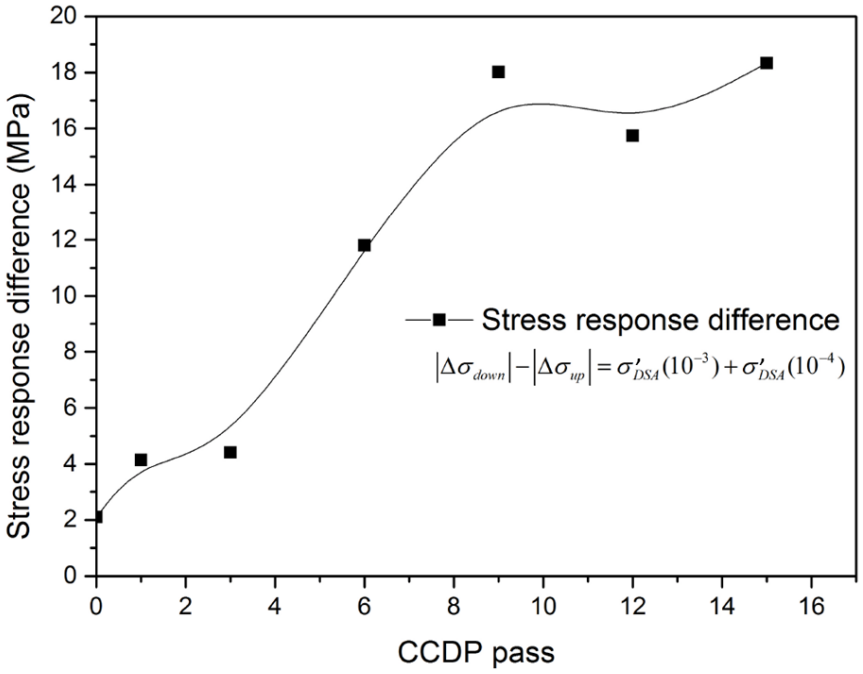

Figure 4.11: Relationship between stress response asymmetry and CCDP pass number.

The transient time t_t reflects the time needed to reestablish the dynamic equilibrium of DSA after the abrupt change of strain rate. Analogous to t_a and t_w, an analysis of t_t sheds some light on the kinetics of DSA. The time intervals t_a and t_w correspond to the time difference between dislocations being aged and arrested. All three characteristic times are strain rate dependent, i.e. a lower strain rate means a larger respective time, as confirmed by Figures 4.10 (c) (f).

4.1.3.2 DSA stress

DSA causes a back stress on mobile dislocations, the magnitude depending on aging time t_a at constant $\dot{\varepsilon}$. This owes to the increasing interaction energy between obstacles and dislocations, if t_a is large enough to enable sufficient solute diffusion. Although a direct means to determine t_a is so far unavailable, the measurement of t_t opens up an opportunity to investigate DSA kinetics. Hähner et al. related t_t to t_a with $\frac{1}{t_t} > \frac{1}{t_a}$, when m_s <0 [Hähner 1997]. If assuming that $t_t and\ t_a$ are of the same order of magnitude and that the aging time

depends only on the strain rate after the change, it is possible to utilize the experimentally measured t_t for a more refined analysis.

The waiting time t_w is another indicator of the DSA kinetics and in general, $t_w > t_a$. Kubin and Estrin introduced the "elementary strain **Ω**", a strain dependent quantity that corresponds to the strain increment obtained if all mobile dislocations would accomplish a successful activation event [Kubin 1990], and therefore related the waiting time to the strain rate as

$$\overline{t_w} = \frac{\Omega}{\dot{\varepsilon}} = \frac{b\rho_m\rho_f^{-1/2}}{\dot{\varepsilon}} = \frac{b\rho_m l^*}{\dot{\varepsilon}} \qquad (4.22)$$

If one assumes $3\rho_m = \rho_f$, and combines Eqs. (4.15) and (4.22)

$$\overline{t_w} = \frac{m_i b^3}{3KT\dot{\varepsilon}} \qquad (4.23),$$

Obviously, t_w increases with growing m_i and decreases with rising $\dot{\varepsilon}$. Based on the assumption of a cross core diffusion mechanism, Curtin et al. proposed a model to estimate $\Delta\sigma_{DSA}(t)$ by considering the dislocation-obstacle binding energy [Soare 2008, Soare 2008],

$$\sigma_{DSA}(t) = \sigma_{DSA}^{\infty}(1 - \exp(-(\frac{t}{t_d})^n)) \qquad (4.24)$$

where σ_{DSA}^{∞} is the saturated σ_{DSA} in case of full aging, t_d is the characteristic time of cross core diffusion, n ≈1 is an exponent related to the migration enthalpy of solute atoms for cross core diffusion. In the current study a slight modification was made, i.e. t is assumed to equal t_a, to simplify the evaluation of σ_{DSA}.

$$\sigma_{DSA}(t_a) = \sigma_{DSA}^{\infty}(1 - \exp(-(\frac{t_a}{t_d})^n)) \qquad (4.25)$$

By integrating Eq. (4.25) over the time interval [0, t_a], we obtain

$$\bar{\sigma}_{DSA} = \frac{\int_0^{t_a} \sigma_{DSA}^{\infty}(1-\exp(-(\frac{t_a}{t_d})^n))dt}{t_a} \qquad (4.26)$$

where $\bar{\sigma}_{DSA}$ is the mean DSA stress during t_a.

The average value of $\bar{\sigma}_{DSA}$ of Al-5Mg deformed at $\dot{\varepsilon} = 1 \times 10^{-4}s^{-1}$ and $\dot{\varepsilon} = 1 \times 10^{-3}s^{-1}$ was calculated under two assumptions, i.e. $t_a = t_t$ and $t_a = 0.2t_w$, respectively. Here t_w was

calculated from Eq. (4.23) utilizing the experimentally measured value of m_i, t_t was taken from the experimental results shown in Figure 4.10 (c) and (e). Parameters such as $\sigma_{DSA}^{\infty} = 210MPa$ and t_d=6.3s were adopted from [Soare 2008]. The final results are shown in Figure 4.12, as function of CCDP pass number. The influence of strain rate on the DSA effect of UFG Al-Mg alloys is depicted by Figure 4.12 (a), i.e. a lower strain rate facilitates the interaction and thus leads to a larger σ_{DSA}. What is more, the influence of SPD on DSA is significantly intensified by lowering the strain rate.

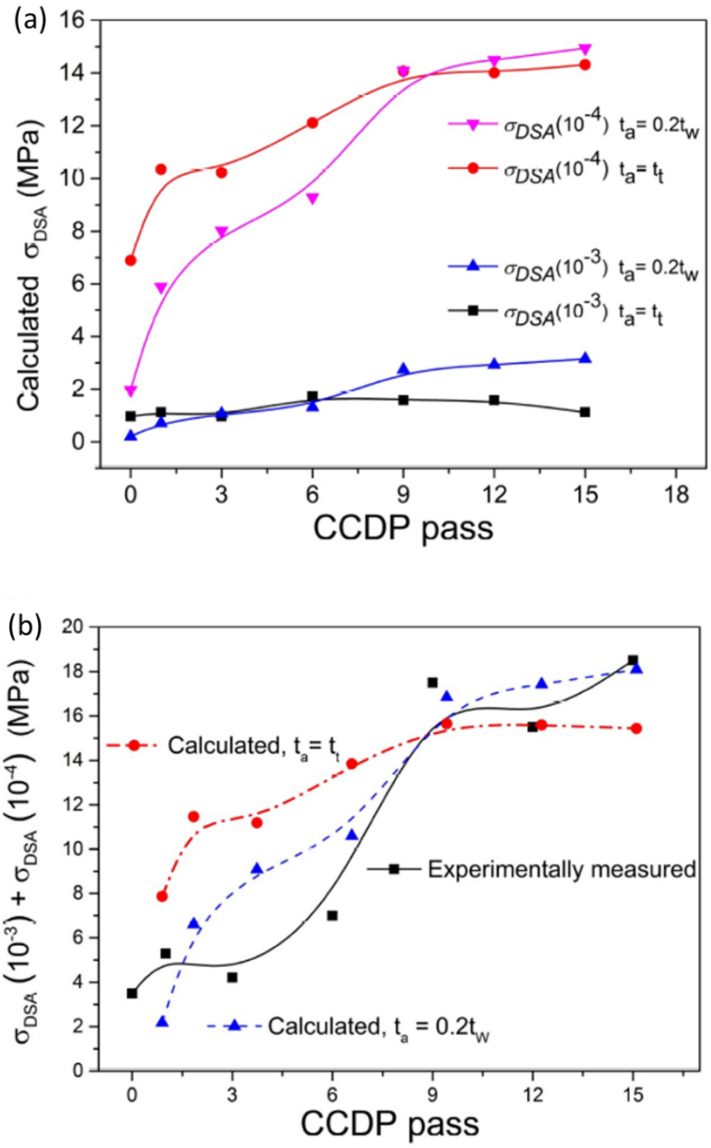

Figure 4.12: Development of σ_{DSA} with progressing CCDP for Al-5Mg. Calculated σ_{DSA} at two strain rates with $t_a = t_t$ and $t_a = 0.2t_w$, respectively (a). Comparison of $\sigma_{DSA}(10^{-4}s^{-1}) + \sigma_{DSA}(10^{-3}s^{-1})$, experimentally measured and calculated [b].

It can be seen from Figure 4.12 (b) that both the experimentally measured effective σ'_{DSA} and the calculated mean values of $\bar{\sigma}_{DSA}$ exhibit a similar trend with progressing CCDP, irrespective of the discrepancy between them during the first few passes, i.e. 1- 6 passes. This discrepancy is associated with the heterogeneous microstructure, e.g. mixture of cellular dislocation structure and grain/subgrains with lower dislocation density. Such inhomogeneity complicates the dynamic interaction of solute atoms and dislocations and causes an uncertainty for determining t_a and t_w. By contrast, after sufficiently high SPD strain, i.e. after 9 passes, the microstructure develops to a relatively more uniform grain/subgrains structure, and thus, weakens the impact of microstructure inhomogeneity on t_a and t_w.

4.1.3.3 Critical strain

The PLC effect does not necessarily manifest itself from the beginning of plastic deformation. The critical strain is defined as the strain corresponding to the onset of the PLC effect, prior to which no apparent DSA is observed. Therefore, one important objective of this study was to understand the initiation of DSA, i.e. the critical strain.

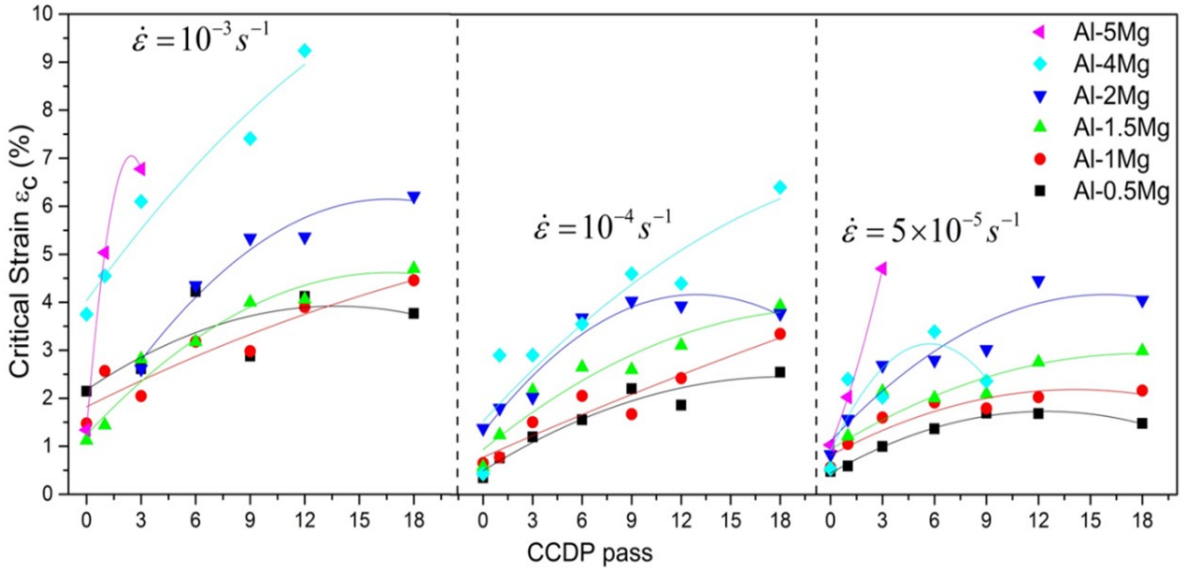

Figure 4.13: Influence of Mg content, CCDP pass number and strain rate on the critical strain for DSA of Al-Mg alloys.

The critical strain ε_c of Al-Mg alloys subjected to SPD was obtained by room temperature tensile tests at various constant strain rates (Figure 4.13). During the measurement, the stress fluctuations caused by the testing machine were taken into account to define a zero reference. A common tendency of ε_c (Figure 4.13) was that ε_c increased with increasing CCDP pass number. This may be attributed to strain enhanced diffusion and thus, to increased solute concentration and pinning stress at arrested dislocations, making the serrated flow to take place at larger strain under a higher flow stress as proposed by van den Beukel [van den Beukel 1975]. Besides, ε_c became larger with increasing strain rate, denoted as the normal relationship of ε_c with $\dot{\varepsilon}$. Furthermore, after 3 passes, it became apparent that ε_c grew with higher Mg content at the same SPD degree. This behavior is opposite to their undeformed (coarse grain) counterparts, in which ε_c decreased with increasing solute concentration [Vandenbrink 1975]. Estrin and Kubin also defined another critical strain that marked the end of the PLC effect, referred to as up-critical strain. However, this upper limitation of serrated flow was not observed in the current study.

As derived in Sec. 4.1.2.3,

$$\dot{\varepsilon} = \dot{\varepsilon}_0 \exp(-\frac{\Delta G}{KT}) \qquad (4.7)$$

On this basis McCormick proposed a model to connect the strain rate to the DSA effect in fcc alloys [McCormick 1971, McCormick 1972],

$$\dot{\varepsilon} = \frac{4b\rho c_v D_0 \exp(-Q_m/kT)}{d_{sol}} \qquad (4.27)$$

where $c_v = K\varepsilon^{\alpha}$, $\rho = N\varepsilon^{ß}$ are the vacancy concentration and the dislocation density ($K \approx 10^{-4}, N \approx 10^{11}$), respectively. D_0 is the diffusion pre-exponential factor, Q_m is the effective activation energy for solute migration, d_{sol} is the effective radius of the solute atmosphere. Eq. (4.27) can be rewritten as

$$\varepsilon_c^{\alpha+ß} = \frac{d_{sol}\dot{\varepsilon}\exp(Q_m/kT)}{4bkD_0} = A\dot{\varepsilon}\exp(Q_m/kT) \qquad (4.28)$$

where $A = \frac{d_{sol}}{4bKND_0}$is a material constant, and the exponent $(\alpha + ß) \approx 1.6\sim3.3$ for coarse grained Al alloys. Eq. (4.28) also indicates that the critical strain would grow with rising $\dot{\varepsilon}, Q_m \; and \; d_{sol}$.

In order to investigate the influence of SPD strain on ε_c of UFG Al-Mg alloys, some modifications of Eq. (4.28) are necessary. First, the solute migration energy Q_m is replaced by the binding energy $\Delta E(t_a)$ between dislocation core and solutes, which is a function of aging time t_a. Moreover, the effective radius of solute atmosphere is replaced by the increase of solute aging concentration $C(t_a, C_0)$ and solute atom radius r_{sol}, which is a function of t_a and alloy composition C. Both modified terms can be expressed as

$$\Delta E(t_a) = \Delta E_{\infty}^{core}[1 - \exp(\frac{-t_a}{t_d})] \qquad (4.29)$$

and

$$C(t_a, C_0) = C_{\infty}\left\{1 - \exp[-(\frac{C_0}{C_{\infty}})(\frac{t_a}{t_d})^n]\right\} \qquad (4.30)$$

where ΔE_{∞}^{core} and C_{∞} are the saturation binding energy and concentration in a fully aged state, respectively. t_d is the intrinsic cross core diffusion characteristic time. Combining Eqs. (4.28), (4.29) and (4.30) yields

$$\varepsilon_c^{\alpha+\beta} = AC(t_a, C_0)\dot{\varepsilon}\exp\left(\frac{\Delta E(t_a)}{kT}\right) = A\dot{\varepsilon}C_{\infty}\left\{1 - \exp[-(\frac{C_0}{C_{\infty}})(\frac{t_a}{t_d})^n]\right\}\exp\left(\frac{\Delta E_{\infty}^{core}[1-\exp(\frac{-t_a}{t_d})]}{kT}\right) \qquad (4.31)$$

Eq. (4.31) reflects qualitatively the influence of CCDP pass number and alloy concentration on ε_c. With progressing CCDP , t_t and thus t_a become larger and then lead to an increase of the solute aging concentration at dislocations and thus, the total binding energy. Consequently, ε_c is enlarged with increasing CCDP pass number. Moreover, an increasing C_0 also raises ε_c, as confirmed in current study. By determining all the related parameters, ε_c can be quantitatively evaluated. With the assumptions of $D_0 \approx 10^{-5}\mathrm{m^2s^{-1}}$ and $D_0 \approx 10^{-6}\mathrm{m^2s^{-1}}$ for CG and UFG Al-Mg alloys, respectively [Fujita 2004], $C_{\infty} \approx 10C_0$, r'_{sol} = 160 pm for Mg, t_a=t_t and t_d=6.3s , ΔE_{∞}^{core}≅0.004eV/Å for each 1% of Mg and a dislocation core width of $\overline{w} \approx 7.5b = 21$Å [Soare 2008] ΔE_{∞}^{core} was calculated to amount to about 0.42eV for Al-5Mg and about 0.084eV for Al-1Mg.

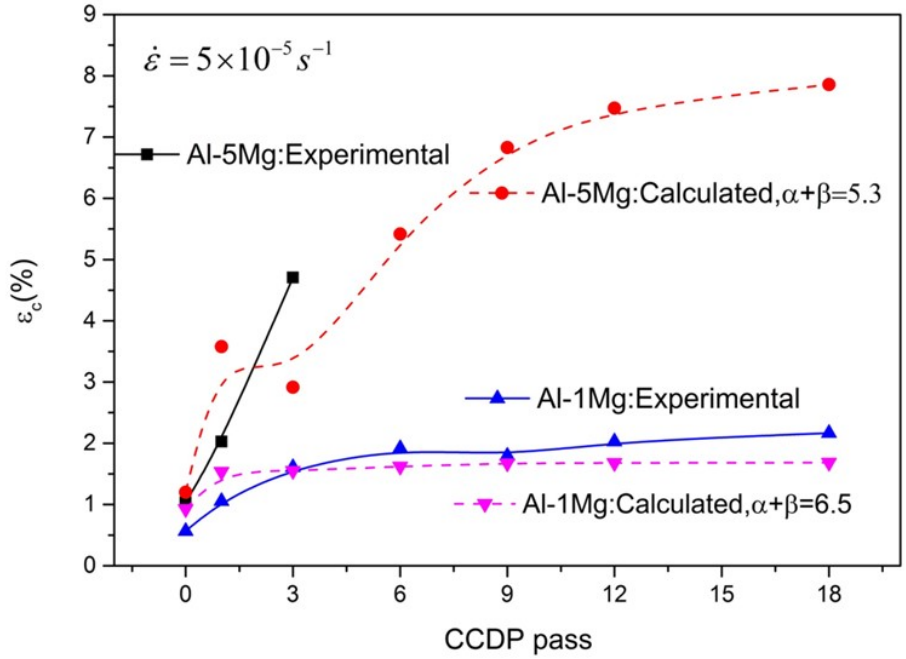

Figure 4.14: Comparison of calculation of critical strain with measured values.

The calculation results of ε_c as function of CCDP pass number are plotted in Figure 4.14, along with the measured data. Both experimentally measured and calculated results show good agreement. The necessary larger exponent $(\alpha + \beta)$ of ε_c used in the calculation, i.e. about $5.3 \leq (\alpha+\beta) \leq 6.5$ compared to $1.6 \leq (\alpha+\beta) \leq 3.3$ for CG Al-Mg alloys [McCormick 1972], was considered to be due to a larger density of vacancies and dislocations in UFG Al-Mg alloys subjected to CCDP. The evolution of ε_c with respect to strain rate and deformation temperature was studied comprehensively. ε_c increased with increasing strain rate (or decreasing T) as expected and referred to as normal relation. For other conditions the relationship may be reversed, which is denoted as abnormal relation. The latter, however, was not observed in our study.

In summary, the investigations carried out at room temperature revealed a strong influence of SPD processing on the DSA effect of Al-Mg alloys, which can be attributed to larger mobile and forest dislocation densities as well as an obviously refined grain size caused by SPD. The obstacle density was increased and thus, led to an amplified DSA effect by an increasing pinning stress and a prolonged aging and waiting time of arrested mobile dislocations at

obstacles. Consequently, a more pronounced serrated flow and retardation of the onset of serrated flow were observed.

4.2 Properties at elevated temperatures

4.2.1 Effect of preheating to test temperature

For an interpretation it is necessary to note that prior to conducting the SRJTs at elevated temperatures, the samples were heated up and stabilized at target temperature (soaking), which corresponds to a prior static annealing treatment of essentially 10 minutes for 100°C and 15 minutes for 200°C. Therefore, the yield stress given in Figure 3. 27 (a) corresponds to the dislocation density of each sample after heating, preceding SRJT. For Al-1Mg, it was noticed that the yield strength leveled off after P6, while the steady state stress increased all the way with increasing CCDP pass number, similar to its room temperature behavior. TEM results did not indicate recrystallization at 100°C for all CCDPed alloys. When the testing temperature was raised to 200°C, the yield stress started to decrease after P3 and the steady state stress no longer increased monotonically. As evident from Figure 3.12, for samples with high number of passes and therefore, with high stored energy, both recovery and partial recrystallization occurred during the heat treatment prior to the mechanical tests. Similar observations have been reported for other SPDed Al-Mg alloys [Wang 1996, Horita 2000]. In case of Al-5Mg, the significantly lower yield stress compared to samples after CCDP at room temperature suggested that preheating of the sample dramatically reduced the dislocation density without coarsening the grain size.

4.2.2 Deformation mechanisms

Contrary to the room temperature results, no asymmetry of the stress response after SRJTs was observed. Moreover, the transient to the steady state stress progressed in the same direction as the instantaneous stress differential contrary, to observations of room temperature deformation behavior (Figs. 2.5a and 4.17). This behavior sheds light on the underlying physical mechanisms of deformation. It is reminded that the instantaneous stress differential reflects the strain rate sensitivity at constant structure, whereas the long term (steady state) response yields information on the mechanisms after solute rearrangement.

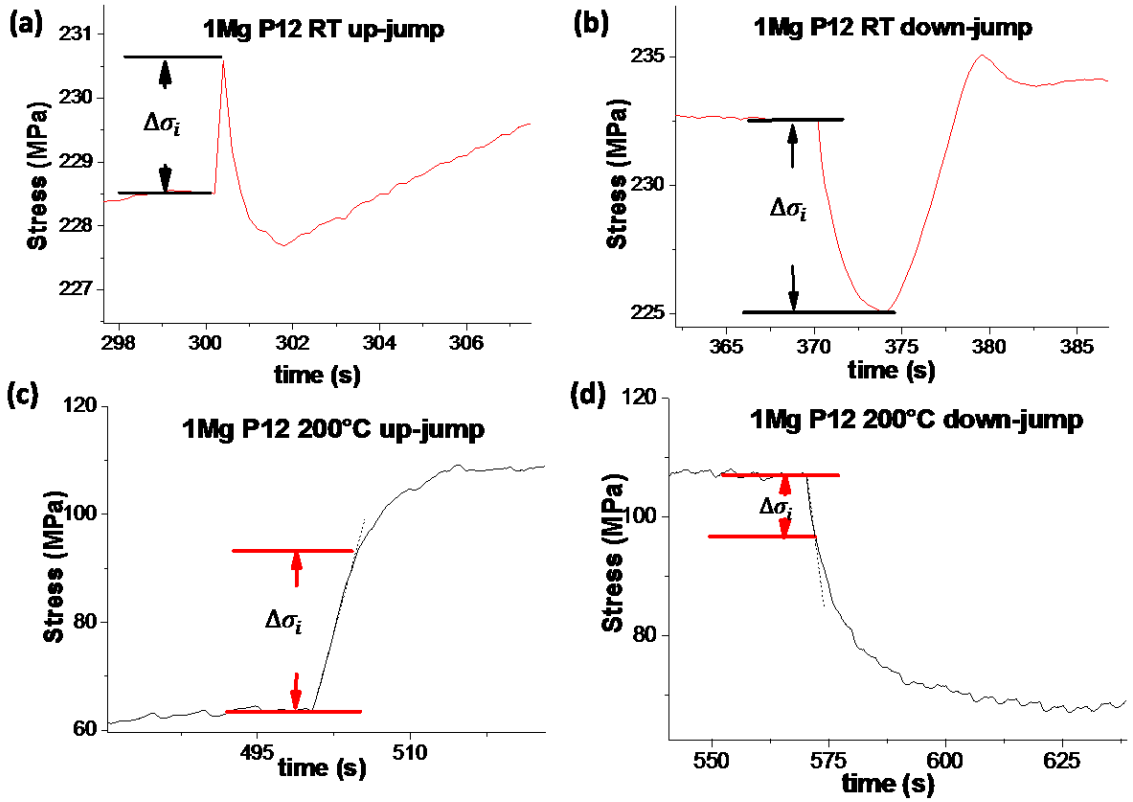

Figure 4.17: Comparison of instantaneous stress differential of Al-1Mg P12 at strain rate jump point at different temperatures (a) RT at strain rate up-jump, (b) RT at strain rate down-jump, (c) 200°C at strain rate up-jump and (d) 200°C at strain rate down-jump.

During room temperature deformation the activation volume indicates dislocation slip (including cross slip) as dominant deformation mechanism. With rising temperature the instantaneous SRS substantially increases, i.e. the activation volume decreases (Eq. 4.14). This indicates that also climb of edge dislocations increasingly contributes to the deformation process. Since both dislocation climb and segregation to dislocations are diffusion controlled,

we can assume that the dislocations during climb controlled motion carry essentially their equilibrium solute concentration characteristic for the deformation temperature. However, the friction stress of the solutes also contributes to the total flow stress. Under these conditions the transition of the deformation mechanisms with increasing temperature is investigated in the following.

The total strain rate is the sum of two separate contributions:

$$\dot{\varepsilon}_{total} = \dot{\varepsilon}_{glide} + \dot{\varepsilon}_{climb} \qquad (4.32)$$

where

$$\dot{\varepsilon}_{glide} = \dot{\varepsilon}_0 \cdot \exp\left(-\frac{\Delta G_0 - \sigma_{th} \cdot v^*}{kT}\right) \qquad (4.33)$$

and

$$\dot{\varepsilon}_{climb} = \rho b v_{climb} \qquad (4.34)$$

here $\Delta G_0$is the activation energy, σ_{th} is the thermal flow stress component, v^* is the activation volume, k is the Boltzmann constant, T is the absolute temperature, ρ is the dislocation density, and b is the Burgers vector.

More specifically, the thermal flow stress term σ_{th} is obtained by the subtraction of the athermal stress component σ_{ath} and the solute friction stress σ_c from the total applied stress. So Eq. (4.33) can be rewritten as

$$\dot{\varepsilon}_{glide} = \dot{\varepsilon}_0 \cdot \exp\left(-\frac{\Delta G_0 - (\sigma_{total} - \sigma_{ath} - \sigma_c) v^*}{kT}\right) \qquad (4.35)$$

In an approximation here for easier calculation purpose, the solute friction stress is determined by the root of the solute concentration at the dislocation, C_d,

$$\sigma_c = K\sqrt{C_d} \qquad (4.36)$$

C_d increases by segregation through diffusion of solutes and exerts a significant impact on the dislocation – solute interaction. An analytic solution for the segregation of solute atoms to a dislocation yields

$$C_d(t_a) = C_d^{\infty} \cdot (1 - \exp(-(\frac{t_a}{t_d})^n)) \qquad (4.37)$$

where C_d^{∞} is the saturation concentration of Mg solutes along a dislocation, t_a is the aging time, t_d is the intrinsic cross-core solute diffusion time at a given temperature (for example $t_d = 6.3$s at room temperature), and a value of n =1 is considered according to [Curtin 2006, Soare 2008]. The aging time t_a is related to the waiting time t_w of a mobile dislocation in front of an obstacle and usually of the same order of magnitude as $t_a > t_w$. According to Kubin and Estrin [Kubin 1990] we can therefore replace t_a in Eq. (4.37) by t_w

$$t_w = \frac{\Omega}{\dot{\varepsilon}} = \frac{b\rho_m\rho_f^{-0,5}}{\dot{\varepsilon}} \qquad (4.22a)$$

where Ω is a strain dependent quantity that equals the total deformation when all mobile dislocations accomplish an activation event, the so-called elementary strain. ρ_m and ρ_f are the mobile and forest dislocation densities, respectively. If assumed ρ_m=ρ_f [Soare 2008], Eq. (4.22a) can be rewritten as

$$t_w = \frac{b\rho_m\rho_f^{-0,5}}{\dot{\varepsilon}} = \frac{\sqrt{2}\sigma}{G\dot{\varepsilon}} \qquad (4.22b)$$

The velocity of dislocation climb is expressed as [Argon 1980]:

$$v_{Climb} = \frac{A\sigma V_a D}{bkT} c_{jog} \left(\frac{E_{SF}}{Gb}\right)_2 \qquad (4.38)$$

where $A_0 = 2(24\pi(1-\boldsymbol{\upsilon})/(2+\boldsymbol{\upsilon}))^2$ is a numerical constant depending on Poisson ratio $\boldsymbol{\upsilon}$, V_a is the atomic volume, D is the self-diffusion coefficient of Al (according to $D_{Al-Mg} = D_{Al}D_{Mg}/(X_{Al}D_{Mg+}X_{Mg}D_{Al})$ [Herring 1950, Weertman 1968] the diffusion of Mg in Al is equal to the self-diffusion of Al), E_{SF} is the stacking fault energy and c_{jog} is the jog concentration along a dislocation line.

The total jog concentration consists of thermally activated and athermally generated jogs

$$c_{jog} = c_{jog}^{ther} + c_{jog}^{ather} \qquad (4.39)$$

The concentration of thermal jogs is given according to [Hirth] [1]

$$c_{jog}^{ther} = 2 * \frac{b}{a} \exp\left(-\frac{F_j}{kT}\right) \qquad (4.40)$$

[1] In this model single jogs instead of jog pairs are considered with respect to the formation energy

where $a = \frac{V_a}{bd}$ is the removal distance of one atom at a jog, d is the spacing of slip planes, F_j is the energy of a pair of jogs which can be approximated as the sum of two average self-energies W_f and the jog-jog interaction energy W_{int},

$$F_j = 2W_f + W_{int} = 2 * \frac{Gb^3}{4\pi(1-\upsilon)} - \frac{Gb^3 \cdot b}{8\pi L(1-\upsilon)} \qquad (4.41)$$

The generation of athermal jogs through dislocation interactions is considered to be more pronounced in the current model since SPD significantly increases the dislocation density. For a single mobile dislocation c_{jog}^{ather} is proportional to the number of cutting processes by other dislocations expressed by the forest dislocation density ρ_f . ρ_f is determined from the microstructure right after SPD and represented by the yield stress,

$$c_{jog}^{ather} \sim \rho_f \sim \rho_{total} = B\sigma_y^2 \qquad (4.42)$$

Accordingly, the strain rate reads

$$\dot{\varepsilon}_{total} = \dot{\varepsilon}_0 \cdot \exp\left(-\frac{\Delta G_0 - (\sigma_{app} - \sigma_{ath} - \sigma_c)v^*}{kT}\right) + \left(\frac{\sigma_{app}}{\alpha G b}\right)^2 \cdot b \cdot \frac{A\sigma_{app}\boldsymbol{\Omega} D}{bkT} \cdot \left(\frac{E_{SF}}{Gb}\right)^2 \cdot (c_{jog}^{ther} + c_{jog}^{ather}) \qquad (4.43)$$

Figure 4.18 shows the stress – strain-rate dependency obtained using equation (4.43), where the transition from glide-dominated to climb-dominated deformation is evident from the slope change. The calculated transition from glide-dominated to climb-dominated dislocation motion qualitatively reflects the experimental observations depicted in Figs. 3.27 and 3.28.

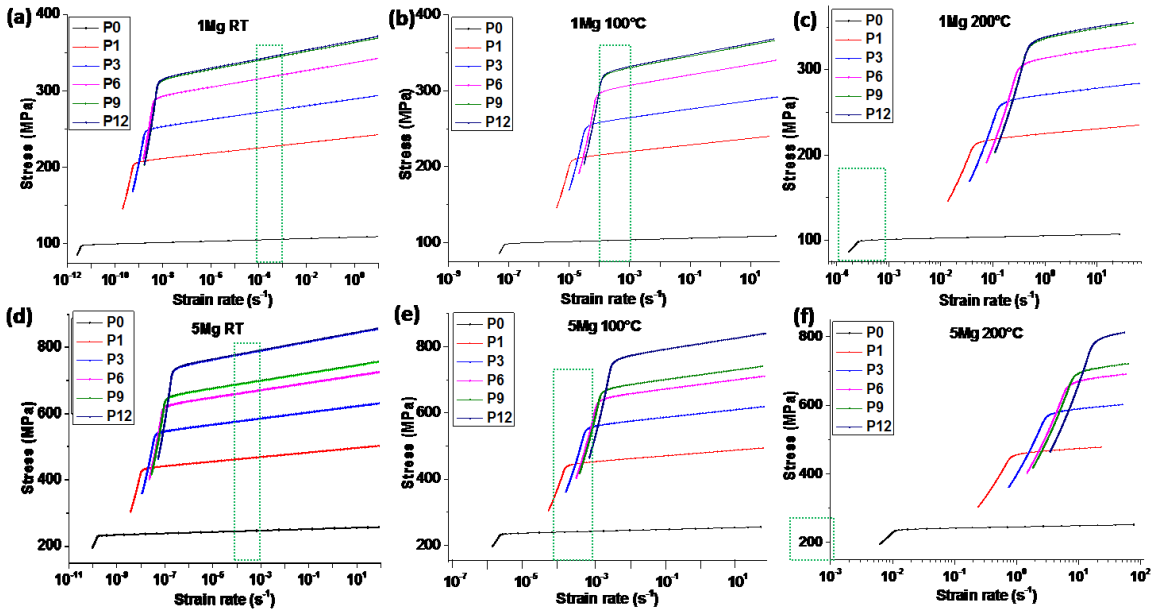

Figure 4.18: Calculated stress – strain-rate curves for Al-1Mg at RT (a), 100°C (b), 200°C (c) and Al-5Mg at RT (d), 100°C (e), 200°C (f). P0 refers to the undeformed material; P1 refers to the material subjected to 1 pass of CCDP, etc. The regions enclosed with a green dotted line are the strain rates utilized in the current experiments.

Specifically at room temperature, deformation is dominated by dislocation glide within the experimental strain rate range of the current study, i.e. $10^{-5}/s - 10^{-3}/s$ where the stress level increases monotonically with increasing SPD passes up to the saturation of the dislocation density. This is consistent with previous observations. At 100°C the transition region between glide-dominated and climb-dominated deformation lies in the experimentally applied strain rate region between $10^{-5} - 10^{-3}/s$, indicating that dislocation climb began to make itself felt in this interval. This is in agreement with the experimental observation of a large stress differential at the strain rate jump points. At 200°C, deformation is essentially climb-dominated.

Figure 4.19 shows calculated and experimentally measured flow stress and stress response at rate-change points as function of CCDP pass number for Al-1Mg and Al-5Mg at 100°C. It is pointed out that the calculated stresses are higher than reality, since the dislocation density reduction during sample heating was not taken into consideration. Nevertheless, both the calculated stress and stress response show good agreement with the trend of the experimental results.

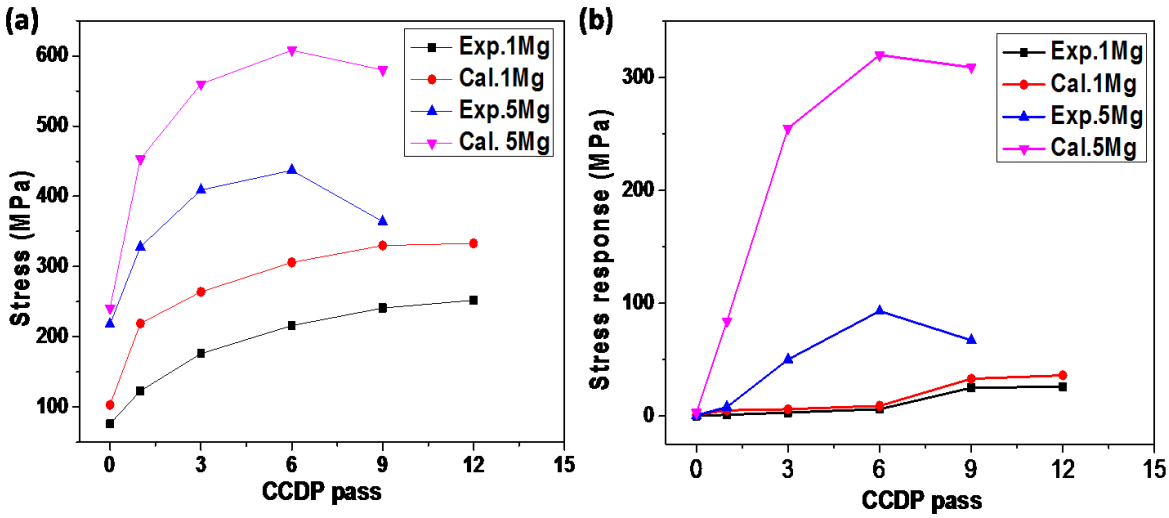

Figure 4.19: Calculated and experimentally measured flow stress (a) and stress response (b) of Al-1Mg and Al-5Mg at 100°C as function of CCDP pass number.

It is stressed that the model does not only account properly for the change of deformation behavior during strain rate jump tests, it also reveals the effect of prior SPD on the transition of deformation mechanism from dislocation glide to climb controlled dislocation motion. Owing to the growing number of deformation generated jogs on dislocations with increasing prestrain, an increase in the number of SPD passes makes itself felt in the same way as an increase in temperature which is accompanied by a higher thermal jog concentration. Thermal energy and expended deformation energy can therefore be considered as interchangeable processing parameters for the promotion or suppression of specific deformation mechanisms in the investigated Al-Mg alloys.

It is finally mentioned that the flow curves at elevated temperatures were evidently affected by microstructural restauration process like recovery and recrystallization during the heating up time prior to elevated temperature deformation (indicated by a decrease of the yield stress) and during deformation to larger strains (apparent from a negative work hardening rate). The experimental data were therefore predominantly taken from the initial part of the flow curve. It is interesting to note that the behavior predicted by the model also reflects the behavior of the samples effected by softening processes. Obviously, the mechanical behavior of partially

recovered or recrystallized structures still reflects the effects imparted by the prior SPD processing.

4.3 Relevance for sheet forming applications

The current research into the PLC effect can be also evaluated with respect to its implications for metal sheet forming applications. In any event serrated yielding is detrimental to the product quality and, hence, the PLC range has to be avoided to prevent the formation of surface markings and waviness induced on the sheets by the strain oscillations. For that purpose, the limits of the PLC regime were constructed based on the critical strains derived from the series of constant strain rate tensile tests (Figure 4.20). In the zone below the surface for the respective working conditions (strain rate) no PLC effect will occur.

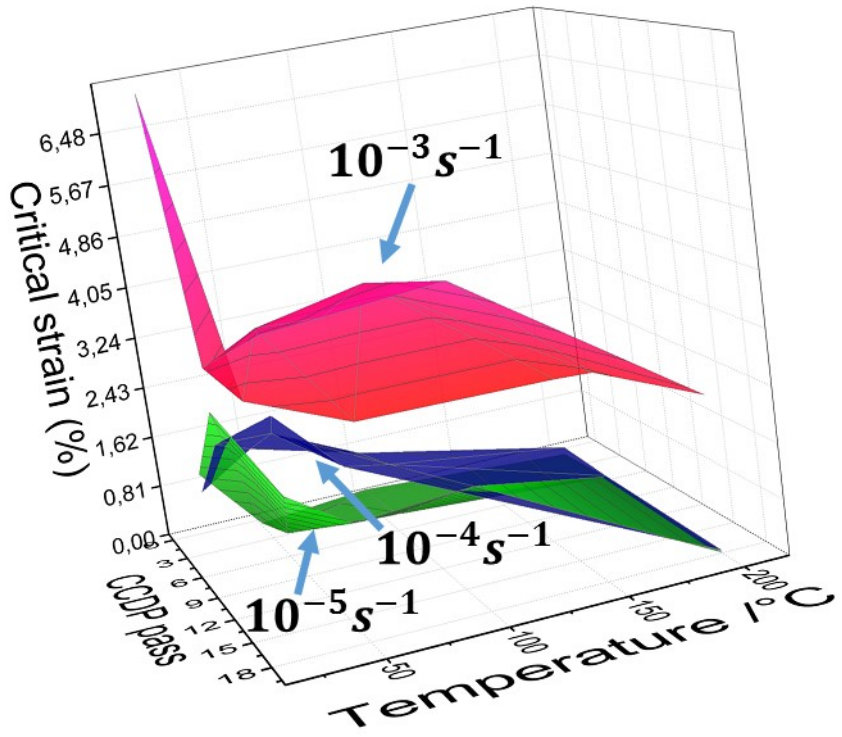

Figure 4.20. 3D map of critical strain ε_c of Al-1Mg for strain rates 10^{-3},10^{-4}, and 10^{-5}/s in dependence on CCDP pass number and temperature

It was observed that ε_c of UFG Al-Mg alloys increased with increasing SPD strain at ambient temperature, i.e. relatively low temperature. This may be attributed to strain enhanced diffusion and thus, to an increase of solute concentration and hence, stronger pinning stress for arrested dislocations, making serrated flow to occur at larger strains and at a higher flow stress. Upon increase of the temperature, e.g. 200° C, ε_c occurred already at very small strains and the influence of the prior SPD strain was negligible. This owes apparently to the accelerated diffusion kinetics, which allowed a segregation of solute atoms to dislocation to happen at incipient stages of deformation.

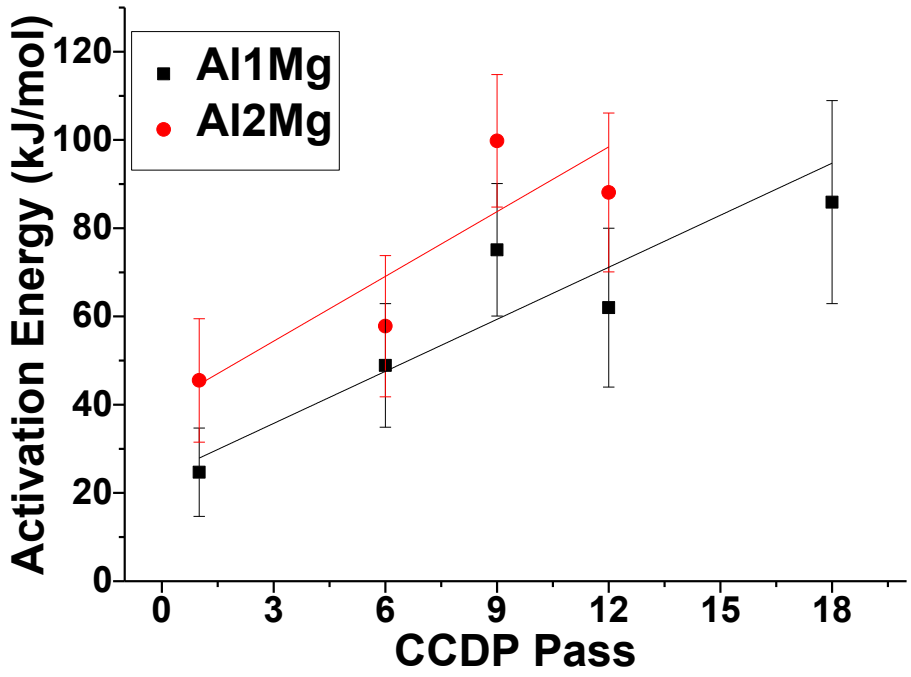

Figure 4.21: Calculated activation energies for serrated flow in two Al-Mg alloys with respect to ongoing CCDP pass.

Finally, Figure 4.21 reveals the calculated dependence of the activation energy for serrated flow in Al-Mg alloys on the number of CCDP passes using the critical strain from different testing temperatures and strain rates, based on Eq. (4.27) [McCormick 1972, Choudhary 2014]. Accordingly, an increasing SPD strain and a higher solute concentration cause the activation energy to increase from 30kJ/mol to 100kJ/mol for CCDPed Al-1Mgs.

5. Summary

This investigation addressed the dynamic strain aging (DSA) and the deformation behavior of ultrafine grained (UFG) solid solution Al-Mg alloys at ambient and various elevated temperatures. UFG materials were produced by confined channel die pressing (CCDP). TEM observations revealed that the microstructure of Al-Mg alloys was significantly refined by the applied severe plastic deformation (SPD). The minimum grain size decreased with increasing Mg content. The CCDP processed material was subsequently subjected to constant strain rate mechanical tests in compression or tension and to strain rate jump tests at room temperature and elevated temperatures up to 200°C. The material was characterized with respect to microstructure, crystallographic texture and mechanical properties after the various stages of processing.

At room temperature the study revealed a strong influence of CCDP processing on the PLC effect of Al-Mg alloys, which could be attributed to a deformation generated increase of the mobile and forest dislocation densities as well as an obviously substantially refined grain size. The corresponding reduction of the obstacle spacing for the mobile dislocations intensified the PLC effect by increasing the pinning stress and prolonging the aging and waiting time of arrested mobile dislocations at obstacles and consequently, amplifying the flow stress serrations and retarding the onset of serrated flow. The diffusion controlled segregation of solute atoms to dislocations caused an asymmetry of the instantaneous stress response for upward and downward strain rate changes, which grew with higher number of CCDP passes. This behavior was analyzed quantitatively, and it compared well to the predictions of a newly developed mechanical model which considered the magnitude of a DSA generated back stress at different strain rates. An increasing Mg content was found to strengthen the influence of SPD on dynamic strain aging of Al-Mg alloys.

The mechanical properties of the material were also investigated during deformation at various elevated temperatures up to 200°C. During short time annealing at moderately elevated temperatures (e.g. 30 min at 100°C) the overall microstructure remained in the

ultrafine range, but local microstructural restauration by recovery and recrystallization was obvious by a decrease of the elevated temperature yield stress with rising number of passes. Strain rate jump tests revealed a significant change of the flow stress response with increasing temperature, which substantially differed from room temperature behavior. The asymmetry of the stress differential for upward and downward strain rate changes disappeared and a more continuous stress transition, characteristic for the new deformation conditions, was observed. From the short term stress differential during strain rate changes it was found that the strain rate sensitivity, respectively the activation volume, markedly changed with temperature and SPD prestrain. A theoretical analysis proved that this behavior was associated with a change of deformation mechanisms from glide dominated dislocation motion at ambient temperature to climb controlled deformation at elevated temperatures. The model properly predicted that the transition was influenced not only by temperature but by the SPD prestrain as well. Essentially, it was shown that the thermal energy and the mechanically expended energy can be interchanged to engender the same mechanical material behavior. A larger number of CCDP passes or an increase in temperature substantially accelerate the transition.

Eventually, the impact of the results on sheet metal processing of materials liable to undergo DSA was addressed. From the theoretical analysis the critical strain for the onset of DSA can be derived. For practical applications a DSA diagram can be theoretically constructed that relates the critical strain to temperature, strain rate and prestrain. Alternatively, the activation energy for DSA in dependence on SPD prestrain can be predicted.

5. Zusammenfassung

Die vorliegende Untersuchung war befasst mit der dynamischen Reckalterung (DSA), bzw. dem Portevin-Le Chatelier (PLC) Effekt, und dem Verformungsverhalten von ultrafein-körnigen Al-Mg Mischkristallen bei Umgebungstemperatur und verschiedenen höheren Temperaturen. Die ultrafein-körnigen Materialien wurden durch Schmieden unter beschränkter Formänderung (CCDP) hergestellt. TEM Untersuchungen belegten, dass die Mikrostruktur der Al-Mg Legierungen durch sehr starke Umformung (SPD) erheblich verfeinert wurde. Die minimale Korngröße verringerte sich mit zunehmendem Magnesiumgehalt. Das durch CCDP hergestellte Material wurde anschließend mittels mechanischer Prüfung untersucht mittels dynamischer Zug- und Druckversuche bei konstanter Dehngeschwindigkeit und Dehngeschwindigkeits-Wechselexperimenten bei Raumtemperatur und erhöhten Temperaturen bis 200°C. Das Material wurde hinsichtlich Mikrostruktur, kristallographischer Textur und mechanischen Eigenschaften nach den jeweiligen Prozessschritten charakterisiert.

Die Studie zeigt, dass CCDP einen starken Einfluss auf den PLC Effekt der Al-Mg Legierungen nimmt, der sowohl auf die verformungsgenerierte starke Zunahme der mobilen Versetzungen und der immobilen Waldversetzungen als auch auf die wesentliche Kornfeinung zurückgeführt werden kann. Die entsprechende Verringerung des Hindernisabstandes für die Versetzungsbewegung verstärkt den PLC Effekt durch Erhöhung der Rückhaltespannung und Verlängerung der Wartezeit der aufgehaltenen mobilen Versetzungen vor den Hindernissen, wodurch die Spannungssprünge sich verstärken und der Beginn der DSA sich verzögert. Die diffusionsgesteuerte Segregation von Legierungsatomen zu den Versetzungen verursachte eine Asymmetrie des instantanen Spannungssprungs bei Aufwärts- und Abwärtswechseln der Dehngeschwindigkeit, die mit der Anzahl der CCDP Durchgänge zunahm. Dieses Verhalten wurde quantitativ analysiert und erfolgreich mit den Vorhersagen eines neu entwickelten mechanischen Modells verglichen, welches die Größe der DSA verursachten Rückspannung in Abhängigkeit von der Dehngeschwindigkeit

betrachtet. Es wurde festgestellt, dass ein erhöhter Magnesiumgehalt den Einfluss der Vorverformung auf die DSA von Al-Mg Legierungen noch verstärkt.

Die mechanischen Eigenschaften des Materials wurden auch durch mechanische Prüfung bei verschiedenen erhöhten Temperaturen bis zu 200°C untersucht. Nach kurzer Glühzeit bei mäßig erhöhten Temperaturen (zB. 30 min bei 100°C) blieb das Gefüge als Ganzes feinkörnig, aber lokale Mikrostrukturänderungen durch Erholung oder Rekristallisation waren messbar anhand einer Abnahme der Streckgrenze mit zunehmender Anzahl von CCDP Durchgängen. Dehngeschwindigkeits-Wechselexperimente belegten eine deutliche Änderung der Fließspannungsreaktion mit steigender Verformungstemperatur, die sich merklich vom Raumtemperaturverhalten unterschied. Die Asymmetrie des Spannungsprungs für Aufwärts- und Abwärtswechsel verschwand zugunsten einer mehr kontinuierlichen Spannungstransiente hin zu den neuen Verformungsbedingungen. Aus den Kurzzeitänderungen des Spannungssignals wurde abgeleitet, dass die Dehngeschwindigkeitsempfindlichkeit, bzw. das Aktivierungsvolumen sich merklich mit der Verformungstemperatur und der Vorverformung änderte. Ein theoretische Analyse wies nach, dass dieses Verhalten mit einer Änderung des Verformungsverhaltens verbunden war, nämlich von gleitkontrollierter Versetzungsbewegung zu klettergesteuerter Verformung bei höheren Temperaturen. Das Modell prognostizierte richtig, dass der Übergang nicht nur von der Temperatur sondern auch von der Vorverformung abhängt. Als fundamentales Ergebnis wurde gezeigt, dass thermische und mechanische Energie austauschbar sind, um das gleiche mechanische Verhalten zu erzeugen. Eine größere Anzahl von CCDP Durchgängen oder eine Temperaturerhöhung beschleunigen erheblich den Übergang.

Letztlich wird die Bedeutung der Ergebnisse für die Blechherstellung von Materialien mit Neigung zu DSA behandelt. Aus der theoretischen Analyse kann die kritische Dehnung für den Beginn des PLC Effekts hergeleitet werden. Für praktische Anwendungen wird ein DSA Diagramm berechnet, das die kritische Dehnung in Abhängigkeit von Temperatur, Dehngeschwindigkeit und Vorverformung darstellt. Alternativ kann die Aktivierungsenergie für DSA in Abhängigkeit vom Vorverformungsgrad vorhergesagt werden.

6. References

[Aboulfadl 2015] H.Aboulfadl, J.Deges, P.Choi, D.Raabe, Acta Mater, 2015; 86:34

[Ananthakrishna 2007] G.Ananthakrishna, Physics Reports, 2007; 440:113

[Argon 1980] AS.Argon, WC.Moffatt, Acta Metall, 1980; 29:293

[Balik 1993] J.Balik, P.Lukac, Acta Metall. Mater, 1993;41:1447

[Berghammer 2011] R.Berghammer, W.Hu, G.Gottstein, Adv Eng Mater, 2011; 13:232

[Brechet 1995] Y.Brechet, Y.Estrin, Acta Metall, 1995; 43:955

[Chang 2000] C.P.Chang, P.L.Sun, P.W.Kao, Acta Mater, 2000; 48:3377

[Chokshi 1993] Chokshi.A.H, Mukherjee.A.K, Langdon.T.G, Mater Sic Eng, 1993; R10:237

[Choudhary 2014] BK.Choudhary, Mater Sci Eng A, 2014; 603:160

[Chovet 2002] C.Chovet, Ch.Desrayyaud, F.Montheillet, Inter J Mech Sci, 2002; 44:343

[Cottrell 1953] Cottrell AH. Phila Mag 1953; 44:3

[Cottrell 1948] Cottrell AH. Bilby BA. Proc Phys Soc 1948; 62:14

[Cuddy 1972] L.J.Cuddy, W.C.Leslie, Acta Metall, 1972; 20:1157

[Curtin 2006] W.A.Curtin, D.L.Olmsted, L.G.Hector, Nature Materials, 2006; 5:875

[Draheim 1994] K.Draheim, Doctor thesis, RWTH Aachen University, 1994

[Dixit 2008] M.Dixit, R.S:Mishra, K.K.Sankaran, Mater Sci Eng A, 2008; 478:163

[Estrin 1995] Y.Estrin and L.P.Kubin, in *Continuum models for materials with microstructure*, New York, United States, Chichester, 1995.

[Estrin 1986] Y.Estrin, L.P.Kubin, Acta Metall, 1986; 34:2455

[Fujita 2004] T.Fujita, Z.Horita, T.G.Langdon, Mater Sci Eng A, 2004; 371:241

[Furukawa 1998] M.Furukawa, Y. Iwahashi, Z.Horita, M.Nemoto, T.G.Langdon, Mater Sci Eng A, 1998; 257:328

[Gottstein 2004] G. Gottstein, Physical Foundations of Materials Science, Berlin, Germany: Springer, 2004.

[Gubicza 2004] J.Gubicza, N.Q.Chinh, Z.Horita, T.G.Langdon, Mater Sci Eng A, 2004; 387:55

[Guillot 1972] J.Guillot, J.Grilhe, Acta Metall, 1972; 20:291

[Hähner 1996] P.Hähner, Mater Sci Eng A, 1996; 207:216

[Hähner 1997] P.Hähner, Acta Mater, 1997; 45:3695

[Herring 1950] C.Herring, J.App.Phys, 1950; 21:437

[Hirth 1982] JP.Hirth, J.Lothe, Theory of dislocations (2nd Ed)

[Horita 1996] Z.Horita, D.J.Smith, M.Furukawa, M.Nemoto, R.Z.Valiev, T.G.Langdon, J Mater Res, 1996; 11:1880

[Horvath 2007] Gy.Horvath, N.Q.Chinh, J.Gubicza, J.Lendvai, Mater Sci Eng A, 2007; 445:186

[Hu 2008] W.Hu, R.Berghammer, G.Gottstein, Wiley-VCH, 2008; p842

[Iwahashi 1996] Y.Iwahashi, J.Wang, Z.Horita, M.Nemoto, T.G.Langdon, Scr. Mater, 1996; 35:143

[Iwahashi 1997] Y.Iwahashi, Z.Horita, M.Nemoto, T.G.Langdon, Acta Mater, 1997; 45:4733

[Iwahashi 1998] Y.Iwahashi, Z.Horita, M.Nemoto, T.G.Langdon, Metal and Mater Trans A, 1998; 29:2503

[Kalk 1995] A.Kalk, A.Nortmann, Ch.Schwink, Philos Mag A, 1995; 72:1239

[Koch 1992] C.C.Koch, Y.S.Cho, Nanostruct. Mater, 1992; 1:207

[Kocks 1981] U.F.Kocks, Chalmers Anniversary Volume, Pergamon Press, Oxford, 1981

[Kocks 1985] U.F.Kocks, R.E.Cook, R.A.Mulford, Acta Metall, 1985; 33:623

[Komura 1999] S.Komura, Z.Horita, M.Nemoto, T.G.Langdon, J.Mater Res, 1999; 14:4044

[Kubin 1990] L.P.Kubin, Y.Estrin, Acta Metall, 1990; 38: 697

[Kubin 1992] L.P.Kubin, Y.Estrin, C.Perrier, Acta Metall, 1992; 40:1037

[Kuhlmann 1982] Doris Kuhlmann-Wilsdorf, J.H.Van der Merwe, Mater Sci Eng, 1982; 55:79

[Kumar 1995] S.Kumar, Scr.Metall.Mater, 1995; 33:81

[Labusch 1970] R.Labusch, A Statistical Theory of Solid Solution Hardening, 1970

[Lee 1993] S.Lee, Doctor thesis, RWTH Aachen University, 1993

[Lee 1993] S.Lee, P.B.Berbon, M.Furukawa, Z.Horita, Mater Sci Eng A, 1993; 272:63

[Lee 2002] S.Lee, A.Utsunomiya, H. Akamatsu, K. Neishi, M.Furukawa, Z.Horita, T.G.Langdon, Acta Mater, 2002; 50:553

[Li 2004] Y.J.Li, X.H.Zeng, W.Blum, Acta Mater, 2004; 52:5009

[Ling 1993] CP.Ling, P.G.McCormick, Acta Metall Mater, 1993; 41:3127

[May 2005] J.May,H.W.Höppel, M.Göken, Scr Mater, 2005; 53:189

[McCormick 1971] P.G.McCormick, Acta Metall, 1971; 19:463

[McCormick 1972] P.G.McCormick, Acta Metall, 1972; 20:351

[McCormick 1972] P.G.McCormick, Scripta Metall, 1972; 6:165

[McCormick 1978] P.G.McCormick, Scr Metall, 1978; 12:443

[Miura 1972] S.Miura, Soc.Mater.Sci, 1972; 1:128

[Molodova 2008] X.Molodova, Doctor thesis, RWTH Aachen University, 2008

[Morris 2002] D.G.Morris, M.A.Munoz-Morris, Acta Mater, 2002; 50:4047

[Mrowka-Nowotnik 2005] G.Mrowka-Nowotnik, J.Sieniawski, Journal of Materials Processing Technology, 2005; 162:367

[Mulford 1979] R.A:Mulford, U.F.Kocks, Acta Metall, 1979; 27:1125

[Mulford 1979] R.A.Mulford, Metal. Trans. A, 1979; 10:1527

[Murr 1975] L.E.Murr, Interfacial Phenomena in Metals and alloys, 1975; 25:387

[Musalimov 1989] R.SH.Musalimov, R.Z.Valiev, N.K.Tsenev, Phys Stat Sol. (a), 1989; 115:451

[Nortmann 1997] A.Nortmann, Ch.Schwink, Acta Mater, 1997; 45:2043

[Penning 1972] P.Penning, Acta Metall, 1972; 20:1169

[Picu 2004] R.C.Picu, D.Zhang, Acta Metar, 2004; 52:161

[Picu 2004] R.C.Picu, Acta Metar, 2004; 52:3447

[Picu 2005] R.C.Picu, G.Vincze. F.Ozturk, J.J.Gracio, F.Barlat, A.M.Maniatty, Mater Sci Eng A, 2005; 390:334

[Räuchle 1973] W.Räuchle, O.Vöhringer, E.Macherauch, Mater.Sci.Eng, 1973; 12:147

[Rigney 1988] D.A.Rigney, Ann.Rev.Mater.Sci, 1988; 18:141

[Rizzi 2004] E.Rizzi, P.Hähner, International Journal of Plasticity, 2004; 20:121

[Roters 2000] Roters.F, Rabbe.D, Gottstein.G, Acta Mater, 2000; 48:4181

[Sanders 1986] J. R. E. Sanders, S. F. Baumann and H. C. Stumpf, "Non-Heat-Treatable Aluminum Alloys," in *Aluminum Alloys-Physical and Mechanical Properties*, West Midlands, EMAS, 1986, pp. 1441-1484.

[Schwaz 1985] R.B.Schwaz, L.L.Funk, Acta Metall, 1985; 33:295

[Schwink 1997] Ch.Schwink, A.Nortmann, Mater.Sci.Eng.A, 1997; 234:1

[Seeger 1955] A.Seeger, Phi Mag, 1955; 46:1194

[Shercliff 1990] H.R.Shercliff, M.F.Ashby, Acta Metall. Mater, 1990; 38:1789

[Sjölander 2010] E.Sjölander, S.Seifeddine, Journal of Materials Processing Technology, 2010; 10:1249

[Sleeswyk 1958] A.W.Sleeswyk, Acta Metall, 1958; 6:598

[Soare 2005] M.A.Soare, R.C.Picu, Int J Multiscale Comp Eng, 2005; 3:415

[Soare 2008] M.A.Soare, W.A.Curtin, Acta Mater, 2008; 56:4091

[Soare 2008] M.A.Soare, W.A.Curtin, Acta Mater, 2008; 56:4046

[Springer 1991] F.Springer, Ch.Schwink, Scr Metall, 1991;25:2739

[Sun 2000] P.L.Sun, P.W.Kao, C.P.Chang, Mater Sci Eng A, 2000; 283:82

[Terhune 2002] S.D.Terhune, D.L.Swisher, K.Oh-ishi, Z.Horita. T.G.Langdon, T.R.McNelley, Metal and Mater Trans A, 2002; 33:2173

[TOTAL Materia] Total Materia database.

[Totten 2003] G. E. Totten and D. S. MacKenzie, Handbook of Aluminum, New York, United States: Marcel Dekker, Inc., 2003.

[Ungar 1984] T.Ungar, H.Mughrabi, D.Rönnpagel, M.Wilkens, Acta Metal, 1984; 32:333

[Valiev 2006] R.Z.Valiev, T.G.Langdon, Progress in Materials Science, 2006; 51:881

[van den Beukel 1982] A.van den Beukel, U.F. Kocks, Acta Metall, 1982; 30:1027

[van den Beukel 1975] A.van den Beukel, Phys. Status. Sol. A, 1975; 30:197

[van den Beukel 1980] A.van den Beukel, Acta Metall, 1980; 28:965

[Vandenbrink 1975] S.H.Vandenbrink, A.van den Beukel, P.G.McCormick. Phys. Status. Sol. A, 1975; 30:469

[Varschavsky 1998] A.Varschavsky, E.Donoso, Mater.Sci.Eng.A, 1998; 251:208

[Wang 1993] J.Wang, Z.Horita, M.Furukawa, M.Nemoto, N.K.Tsenev, R.Z.Valiev, Y.Ma, T.G.langdon, J Mater Res, 1993; 8:2810

[Wang 1996] J.Wang, Y.Iwahashi, Z.Horita, M.Furukawa, M.Nemoto, R.Z.Valiev, T.G.Langdon, Acta Mater, 1996; 44:2973

[Wang 2006] K.Wang, N.R.Tao, G.Liu, J.Lu, K.Lu, Acta Mater, 2006; 54:5281

[Weertman 1968] J .Weertman, Trans.Am.Soc.Metals, 1968; 61:681

[Wei 2004] Wei.Q, Cheng.S, Ramesh.K.T, Ma.E, Mater Sci Eng A, 2004; 381:71

[Wei 2007] Wei.Q, Jour Mater Sci, 2007; 45:1709

[Wei 2011] Wei.Q, Pan.Z.L, Wu,X.L, Acta Mater, 2011; 59:2423

[Wycliffe 1980] P.Wycliffe, U.F.Kocks, J.D.Embury, Scripta Metal, 1980; 14:1349

[Yavari 1981] P.Yavari, FA.Mohamed, LG.Langdon, Acta Metall, 1981; 29:1495

[Zhang 2008] F.Zhang,W.A.Curtin, Model.Simul,. Mater.Sci.2008; 16:1

[Zhang 2009] S.Zhang, Master thesis, RWTH Aachen University, 2009

[Zhang 2010] S.Zhang, W.Hu, R.Berghammer, G.Gottstein, Acta Mater, 2010; 58:6695

[Zhao 2008] Y.H.Zhao, J.F.Binget, Y.T.Zhu, X.Z.Liao, R.Z.Valiev, T.G.Langdon, Appl Phys Lett, 2008, 92:081903

[Zhilyaev 2008] A.P.Zhilyaev, T.G:Langdon, Prog.Mater Sci, 2008; 53:893